UPSCALING THE GEOMECHANICAL PROPERTIES OF SHALE FORMATIONS FROM DRILL CUTTINGS

A Dissertation

Presented to

the Faculty of the Department of Petroleum Engineering

University of Houston

In Partial Fulfillment

of the Requirement for the Degree

Doctor of Philosophy

in Petroleum Engineering

by

Wenfeng Li

May 2019

UPSCALING THE GEOMECHANICAL PROPERTIES OF SHALE FORMATIONS FROM DRILL CUTTINGS

Wenfeng Li

Approved:

Chair of the Committee
Ahmad Sakhaee-Pour, Assistant Professor,
Department of Petroleum Engineering

Committee Members:

Mohamed Soliman, Professor,
Department of Petroleum Engineering

Konstantinos Kostarelos, Associate Professor,
Department of Petroleum Engineering

George K. Wong, Associate Professor,
Department of Petroleum Engineering

Maysam Pournik, Assistant Professor,
Department of Mechanical Engineering,
University of Texas Rio Grande Valley

Suresh K. Khator, Associate Dean,
Cullen College of Engineering

Mohamed Soliman, Professor and Chair,
Department of Petroleum Engineering

Acknowledgements

I would like to express my sincere appreciation to my advisor, Dr. Ahmad Sakhaee-Pour, for his guidance and support throughout my graduate study. His constant suggestions for high-quality research have caused me to strive for the very best. This work would have not been possible without his continuous instruction and support.

Special thanks are due to the members of my Ph.D. committee, Prof. Mohamed Soliman, Prof. Konstantinos Kostarelos, Prof. George Wong, and Prof. Maysam Pournik, for their valuable comments on my research. Their comments have helped me to greatly improve my work. I have also benefited a great deal from their professional experience.

I also thank the team members in our research group, Mr. Huy Tran and Ms. Chen Yu, for their assistance during my stay at UH. This dissertation is dedicated to my family, for their continuous love, understanding, and support.

UPSCALING THE GEOMECHANICAL PROPERTIES OF SHALE FORMATIONS FROM DRILL CUTTINGS

An Abstract

of a

Dissertation

Presented to

the Faculty of the Department of Petroleum Engineering

University of Houston

In Partial Fulfillment

of the Requirement for the Degree

Doctor of Philosophy

in Petroleum Engineering

by

Wenfeng Li

May 2019

Abstract

The geomechanical properties of reservoirs—important for formation stimulation—are often determined from triaxial tests on core plugs. Recovery of these samples is difficult because shales are mechanically unstable and usually disintegrate. To predict the elastic properties of shales at the core scale, we propose two models based on different measurements of drill cuttings.

First, a conceptual model is proposed to predict the elastic properties of shales at the core scale from nanoindentations. Nanoindentation measures the local (small-scale) mechanical properties of a shale, whose correlation to the core- and block-scale properties is unclear because of shale's heterogeneous structure. The proposed model accounts for the effective stiffness of small-scale constitutive minerals at a large scale. It is applied to samples recovered from the Woodford shale and the results are promising.

Second, a hierarchical model is developed to predict the elastic properties of shales at the core scale by accounting for the mineralogy, porosity, pore structure, and grain-size distribution. The hierarchical model entails two-scale simulations. At the small (grain) scale, a physically representative element is developed to capture the elastic deformation of a solid grain with a known porosity and pore structure. At the large (core) scale, the model is built based on the volume fractions of the minerals and representative elements characterized at the small scale. The minerals are randomly distributed in the core-scale model. The finite element method is used to compute the elastic moduli. The proposed models are applied to the New Albany, Rocky Mountain Siliceous, Lower Bakken, and Barnett shales. The predicted elastic moduli capture the measured values parallel to the bedding plane.

The hierarchical model allows us to determine the anisotropic elastic properties of shale formations at the core scale with additional consideration of the microfabric structures of the matrix. The model is implemented for Lower Bakken, Barnett, and Haynesville shales. Independent lab measurements corroborate the predicted anisotropic elastic moduli at the core scale. The two models have major applications in characterizing shale formations at the core scale from drill cuttings and can potentially be used for real-time analyses in a mobile field laboratory.

Table of Contents

List of Figures

List of Tables

Chapter 1. Introduction

1.1. Problem statement

Geomechanics is important in petroleum engineering, as it is required in many aspects of hydrocarbon exploitation. In drilling engineering, it helps us to identify the formation fracture resistance, which is required for preventing the loss of the circulating fluid (Bourgoyne et al., 1991). Investigation of the wellbore stability issue requires a comprehensive knowledge of the formation geomechanics (Zoback 2008). In reservoir engineering, the transport properties show dependence on the effective stresses, whose values can be determined based on the corresponding geomechanical principles (Sayers and Schutjens 2007). Another important application of geomechanics in petroleum engineering is hydraulic fracturing, which is crucial for economic production from tight formations, such as shales (Soliman 1990; Dahi-Taleghani and Olson 2011).

Researchers have made significant efforts to characterize the geomechanical properties of the shales (Sone 2012; Chen et al., 2017; Vachaparampil and Ghassemi 2017), the hydrocarbon production from which has launched a new era in the petroleum industry. However, the geomechanical characterization of shales remains difficult due to several issues. First, a shale formation is strongly heterogeneous because its matrix is composed of the carbonates, silica, clays, and organic matter in different volume fractions (Loucks et al., 2009). Different compositions of the forming minerals result in different geomechanical properties due to the different mechanical properties (Mavko et al., 2009). Second, it is difficult to recover large shale samples for core-scale tests because they are mechanically unstable and usually break down into pieces.

Researchers have used small-scale measurements to predict the large-scale properties. For instance, nanoindentations have been used to predict the core-scale elastic properties of shales (Ulm and Abousleiman 2006; Bobko and Ulm 2008; Bennett et al., 2015). Researchers have also proposed analytical models to predict the geomechanical properties of a shale formation based on the forming minerals (Levin and Markov 2005; Ortega et al., 2007; Chen et al., 2016). The analytical models are usually complex and difficult to implement, and lead to uncertainties of close to 40 to 50% (Ortega et al., 2007).

1.2. Objectives

The main objective of this study is to predict the geomechanical properties of a shale formation at the core scale based on the small-scale measurements conducted on drill cuttings. Two distinct methods are proposed, as follows:

a) A conceptual model that accounts for the effective stiffness of the forming minerals at the nanoscale based on nanoindentations.

b) A hierarchical model that accounts for the mineral composition, porosity, pore structure, grain size distribution, and microfabric structures.

The first method is used to predict the core-scale elastic properties of shale formations from the nanoindentations. The second method is adopted to predict the isotropic elastic properties of shale and carbonate formations. It is also extended to predict the anisotropic elastic properties of shales by accounting for the pore and fabric structures in different directions (parallel and perpendicular to the bedding).

1.3. Hypotheses

I hypothesize that the elastic properties of a shale formation at the core scale can be predicted if one accounts for the effective stiffness of the constitutive entities at a large scale (**hypothesis I**). This is relevant to the first method. A combination of the entities form a loading frame to sustain the load applied in nanoindentation. The hypothesis implies that the effective properties of the loading frame are mainly determined by the softer entities, even if they are not perturbed directly. The combination of the loading frames determines the elastic behavior of a bulk shale. Accordingly, a conceptual model (Fig. 1.1) is proposed to predict the core-scale elastic modulus of a shale based on nanoindentations. In Fig 1.1a, the softer entity (shown in grey), whose length change is denoted by Δl, deforms more significantly under loading and controls the effective stiffness. In Fig 1.1b, the red dotted lines show the loading frames in the conceptual model. Fig. 1.1c shows the macroscale representation of the shale whose relevant measurements are used to test the model (courtesy of Li and Sakhaee-Pour 2016).

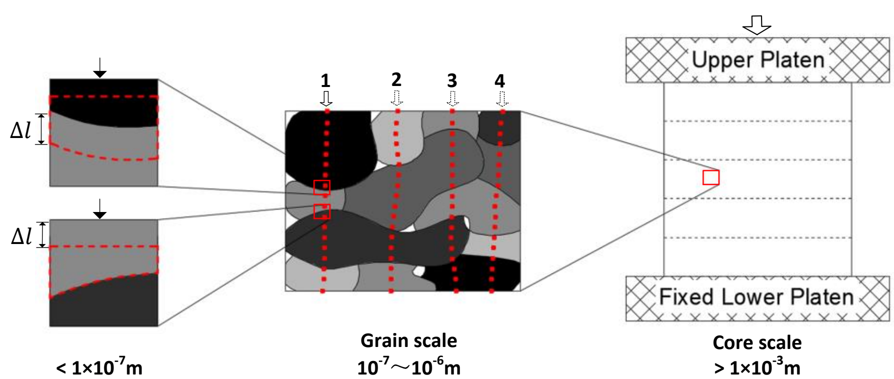

a. b. c.

Figure 1.1 – The conceptual model (Fig. 1.1) for predicting the core-scale elastic modulus of a shale based on nanoindentations (courtesy of Li and Sakhaee-Pour 2016).

The predicted elastic moduli of a shale formation, based on the conceptual model (Fig. 1.1), are compared against independent measurements to test the first hypothesis. The hypothesis is falsifiable because the predicted values can deviate from the lab measurements.

I hypothesize that the elastic properties of shales at the core scale can be captured if I account for the mineralogy, porosity, pore structure, and grain-size distribution (**hypothesis II**). This is relevant to the second method. A workflow (Fig. 1.2) based on a hierarchical model is developed to test this hypothesis. The workflow includes a grain-scale model, which accounts for the mineralogy, grain size, and pore structure, and a core-scale model that utilizes the volume fraction of the minerals and the effective properties at the grain scale.

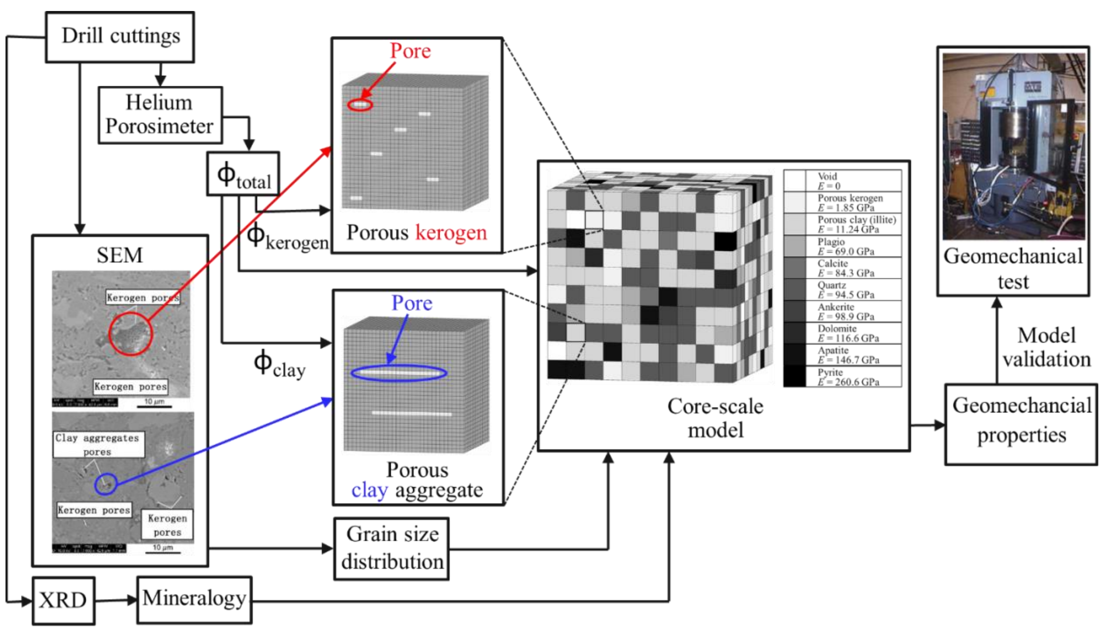

Figure 1.2 – Workflow for predicting the elastic properties of a shale formation at the large scale from drill cuttings. The workflow is implemented based on the model that includes the grain and core scales (Sakhaee-Pour and Li 2018).

Independent lab measurements are used to test the predicted elastic properties in order to test the second hypothesis. The second hypothesis is also falsifiable because the predicted value can differ from the measured value.

Throughout this dissertation, small scale refers to the grain scale, which is typically on the order of nano- to a few micro-meters for shales (Loucks et al., 2009). The large scale is relevant to the core scale on the order of a few centimeters (Sone 2012). These definitions will be frequently used in the following chapters.

1.4. Summary of chapters

In Chapter 2, the fundamental concepts of nanoindentation are presented, as nanoindentation enables us to obtain the elastic modulus and hardness of a homogeneous medium. The application of nanoindentation to shale samples is then discussed, with a focus on the limitations of the current interpretation of the measurements. In addition, the literature review also covers the existing methods of modeling the elastic properties of shales at the core scale from the forming minerals. The issues associated with the existing methods are illustrated. The elastic potential energy of a solid medium is then reviewed because the concepts are necessary for the hierarchical model (Fig. 1.2). Finally, for completeness, the conventional geomechanical characterization of rocks at the core scale is briefly discussed.

In Chapter 3, a conceptual model is proposed to predict the elastic properties of a shale at the core scale from nanoindentation measurements. The proposed model accounts for the effective stiffness of a combined volume in the nanoindentation, and relates that effective stiffness to the pertinent properties of the shale at the core scale. The predicted elastic properties at the core scale are tested against the independent lab measurements for model validation. The proposed model has major implications for understanding the large scale properties of the heterogeneous media from nanoindentation measurements.

In Chapter 4, a hierarchical model is presented to predict the elastic properties of shales at the core scale from the mineral composition, porosity, pore structure, and grain-size distribution. The hierarchical model starts with a grain-scale model to capture the elastic deformation of a grain with a known mineralogy. The grain-scale model enables us to develop a representative element which is used to build the core-scale model. The finite element method is adopted to solve the hierarchical model and derive the elastic moduli of shales at the core scale. The computed results are compared with independent lab measurements. The proposed model is important because it allows us to characterize the geomechanical properties of shales at the core scale from small-scale measurements that can be conducted on drill cuttings. This is crucial because it is expensive and difficult to recover a core-scale shale sample for the geomechanical characterization.

In Chapter 5, the hierarchical model is applied on a carbonate (Arab-D) formation to predict its elastic properties at the core scale from the mineralogy and the void system. Compared to shales, carbonates have a more complex void system, which significantly influences the geomechanical properties at the core scale. The complex void system is accounted for in the hierarchical model to quantitatively analyze its effect on the core-scale elastic properties of carbonates. To validate the model, the simulation results are compared with independent lab measurements of the same formation.

In Chapter 6, the hierarchical model is revised to predict the anisotropic elastic properties of shales at the core scale from the mineral composition, porosity, pore structure, grain-size distribution, and microfabric structures. All these factors contribute to the anisotropic elastic behavior of shales at the core scale. A sensitivity analysis is conducted to study the dependency of the predicted anisotropic elastic moduli on the governing parameters. This is important because it allows us to systematically and quantitatively determine the importance of each parameter, which has not been achieved previously. The anisotropic elastic properties of shales have many field applications, such as in-situ stress interpretation and wellbore stability analysis, where failure to account for the anisotropic elasticity of shales may cause significant errors.

The assumptions and limitations of the proposed models are discussed in Chapter 7 for completeness. A range of the applied load (displacement) in nanoindentation is suggested for applying the proposed conceptual model (Fig. 1.1) to shales. In contrast, the hierarchical model predicts the core-scale elastic properties of shales in quasi-static conditions, whose dependency on the temperature, fractures, and rock-fluid interactions are beyond the scope of the present study.

The conclusions are presented in Chapter 8. The proposed models may also be utilized to predict other geomechanical properties of shales, such as creep and strength properties. Recommendations for future work on these aspects are also given.

Chapter 2. Literature Review

Hydrocarbon energy is important for human development. According to a BP statistical review of world energy (2017), oil and natural gas account for 33.28% and 24.13% of the global total energy consumption, respectively, in 2016 (Fig. 2.1). Most predictions indicate that the demand for oil and gas will increase substantially, which demonstrates the importance of hydrocarbon exploitation (Jarvie 2012; BP 2017).

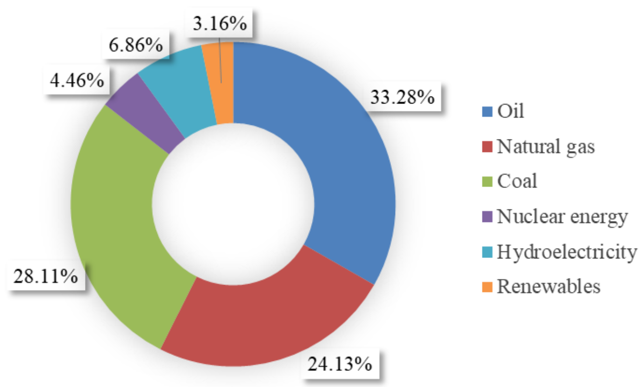

Figure 2.1 – Energy consumption share of the major sources in 2016 (data from BP 2017).

Hydrocarbons are produced from sandstone, carbonate, and shale formations. Carbonate formations constitute close to half of the world's oil reserves (US EIA 2017), and based on some estimates up to 60% (Burchette 2012). In the Middle East, carbonates alone contain close to half of the world's hydrocarbon resources (Edgell 1997). Source shales also contain significant amounts of organic matter from which people can extract hydrocarbons. Hydrocarbon production from shale formations has changed the global energy supply, and will play an increasingly important role in the oil and gas industry. The US EIA (2017) estimates that the U.S. has close to 200 trillion cubic feet of proved shale gas and it may have nearly 623 trillion cubic feet of additional unproved shale gas, which is technically recoverable.

There are many technical challenges in producing hydrocarbons from shale formations. For instance, seismic data processing lacks accuracy (Sayers 2005); the effective transport properties of shales are not fully understood (Sakhaee-Pour and Bryant 2012); and economic feasibility studies and hydraulic fracturing design face challenges (Soliman et al., 2004; Warpinski et al., 2013; Wong et al., 2017). Geomechanics plays an important role in addressing these issues.

Geomechanics is important in seismic interpretation for shale formations. Seismic data allows one to identify the potential geological structures that influence the oil and gas exploitation from shales. These data, such as the wave velocity, seismic impedance, and seismic amplitude, are strongly impacted by the shale characteristics. Seismic uncertainties can be reduced by incorporating the geomechanical characteristics of shales in the interpretation (Wang 2002; Barkved and Kristiansen 2005).

Geomechanics is crucial for successful drilling and completion operations. First, shale formations may be fractured if the circulating fluid in the wellbore provides a pressure that the formation cannot withstand. The occurrence of this issue causes a significant loss of the circulating fluid. Geomechanics can help to identify the formation fracture resistance, thus avoiding this issue (Bourgoyne et al., 1991). Second, drilling releases the radial confinement of the penetrated shales, which may cause wellbore instability. The investigation of wellbore stability requires a comprehensive knowledge of the rock strength and in-situ stresses, as well as of wellbore geometry, inclination, and trajectory (Zoback 2010).

Geomechanics is also an essential part of integrated reservoir characterization. An accurate determination of in-situ stresses enables us to better estimate the reservoir deliverability because the permeability is stress dependent. Further, reservoir depletion changes the formation pore pressure, which causes an increase of the effective stresses. Researchers have reported that many issues, such as surface subsidence, casing deformation, fault activation, and bedding-parallel slip, are related to effective stress changes (Sayers and Schutjens 2007).

Another important application of geomechanics is hydraulic fracturing. Hydraulic fracturing is a stimulation technique in which large amounts of fluid and sands are usually injected into the formation (Montgomery and Smith 2010; Dahi-Taleghani and Olson 2011; Sesetty and Ghassemi 2015). The shale reservoir is usually fractured in order to increase its permeability. The formation fracture gradient often varies significantly along a well. Shale formations respond differently to fluid injection. Maxwell (2011) reported that fluid injection created macroscopic fracture planes at some injection points, while it induced complex fracture networks at other locations. Geomechanics can help us to gain a deeper understanding of the outcome of hydraulic fracturing operations.

Realizing the importance of geomechanics, researchers have characterized the pertinent properties of shale samples from triaxial tests on large scale samples such as core plugs (~ 1 in). For several reasons, however, it is not always possible to conduct such measurements. First, it is difficult to recover a core plug because the shale formation is mechanically unstable and usually breaks down into pieces during extraction (Donath 1961; Gomes and He 2012; Cheng et al., 2015). Second, extensive coring work with a coring interval of 3 to 5 ft (Xu and Sonnenberg 2016) is required to cover the formation of interest, which dramatically increases the associated cost.

Due to these difficulties in characterizing the geomechanical properties of shale formations from large-scale samples, researchers have used small-scale (sub core-scale) samples to predict the relevant properties at the core scale. For instance, researchers have conducted nanoindentations (Bobko and Ulm 2008) and used scanning electron microscopes (Bennett et al., 2015) on small samples (a few millimeters in size) and have analyzed the relation between the measured values and those at the core-scale (Ulm and Abousleiman, 2006). A more sophisticated technique, which couples nanoindentation and energy-dispersive X-ray spectroscopy (EDX), has also been used to extract the in-situ properties of the forming minerals and estimate the mechanical properties of a shale formation (Abedi et al., 2015 and 2016; Monfared and Ulm 2016; Veytskin et al., 2017). Such small-scale measurements account for the shale heterogeneity and can be conducted on drill cuttings, instead of core plugs. Thus, they serve as promising tools for the geomechanical characterization of a shale formation, although it is not yet clear whether there is a close relation between the measurements made so far and the relevant properties at the large scale.

Researchers have proposed analytical models to predict the geomechanical properties of the shale formation at the core scale based on the forming minerals and microstructures (Levin and Markov 2005; Ortega et al., 2007; Chen et al., 2016). Based on the mineral composition and grain-size distribution, Levin and Markov (2005) and Levin et al., (2012) used an effective-medium theory to predict the elastic properties of shales at the core scale. The homogenization theory has also been adopted to predict the large-scale properties by accounting for the mineral content and porosity (Ortega et al., 2007; Chen et al., 2016; Monfared and Ulm 2016). The error associated with the analytical method was on the order of 40 to 50% for different shales (Ortega et al., 2007; Monfared and Ulm 2016). The analytical models determine the effects of forming minerals, but they are complex and difficult to implement. More importantly, they are limited to simplified geometries for the void and the grain.

The present study presents two methods, elaborated in the preceding chapter, to predict the core-scale elastic properties of a shale from small-scale measurements. The basic concepts and principles of the two methods are introduced in this chapter. For completeness, the conventional method for geomechanical characterization of shales at the core scale is also discussed.

2.1. Basic concepts of nanoindentation

Hertz's contact theory is briefly mentioned because it forms the foundation for the interpretation of nanoindentation measurements. In 1886 to 1889, Hertz pioneered analytical solutions for the stress and displacement distribution in an elastic body subjected to a force on a free surface. These analytical solutions have been illustrated in many elasticity books, such as that of Landau and Lifschitz (1999). Thus, they are not elaborated here. However, it is important to mention two major assumptions of Hertz's work (Johnson et al., 1971): 1) the force is applied on an infinitely large half-space of an elastic medium; and 2) adhesive force is ignored between the two media in contact. These two assumptions have been modified accordingly to discover more applications (Popov

2010). Nanoindentation is one typical application of Hertzian contact theory. The remaining content in this section covers the fundamental concepts of nanoindentation.

2.1.1. Nanoindentation modulus

Nanoindentation is usually applied to determine the mechanical properties of a homogeneous medium. A hard tip with known geometry and mechanical properties is placed on the surface of the medium. The force is then increased continuously and the penetration depth is recorded. The force-displacement measurements (Fig. 2.2) allow us to calculate the indentation modulus as follows (Fischer-Cripps 2004):

$$M = \frac{\sqrt{\pi}}{2\alpha}\frac{S}{\sqrt{A_c}}, \tag{2.1}$$

where M is the indentation modulus, α is a correction factor related to the geometry of the indenter (= 1.034 for a Berkovich tip), S is the slope of the force-displacement curve at the beginning of the unloading (Figure 2.2), and A_c is the projected contact area.

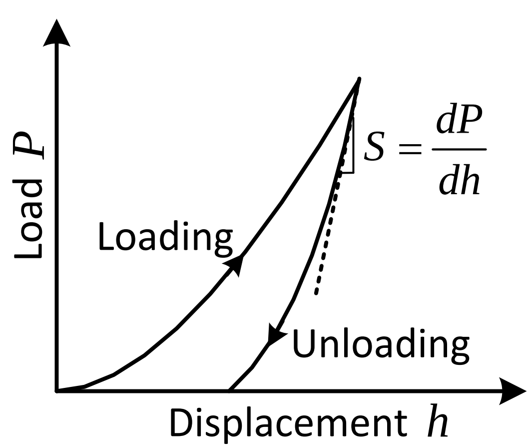

Figure 2.2 – A representative load-displacement curve of a nanoindentation test. The slope S at the beginning of the unloading is used to determine the indentation modulus M according to Eq. 2.1 (courtesy of Li and Sakhaee-Pour 2016).

Oliver and Pharr (1992) suggested the following equation to calculate the projected contact area (A_c) for a Berkovich indenter:

$$A_c = 24.5\, h_c^2 + C_1 h_c^1 + C_2 h_c^{1/2} + C_3 h_c^{1/4} + \cdots + C_8 h_c^{1/128}, \tag{2.2}$$

where h_c is the depth of the elastic contact, and C_1 through C_8 are constants. Only the lead term is necessary for a sharp Berkovich tip; other terms are needed when the tip is blunt.

The depth of the elastic contact (h_c) can be obtained from the following equation (Oliver and Pharr 1992):

$$h_c = h_{max} - \frac{2}{\pi}(\pi - 2)\frac{P_{max}}{S}, \tag{2.3}$$

where h_{max} is the maximum indentation depth that is recorded during the test.

The Young's modulus is determined based on the indentation modulus (M) as follows (Fischer-Cripps 2004):

$$\frac{1}{M} = \frac{1 - \nu^2}{E} + \frac{1 - \nu_i^2}{E_i}, \tag{2.4}$$

where E is the Young's modulus of the indented medium, ν is the Poisson's ratio of the indented material, E_i is the Young's modulus of the indenter, and ν_i is the Poisson's ratio of the indenter.

2.1.2. Hardness

Hardness can also be obtained from a nanoindentation as follows (Fischer-Cripps 2004):

$$H = \frac{P_{max}}{A_c}, \tag{2.5}$$

where H is the hardness of the indented medium, P_{max} is the applied force, and A_c is the projected contact (Eq. 2.2).

The indentation hardness is related to the strength properties of the medium. For a cohesive medium, researchers have proposed many theoretical models to study the correlation between the hardness (H) and the yield stress (Y) (Hill et al., 1947; Samuels and Mulhearn 1957; Tabor 1985; Johnson 1987; Fischer-Cripps 2004), and the general rule of thumb is that the ratio of H to Y is equal to 3 (Cheng and Cheng 2004). In contrast, the hardness–strength relation of a cohesive-frictional medium, like a rock, has not been studied in the same depth and the existing models are mainly empirical (Chollacoop et al., 2003; Constantinides et al., 2003). For instance, Ganneau et al., (2006) proposed the following relation to determine the cohesion and friction angle:

$$\frac{H}{c} = \frac{1}{tan\varphi}\sum_{k=1}^{6}(a_k \cdot tan\varphi)^k \,, \tag{2.6}$$

where c is cohesion, φ is the friction angle, and a_1 = 5.7946, a_2 = –2.9455, a_3 = 2.6309, a_4 = 4.2903, a_5 = –3.4887, a_6 = 2.7336 are tuning parameters, which depend on the tip geometry. Ganneau's model suggests that the value of H/c varies from 16 to 115 when the friction angle changes from 20° to 40°.

2.1.3. Indenter tips

It is necessary to review the popular indenter tips because the interpretation of the nanoindentation measurements depends on the geometry of the indenters. Fig. 2.3 illustrates four major nanoindentation tips: spherical, conical, Vickers, and Berkovich.

Cube core and Knoop tips are not shown here because they are less popular in applications (Fischer-Cripps 2004).

Indenters are usually classified into blunt and sharp tips based on their geometry. Although there are no widely-accepted criteria for tip classification (Fischer-Cripps 2004), a common definition is that a blunt tip provides a smooth transition from elastic to plastic contact in the indentation test, while a sharp tip induces plastic (irreversible) deformation immediately after contact (Lawn and Wilshaw 1993). Thus, a spherical indenter (Fig. 2.3a) is usually considered to be a blunt tip, whereas conical, Vickers, and Berkovich indenters (Fig.s 2.3b−d) are classified as sharp tips (Fischer-Cripps 2004).

The tips are usually made of diamond because it is brittle and hard, which eases the interpretation of the nanoindentation measurements. The typical Young's modulus and Poisson's ratio of a diamond are 1143 GPa and 0.0691, respectively (Klein and Cardinale 1993). Thus, the second term on the right-hand side of Eq. 2.4 is negligible for indentations on various media, such as metals, glasses, ceramic, concrete, and rocks (Page et al., 1992; Shi and Falk 2007; Ulm et al., 2007).

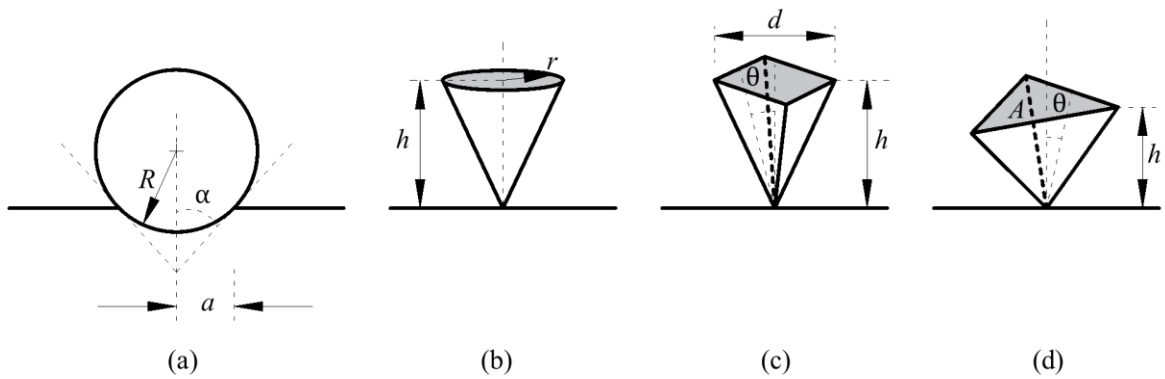

Figure 2.3 – Typical indenter tips: (a) spherical, (b) conical, (c) Vickers, (d) Berkovich (courtesy of Fischer-Cripps 2004).

The geometry of a spherical indenter is shown in Fig. 2.3a. The tip is typically made of a sphero-cone for easy mounting on the indentation equipment. In the test, only the spherical tip of the indenter is used to penetrate the medium of interest.

Another popular indenter is the conical tip (Fig. 2.3b). It is easy to calculate the contact area when this indenter is used, and thus it has been widely used to measure the mechanical responses of a number of materials, such as copper (Dugdale 1954), aluminum foam (Ramamurty and Kumaran 2004), thin films (Li and Bhushan 1998), glasses (Wright et al., 2001), and rocks (Zhu et al., 2007).

Vickers and Berkovich indenters have four-sided and three-sided pyramid tips (Figs. 2.3 c and 2.3d), respectively. They are the most popular tips in nanoindentation measurements because the tips are easy to construct and generate geometrical similarity in penetration (Fischer-Cripps 2004). Geometrical similarity is discussed below.

2.1.4. Geometrical similarity

Conical and pyramid indentations have the property of geometrical similarity, which captures the ratio of the characteristic size of the contact to the penetration depth of the indenter remains constant for an increasing load. The importance of geometrically similar indentations is that the strain of the material under test remains constant, independent of the applied load (Oliver and Pharr 1992). Thus, geometrical similarity can significantly simplify the calculation of the stress field in the material under indentation (Tabor 1996).

Geometrical similarity helps us to define an equivalent cone for a pyramid (Vickers or Berkovich) indenter. This is because the projected area of contact can be expressed as a function of the penetration depth for both conical and pyramid indenters. Owing to the geometrical similarity, a Vickers or Berkovich tip has a semi-angle of 70.3° for an equivalent conical indenter. This semi-angle of an equivalent cone provides convenience when analyzing nanoindentations taken with the pyramidal indenters.

Another merit of geometrical similarity is that it provides an easy way to calculate the projected area of contact in an indentation, which is necessary for the indentation hardness determination (Eq. 2.5). For a given indenter with geometrical similarity, the projected area of contact can be analytically determined from the recorded penetration depth (Oliver and Pharr 1992). Therefore, researchers no longer need to measure the value of contact area, which is difficult, after the completion of the nanoindentations.

2.1.5. Sources of error for nanoindentation

Sources of error for nanoindentation need to be discussed for completeness. First, the nanoindenter should be mounted on a vibration-damping table to eliminate the error associated with noise in the environment (Bec et al., 2006). Second, temperature or electronic fluctuations can cause thermal drift of the tip, which results in measurement error (Briscoe et al., 1998). The thermal drift can be quantified from the beginning or end of the holding periods of the tests. To minimize this effect, the nanoindentations are usually done in a thermally stable environment.

Surface roughness of the sample is another issue that may cause measurement errors (Bobko 2008). This is a particular problem when a sharp tip is indented on a rough surface, especially for small indentation depths (Bennett et al., 2015). Therefore, the surface roughness of the sample needs to be accounted for in order to determine meaningful indentation depths.

There are other factors that could affect the accuracy of the nanoindentation measurements, such as instrument compliance, piling-up and sinking-in of the indented specimen, and tip rounding. A comprehensive review can be found in Fischer-Cripps (2004), where suggestions are also given for minimizing the effects of those factors.

2.2. Nanoindentation measurements on shales

Equations (2.1) to (2.6) are originally derived to interpret nanoindentation results on a homogeneous and isotropic medium, whose relevant properties do not vary spatially. The application of nanoindentation to shales requires further interpretation because they are heterogeneous at various length scales and possess complex structures in the matrix.

Heterogeneity significantly hinders our understanding of nanoindentations conducted on shales. Shales are composed of organic matter, clays, carbonates, quartz, and pyrite in varying amounts. These minerals have different mechanical properties (Mavko et al., 2009) and form grains with characteristics ranging from nano- to micrometer (Bobko and Ulm 2008; Loucks and Ruppel 2007; Pommer and Milliken 2015). In other cases, the grain sizes may vary up to a few millimeters (Emmanuel 2014). The various grain sizes make the nanoindentation of shales difficult because it is quite possible for the tip to penetrate multiple minerals in each indent, and there is no analytical model for the interpretation of such measurements.

Ulm and Abousleiman (2006) pioneered the interpretation of nanoindentations on shales. They hypothesized that, for a material composed of two different phases, a single indent gives access to the mechanical properties of the indented phase if the penetration depth is much smaller than the characteristic size of the phases. They conducted a number of nanoindentations with penetration depths about 200 nanometers and distinguished three to four mechanical phases from a statistical analysis. Following the same hypothesis, other researchers have determined the mechanical properties of the forming minerals in shales from nanoindentation measurements (Bobko and Ulm 2008; Abedi et al., 2016; Monfared and Ulm 2016; Liu et al., 2016 and 2018). One problem in the work of Ulm and Abousleiman (2006) is that they do not directly identify the mineral type of the penetrated phase in a single indent. Instead, they infer the mineral type by comparing the interpreted elastic modulus with the reported values of minerals in literature. Chapter 3 will discuss predicting the core-scale properties if the indentation results are assumed to be relevant to the bulk property, as opposed to a local property.

A coupled indentation–energy–dispersive X–ray spectroscopy (EDX) analysis has been developed to directly identify the probed mineral type in a single indent (Abedi et al., 2015 and 2016). EDX analysis enables one to obtain the elemental composition of the impression, from which the probed mineral type can be determined. This method was applied to Haynesville, Barnett, Marcellus, Fayetteville, and Antrim shales. The average of the measured mechanical properties of minerals was close to the reported values in the literature, although there was significant variation in the measured elastic properties for a specific mineral.

The method of Ulm and Abousleiman (2006) needs further discussion. First, their method was only for small-scale (sub-micrometer) measurements because their objective was to determine the mechanical properties of the forming phases of shales from nanoindentations. It is unclear how nanoindentation can be used to determine the core-scale properties of shales for engineering applications. Second, their hypothesis may overlook the effect of the softer entities on the nanoindentation measurements. It is possible that a single nanoindentation determines the effective properties of a combined volume, instead of only the probed grain.

Other researchers have applied a larger penetration depth, on the order of micrometers, to measure the mechanical properties of shales from nanoindentation (Bennett et al., 2015; Liu et al., 2016 and 2018). For a larger penetration depth (3–5 micrometers), the indentation measurements are relatively consistent and reproducible because the grain-scale heterogeneity may be suppressed at this measurement scale. However, it is not clear whether there is a close correlation between the nanoindentation results at this penetration depth and the relevant properties at the large scale.

It is unclear whether nanoindentation can be used to determine the anisotropic properties of shales at the core scale. The elastic anisotropy of shales can be attributed to the intrinsic anisotropy of clays (Sayers 2005), the microfabric structures of clays and organic matter (Hornby et al., 1994; Sone and Zoback 2013a), and the presence of the bedding planes. The nano- to microscale indentations may sense the intrinsic anisotropic elastic properties of clays (Bobko and Ulm 2008), but may overlook the other two factors due to the non-comparable characteristic sizes.

Despite these issues, nanoindentation is a promising tool for the geomechanical characterization of shale formations because it accounts for the heterogeneity of the shale and can be conducted on drill cuttings, instead of on core plugs. However, a model must be developed to correlate the nanoindentation measurements and the relevant properties at a large scale.

2.3. Theoretical modeling of elastic properties of shales at the core scale based on the forming minerals

The geomechanical properties of shales at the core scale depend on a number of factors. First, the mineral composition has a significant effect on the geomechanical behavior of shales (Josh et al., 2012). Researchers have reported the inverse correlations between the core-scale elastic properties of shales and the volume fraction of kerogen and clays, which are the weak minerals in the bulk volume (Sone and Zoback 2013a). Second, the microfabric structures of the forming minerals also influence the geomechanical properties of shales, when the anisotropic sheet-like clay particles are generally aligned parallel to the bedding (Sayers and den Boer 2016). It has also been documented that kerogen structures would affect the geomechanical properties of shales (Vernik and Liu 1997). Third, the geomechanical properties of shales decrease at an elevated temperature (Rybacki et al., 2015). Fourth, the orientation of the bedding planes has a profound effect on the measured geomechanical properties of shale cores (Sone and Zoback 2013a; Rybacki et al., 2015). Other factors, such as the porosity, water saturation, pore pressure, and strain rate more or less alter the geomechanical properties of shales at the core scale (Josh et al., 2012; Rybacki et al., 2015; Kamali-Asl et al., 2018).

Researchers have applied differential effective medium (DEM) theory to predict the geomechanical properties of shales at the core scale from the forming minerals. Hornby et al., (1994) formulated a DEM method to predict the anisotropic elastic properties of shales from the porosity, pore structure, clay platelet orientation, and silt grains of other minerals. The pores and silt geometries were simplified to derive an analytical solution. The predicted results agreed with the independent velocity measurements. Modifications of this method have been reported in the literature (Mukerji et al., 1995; Levin and Markov 2005; Bachrach 2011). Mavko et al., (2009) conducted a comprehensive review of this method.

Homogenization theory has also been adopted to predict the core-scale properties of shales by accounting for the mineral content and porosity. Ortega et al., (2007) elaborated a multiscale homogenization scheme for the shales without organic matter under the assumption that the pores resided in clays. The predicted elastic moduli were consistent with the reported values in the literature from velocity measurements. Researchers then applied this method to organic-rich shales by including porous kerogens (Monfared and Ulm 2016). Chen et al., (2016) incorporated the interfacial transition zone in the homogenization approach to account for the bonding between the host medium and the inclusions.

Several issues, however, are associated with the DEM and the homogenization approaches. First, it is difficult to implement the analytical formulations. Second, they are limited to simplified void and grain geometries such as spheres and spheroids. Third, some of the input parameters of the homogenization approach have to be back calculated from core-scale measurements. For instance, it is impossible to directly measure the properties of the interfacial transition zone in the laboratory, as discussed in Chen et al., (2016).

2.4. Elastic energy of a solid medium

The elastic potential energy of a solid medium is reviewed here because the concepts are necessary for predicting the geomechanical properties of a shale sample at the core scale based on the forming constituents in the hierarchical model (Fig. 1.2). The potential energy in the elastic deformation can be determined as follows (Sakhaee-Pour 2009):

$$U_{total} = \sum U_r + \sum U_\theta + \sum U_\phi, \tag{2.7}$$

where U_r, U_θ, and U_ϕ are the stretching energy, the angle bending energy, and the torsional energy, respectively. The energy terms can be related to the corresponding deformations as follows:

$$U_r = \frac{1}{2} k_r (r - r_0)^2 = \frac{1}{2} k_r (\Delta r)^2, \tag{2.8a}$$

$$U_\theta = \frac{1}{2} k_\theta (\theta - \theta_0)^2 = \frac{1}{2} k_\theta (\Delta\theta)^2, \text{ and} \tag{2.8b}$$

$$U_\phi = \frac{1}{2} k_\phi (\phi - \phi_0)^2 = \frac{1}{2} k_\phi (\Delta\phi)^2, \tag{2.8c}$$

where $k_r, k_\theta,$ and k_ϕ are the stretching stiffness, the bending stiffness, and the torsional stiffness, respectively, and $\Delta r, \Delta\theta,$ and $\Delta\phi$ denote the corresponding variations from the initial positions in equilibrium.

The theory of structural mechanics is used to determine the potential energy under elastic deformation. The total potential energy of the solid medium subjected to an external loading includes stretching or compression, bending, and twisting (Fig. 2.3). The stretching or compression energy of the solid medium with a constant cross-sectional area can be derived as follows (Li and Chou 2003):

$$U_A = \frac{1}{2}\int_0^{L_m} \frac{N^2}{E_m A_m} dl = \frac{1}{2}\frac{N^2 l}{E_m A_m} = \frac{1}{2}\frac{E_m A_m}{L_m}(\Delta L_m)^2, \tag{2.9}$$

where U_A is the stretching- or compression-potential energy, N is the axial load, E_m is the Young's modulus of the solid medium, L_m is the length of the solid medium, A_m is the constant cross-sectional area of the solid medium, and ΔL_m is the change in length of the solid medium.

The bending energy of the solid medium can also be determined as follows (Li and Chou 2003):

$$U_M = \frac{1}{2}\int_0^{L_m} \frac{M^2}{E_m I_m} dl = \frac{2E_m I_m}{L_m}\alpha^2 = \frac{1}{2}\frac{E_m I_m}{L_m}(2\alpha)^2, \tag{2.10}$$

where U_M is the bending-potential energy, M is the bending load, I_m is the moment of inertia, and α is the rotational angle of the ends.

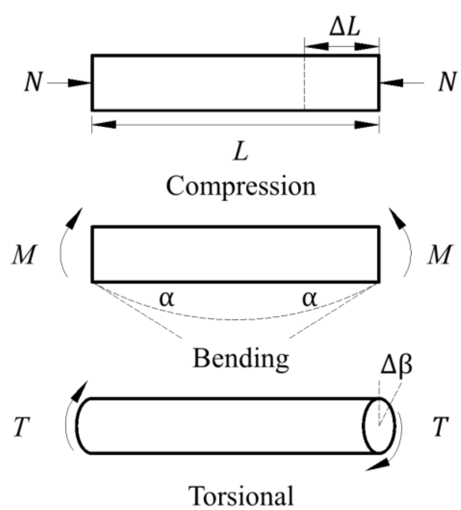

Figure 2.4 – Potential-energy terms in structural mechanics (Li and Chou 2003).

Applying a torsional load also results in a potential energy that can be computed as follows (Li and Chou 2003):

$$U_T = \frac{1}{2}\int_0^{L_m} \frac{T^2}{G_m J_m} dl = \frac{2\, T^2 L_m}{G_m J_m} = \frac{1}{2}\frac{G_m J_m}{L_m}(\Delta\beta)^2, \tag{2.11}$$

where U_T is the torsional energy, T is the pure torsion, G_m is the shear modulus, J_m is the polar moment of inertia, and $\Delta\beta$ is the relative torsion angle.

The potential-energy terms derived from the two approaches are independent. Thus, the corresponding terms can be set equal as follows:

$$k_r = \frac{E_m A_m}{L_m}, \tag{2.12a}$$

$$k_\theta = \frac{E_m I_m}{L_m}, \text{ and} \tag{2.12b}$$

$$k_\phi = \frac{G_m J_m}{L_m}. \tag{2.12c}$$

These relations dictate the effective stiffness of a solid medium (grain with a known mineralogy) dependent on its elastic properties (E_m and G_m) and the geometrical parameters ($A_m, I_m,$ and J_m). The elastic properties and the grain size available in the literature will be used subsequently to determine the pertinent terms.

The proposed hierarchical model (Fig. 1.2) includes a grain-scale model and a core-scale model. The grain-scale model requires a representative element that is mechanically equivalent to the grain in the shale matrix. Eqs. 2.7 to 2.12 will be used to develop the representative elements, which are the building elements in the core-scale model.

2.5. Measurements of elastic properties of shales at the core scale

2.5.1. Dynamic elastic properties

Shales are characterized by five independent elastic constants in the constitutive stress-strain relation. The generalized Hooke's law for a transversely isotropic (TI) medium is as follows (Jaeger et al., 2007):

$$\begin{bmatrix} \sigma_{11} \\ \sigma_{22} \\ \sigma_{33} \\ \sigma_{12} \\ \sigma_{23} \\ \sigma_{13} \end{bmatrix} = \begin{bmatrix} c_{11} & c_{12} & c_{13} & 0 & 0 & 0 \\ c_{12} & c_{11} & c_{13} & 0 & 0 & 0 \\ c_{13} & c_{13} & c_{33} & 0 & 0 & 0 \\ 0 & 0 & 0 & c_{44} & 0 & 0 \\ 0 & 0 & 0 & 0 & c_{44} & 0 \\ 0 & 0 & 0 & 0 & 0 & c_{66} \end{bmatrix} \begin{bmatrix} \varepsilon_{11} \\ \varepsilon_{22} \\ \varepsilon_{33} \\ \varepsilon_{12} \\ \varepsilon_{23} \\ \varepsilon_{13} \end{bmatrix}, \qquad (2.13)$$

where σ_{ij} is the stress tensor, ε_{ij} is the strain tensor, c_{ij} is the elastic constants, and assuming "3" denotes the direction parallel to the material symmetry axis.

Ultrasonic pulse velocities (UPV) can be related to the five independent elastic constants (c_{11}, c_{12}, c_{13}, c_{33}, c_{44} in Eq. 2.13). There are only five independent elastic constants for a TI medium because of the existence of the plane of isotropy in which the elastic constants do not depend on directions (Jeager et al., 2009). In the measurements, the UPV signals are emitted and travel through the sample in predefined directions, as shown in Fig 2.5. The recorded velocities allow us to determine the elastic constants as follows (Tran 2009):

$$c_{11} = \rho V_{P0}^2, \qquad (2.14a)$$

$$c_{33} = \rho V_{P90}^2, \qquad (2.14b)$$

$$c_{44} = \rho V_{S90}^2, \qquad (2.14c)$$

$$c_{66} = \rho V_{S0}^2, \qquad (2.14d)$$

$$c_{12} = c_{11} - 2c_{66}, \text{ and} \qquad (2.14e)$$

$$c_{13} = -c_{44} + \frac{\sqrt{\left(c_{33}cos^2\beta + c_{44}sin^2\beta - \rho V_{P\beta}^2\right)\left(c_{11}sin^2\beta + c_{44}cos^2\beta - \rho V_{P\beta}^2\right)}}{sin\beta cos\beta}. \quad (2.14f)$$

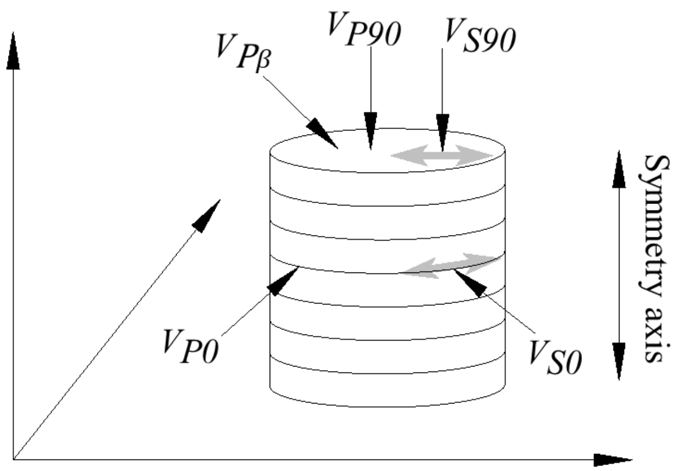

Figure 2.5 – Schematic of acoustic measurements (Tran 2009). The subscripts "*P*" and "*S*" represent the *P* wave and *S* wave, respectively. The gray arrows indicate the polarization directions of the *S* wave.

The elastic and shear moduli, as well as the Poisson's ratios, can be determined based on the constants listed in Eq. 2.13, as follows (Tran 2009):

$$E_1 = \frac{c_{11}^2 c_{33} - c_{12}^2 c_{33} - 2c_{13}^2 c_{11} + 2c_{13}^2 c_{12}}{c_{11}c_{33} - c_{13}^2}, \quad (2.15a)$$

$$E_3 = \frac{c_{11}c_{33} + c_{12}c_{33} - 2c_{13}^2}{c_{11} + c_{12}}, \quad (2.15b)$$

$$\nu_{13} = \frac{c_{12}c_{33} - c_{13}^2}{c_{11}c_{33} - c_{13}^2}, \quad (2.15c)$$

$$\nu_{31} = \frac{c_{13}}{c_{11} + c_{12}}, \text{ and} \quad (2.15d)$$

$$G = c_{44}, \quad (2.15e)$$

where E_1 is the elastic modulus perpendicular to the symmetry axis, E_3 is the elastic modulus parallel to the symmetry axis, ν_{13} is the Poisson's ratio that demonstrates the lateral strain of the sample subjected to an external force parallel to the bedding plane, ν_{31} is the Poisson's ratio that demonstrates the horizontal strain of the sample subjected to an external force perpendicular to the bedding plane, and G is the shear modulus in the plane perpendicular to the bedding.

Eqs. 2.14 and 2.15 determine the dynamic anisotropic elastic properties of a shale at the core-scale. These dynamic properties (strain on the order of 10^{-7}) are usually different from the static properties (strain on the order of 10^{-2}), which are more representative of the deformation of shales in the drilling and hydraulic fracturing operations (Mavko et al., 2009). Researchers have proposed empirical equations to correlate the dynamic elastic properties to static values, although these introduce significant uncertainties (Chang et al., 2006; Wong et al., 2008).

2.5.2. Static elastic properties

The static elastic properties are usually determined from quasi-static compressions on core plugs (Jaeger et al., 2009). To obtain the elastic properties, compressions must be conducted on plugs whose axes align differently to the bedding planes, as shown in Fig. 2.6. Fig. 2.6a shows one sample whose axis is perpendicular to the bedding. Fig. 2.6b shows the case when the axis of sample is parallel to the bedding. In Fig. 2.6c, the axis of sample is inclined to the bedding.

For axial loading on a sample whose axis is perpendicular to the bedding (Fig. 2.6a), there are two equations that relate the elastic constants to the stress and strain (Amadei 1996):

$$\frac{\varepsilon_3}{\sigma_a} = \frac{1}{E_3} \text{ and} \tag{2.16a}$$

$$\frac{\varepsilon_1}{\sigma_a} = \frac{\varepsilon_2}{\sigma_a} = \frac{\nu_{31}}{E_3}. \tag{2.16b}$$

where σ_a is the axial stress, ε_3 is the axial strain, E_3 is the Young's modulus perpendicular to the bedding, ε_1 is equal to ε_2 (lateral strain), and ν_{31} is the Poisson's ratio that characterizes the lateral strain response in the bedding plane when a force acts perpendicular to it.

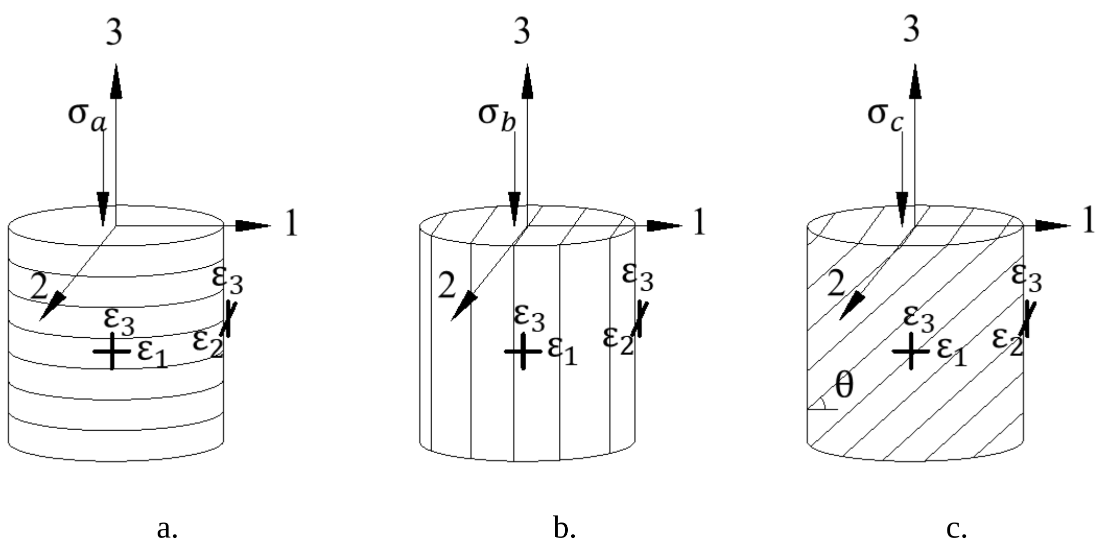

Figure 2.6 – Schematic of lab measurements for determining the elastic constants of an anisotropic medium (Amadei 1996).

For axial loading on the sample whose axis is parallel to the bedding (Fig. 2.6b), three equations relate the elastic constants to the stress and strain (Amadei 1996):

$$\frac{\varepsilon_3}{\sigma_b} = \frac{1}{E_1}, \tag{2.17a}$$

$$\frac{\varepsilon_2}{\sigma_a} = \frac{\nu_{13}}{E_1}, \text{ and} \tag{2.17b}$$

$$\frac{\varepsilon_1}{\sigma_b} = \frac{\nu_{31}}{E_3}, \tag{2.17c}$$

where σ_b is the axial stress, ε_3 is the axial strain, E_1 is the Young's modulus parallel to the bedding, σ_a is the lateral stress, ε_1 and ε_2 denote the lateral strains, and ν_{13} is the Poisson's ratio that characterizes the lateral strain response in the bedding plane when a force acts parallel to it, ν_{31} is the Poisson's ratio that describes the lateral strain response in the bedding plane when a force acts perpendicular to it, and E_3 is the Young's modulus perpendicular to the bedding plane.

For axial loading on the sample whose axis is inclined to the bedding (Fig. 2.6c), there are also three equations relating the elastic constants to the stress and strain (Amadei 1996):

$$\frac{\varepsilon_3}{\sigma_c} = \frac{sin^4\theta}{E_1} + \frac{cos^4\theta}{E_3} + \frac{sin^2 2\theta}{4}(-\frac{2\nu_{31}}{E_3} + \frac{1}{G}), \tag{2.18a}$$

$$\frac{\varepsilon_1}{\sigma_c} = \frac{sin^2 2\theta}{4}\left(\frac{1}{E_1} + \frac{1}{E_3} - \frac{1}{G}\right) - \frac{\nu_{31}}{E_3}(cos^4\theta + sin^4\theta), \text{ and} \tag{2.18b}$$

$$\frac{\varepsilon_3}{\sigma_c} = -sin^2\theta\frac{\nu_{13}}{E_1} - cos^2\theta\frac{\nu_{31}}{E_3}, \tag{2.18c}$$

where ε_3 is the axial strain, σ_c is the axial stress, θ is the angle between the bedding and the axis of the sample, E_1 and E_3 are the Young's moduli parallel to and perpendicular to the bedding, respectively, G is the shear modulus in the plane perpendicular to the bedding, ν_{31} and ν_{13} are the Poisson's ratios that characterize the lateral strain response in the bedding plane when a force acts perpendicular to and parallel to it, respectively.

To determine the five independent elastic constants of an anisotropic medium, researchers usually use three or more samples (Barla 1974; Jaeger et al., 2009), as shown in Fig. 2.6. Because there are more than five strain measurements in this method, the least-square method is required to calculate the best-fit values for the five elastic constants. Cho et al., (2012) developed a method to compute the five elastic constants from two samples that have different axes with respect to the bedding. In a case where the measurements shown in Figs 2.6a and 2.6c are conducted, the five elastic constants of a TI medium can be obtained by solving the following matrix (Cho et al., 2012):

$$\begin{bmatrix} \left(\frac{\varepsilon_1}{\sigma}\right)_a \\ \left(\frac{\varepsilon_3}{\sigma}\right)_a \\ \left(\frac{\varepsilon_2}{\sigma}\right)_a \\ \left(\frac{\varepsilon_3}{\sigma}\right)_a \\ \left(\frac{\varepsilon_1}{\sigma}\right)_c \\ \left(\frac{\varepsilon_3}{\sigma}\right)_c \\ \left(\frac{\varepsilon_2}{\sigma}\right)_c \\ \left(\frac{\varepsilon_3}{\sigma}\right)_c \end{bmatrix} = \begin{bmatrix} 0 & 0 & 0 & -1 & 0 \\ 0 & 1 & 0 & 0 & 0 \\ 0 & 0 & 0 & -1 & 0 \\ 0 & 1 & 0 & 0 & 0 \\ sin^2 2\theta/4 & sin^2 2\theta/4 & 0 & -cos^4\theta/4 - sin^4\theta/4 & sin^2 2\theta/4 \\ sin^4\theta & cos^4\theta & 0 & -2sin^2 2\theta/4 & sin^2 2\theta/4 \\ 0 & 0 & -sin^2\theta & -cos^2\theta & 0 \\ sin^4\theta & cos^4\theta & 0 & -2sin^2 2\theta/4 & sin^2 2\theta/4 \end{bmatrix} \begin{bmatrix} \frac{1}{E_1} \\ \frac{1}{E_3} \\ \frac{\nu_{13}}{E_1} \\ \frac{\nu_{31}}{E_3} \\ \frac{1}{G} \end{bmatrix}, \qquad (2.19)$$

where the subscript "*a*" and "*c*" are relevant to Figs. 2.6(a) and 2.6(c), respectively.

Researchers usually prepare the samples shown in Figs. 2.6(a) and 2.6(b) to measure the static elastic properties of shales because it is more convenient to prepare those samples in practice (Sone 2012). In this case, two elastic moduli and two Poisson's ratios can be determined based on Eqs. 2.16a, 2.16b, 2.17a, and 2.17b. The shear modulus, *G*, cannot be obtained, however, because the shear stress and shear strain parallel to the bedding are not measured.

2.6. X-ray diffraction

The X-ray diffraction (XRD) can be used to quantify the volume fractions of minerals, which are required in the hierarchical model (Fig. 1.2). The uncertainties of the mineral characterization with XRD is discussed here. XRD is a non-destructive technique for analyzing the crystal structure, chemical composition, and physical properties. XRD measures the scattered intensity of an X-ray beam hitting a sample after recording the incident and scattered angle, polarization, and wavelength (Suryanarayana and Norton 2013). Whereas mineral identification is relatively simple, the accurate analysis of clays remains challenging. This is due to the variable chemical compositions, structures, and the orientations of the clay minerals (Srodon et al., 2001). The variations result in large differences in the intensities of different samples with a similar clay mineral, which may lead to uncertainties. Researchers have proposed different methods to reduce the associated uncertainties such the whole-pattern fitting approach (Ward et al., 1999) and the diagnostic reflections based on random powders (Srodon et al., 2001). A thorough review of the existing methods were reported by Suryanarayana and Norton (2013).

2.7. Conclusions

The fundamental concepts of using nanoindentation to obtain the elastic modulus and hardness of a homogeneous medium have been reviewed. The application of nanoindentation to shales, which are heterogeneous, has also been elaborated, with a focus on the limitations of the current interpretation of the measurements. The limitations motivate us to propose an appropriate conceptual model for predicting the core-scale elastic properties of shales from nanoindentations. The conceptual model will be introduced in Chapter 3.

The literature review has covered the existing methods of modeling the elastic properties of shales at the core scale from the forming minerals and discussed the issues related to the existing methods. The elastic potential energy of a solid medium has also been reviewed because the pertinent theories allow us to develop a hierarchical model (Fig. 1.2), which will be presented in Chapters 4, 5, and 6. The purpose of the hierarchical model is to predict the core-scale geomechanical properties of shales from the mineralogy and the void system.

For completeness, two conventional methods for the geomechanical characterization of shales at the core scale have been summarized. Both methods require core-scale samples and provide the pertinent properties for validating the predictions of the proposed models in this study.

Chapter 3. A Conceptual Model to Predict the Core-Scale Elastic Modulus of a Shale Based on Nanoindentations

The content of this chapter has been published in the *Journal of Petrophysics* (Li and Sakhaee-Pour 2016). In this chapter, nanoindentation is used to determine the small-scale elastic properties of a shale. A conceptual model is proposed to predict the core-scale elastic properties of the shale from nanoindentations. Predicted elastic properties are compared with independent laboratory measurements.

3.1. A conceptual model of the core-scale deformation of a shale

To interpret the nanoindentation of a heterogeneous medium, researchers originally considered a hypothetical solid medium composed of two phases with different mechanical properties (Ulm and Abousleiman 2006). They hypothesized that a single indentation test evaluates the material properties of the probed phase if the indentation depth is much smaller than the characteristic size of the phase considered. This proposition allowed them to extract the mechanical properties and the probability of each phase, in terms of Gaussian distribution, by conducting a great number of nanoindentations.

Here, a new conceptual model is presented to interpret nanoindentations of a shale sample (Fig. 1.1). The hypothesis is that the elastic properties of a shale formation at the core scale can be predicted when accounting for the effective stiffness of the constitutive entities at a large scale (**hypothesis I**). This effective stiffness can be determined from nanoindentation, in which the local deformation of two entities with significantly different mechanical properties is mainly controlled by the softer entity at their contact point. Fig. 1.1a illustrates such interaction between two entities: an applied load causes a significant deformation of the softer entity, which is denoted in lighter color, whereas the stiffer entity remains almost undeformed. Δl in Fig. 1.1a represents the change in length. The effective stiffness is thus mainly associated with the mechanical properties of the softer entity, especially when the difference between their stiffness is significant. Our hypothesis implies that the applied load of nanoindentation gives access to the effective stiffness of the combined volume, instead of the properties of the probed entity body.

A shale sample consists of entities with different levels of stiffness. It is difficult to determine the spatial distribution and topology of the entity in the packing. Fig. 1.1b illustrates a packing as an example to shed light on the difficulty; different colors show the stiffness of each entity, with darker color representing increasing stiffness. Fig. 1.1b is for clarification, and there is no emphasis on any specific packing. Because the entities are randomly distributed, it is impossible to independently determine the effective stiffness of their bulk volume a priori.

The first hypothesis allows us to determine the mechanical properties of the bulk medium from nanoindentations. When an indentation load is applied on a specimen surface, a combination of the entities forms a loading frame (the dotted line in Fig. 1.1b) to sustain the load. The extracted properties from a nanoindentation imply the mechanical response of a loading frame that incorporates a locally heterogeneous composite. This could help us determine the elastic properties of the bulk volume.

The main assumption is that the elastic behavior of a bulk shale at macroscale is controlled by the loading frames (Fig. 1.1c). Thus, the proposed conceptual model relates nanoindentation to core-scale properties by accounting for the pertinent properties of the loading frames, which cannot be easily determined from the grains. The core-scale elastic modulus of the Woodford shale will be predicted based on the conceptual model.

3.2. Predicting the core-scale Young's modulus based on the conceptual model

The conceptual model is applied to Woodford shale samples, whose nanoindentations are available in literature. Bobko (2008) collected several Woodford samples from a well located at Pontotoc County in Oklahoma. Using a Berkovich indenter, he conducted a number of nanoindentations, ranging from 219 to 287, on various samples. The applied load was 4.8 mN and the resulting penetration depth ranged from 736 to 820 nm, which is less than the typical characteristic dimension of the grains in Woodford shale (1 μm). He presented the measurements as a frequency density function in terms of the indentation modulus and hardness. This density function was then mathematically represented by a summation of several Gaussian distributions with the pertinent weighting coefficients. The sum of all the weighting coefficients was equal to 1. By minimizing the error between the mathematical representation and the actual density function, he determined three Gaussian distributions, each of which was characterized by a mean indentation modulus (M_1^n, M_2^n, M_3^n) and a corresponding fraction (f_1^n, f_2^n, f_3^n). Because shale is mechanically anisotropic, he conducted the above work in parallel to (x_1) and perpendicular to (x_3) the bedding planes.

The nanoindentation moduli of the distributions are used to determine the pertinent elastic moduli based on Eq. 2.4. The elastic modulus of the indenter (E_i) is much larger than that of the shale, and thus its corresponding term is ignored. To determine the elastic moduli in x_3 direction, υ_3 is assumed to be 0.3, which is measured based on triaxial tests on Woodford shale (Tran 2009). The elastic moduli in x_1 direction is determined by using υ_1 = 0.2, which is an assumed value because there is no reliable value for υ_1 in the literature for the formation analyzed. The assumed value is representative of υ_1 considering data published for other shales (Shukla et al., 2013) and other types of rock (Gercek 2007). This does not significantly introduce errors because an uncertainty of $\pm$0.1 in the Poisson's ratio only leads to a 5% derivation in the calculated elastic modulus, according to Eq. 2.4. Table 3.1 shows the computed elastic moduli, along with the corresponding fractions. In Table 3.1, the corresponding fractions of the nanoindentations are represented by f_1^n, f_2^n, and f_3^n. The x_1 and x_3 denote the directions parallel and perpendicular to the axis of symmetry, respectively.

Table 3. 1 – Means of elastic moduli (E_1^n, E_2^n, E_3^n) for Woodford shale obtained based on nanoindentations (Bobko 2008).

Depth (m)	f_1^n	E_1^n(GPa)	f_2^n	E_2^n(GPa)	f_3^n	E_3^n(GPa)
x_1 direction						
33.53	0.54	12.85	0.28	22.62	0.18	44.85
39.93	0.49	10.14	0.26	16.42	0.24	41.58
46.94	0.39	9.15	0.3	16.60	0.26	46.42
50.60	0.50	8.29	0.28	16.96	0.22	46.96
53.34	0.40	11.21	0.35	19.80	0.25	40.93
56.39	0.44	7.24	0.33	15.42	0.23	40.23
x_3 direction						
33.53	0.45	6.51	0.34	11.49	0.21	38.49
39.93	0.42	7.30	0.30	12.69	0.28	32.33
46.94	0.39	10.76	0.33	19.80	0.28	47.69
50.60	0.45	8.03	0.26	20.80	0.29	50.72
53.34	0.34	8.53	0.38	15.51	0.28	36.38
56.39	0.30	6.75	0.23	14.63	0.48	42.27

The scale dependency of the Poisson's ratio needs to be discussed. Strictly speaking, the relationship between the indentation and the elastic modulus is valid only when the corresponding Poisson's ratio is implemented at the same scale. Here, the

Poisson's ratio obtained from a large-scale measurement is used to derive the elastic modulus from the indentation modulus (Eq. 2.4). This is because there is no nano-scale measurement of the Poisson's ratio for the shales analyzed in the literature.

The elastic modulus at macroscale can be determined based on the conceptual model (Fig. 1.1). The proposed model indicates that when loads are applied on the surface of the bulk volume (Fig. 1.1c), the loading frames (Fig. 1.1b) sustain the loads in the nanogranular medium. Thus, one can predict the elastic modulus at the macroscale by accounting for the elastic properties of the loading frames. Each nanoindentation, when made sparsely, gives us the elastic modulus of a single loading frame. The core-scale elastic moduli are predicted from the means of the elastic moduli and their corresponding fractions, obtained from nanoindentations, as follows:

$$E_n = \sum_{i}^{m} E_i^{ni} f_i^{ni} , \tag{3.1}$$

where E_n is the predicted elastic modulus at the macroscale, m is the number of distributions used to fit the mathematical model to the measurements, and E_i^n is the mean of the elastic moduli in the distributions whose corresponding fraction is denoted by f_i^n.

It is assumed that the loading frames act in parallel (Fig. 1.2b). Thus, the total load in the bulk medium is the sum of the corresponding loads in each loading frame. The load balance yields the relationship proposed in Eq. 3.1. There are other averaging schemes that are not realistic for the proposed assumption. One of them is volume averaging, which will be discussed later. Other averaging schemes are not tested because they are not realistic given the fundamental assumptions in this study.

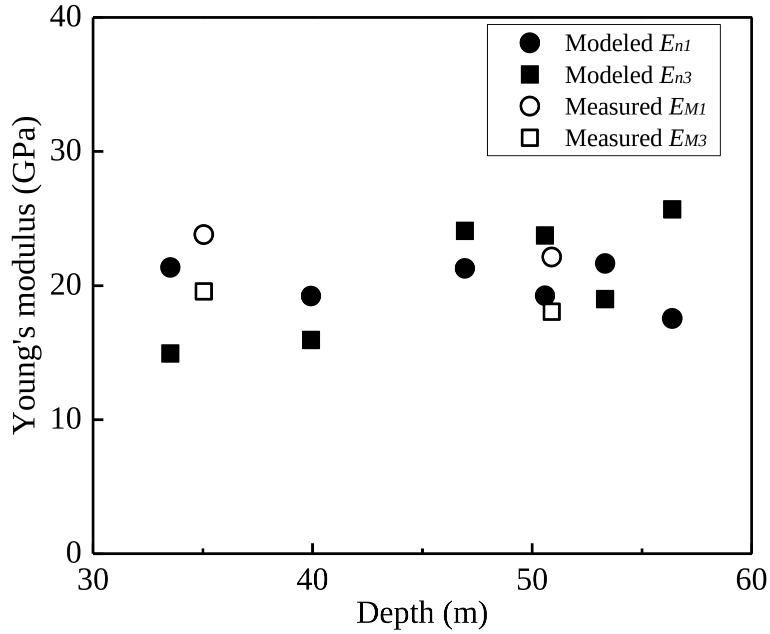

Figure 3.1 – Predicted elastic moduli (E_{n1} and E_{n3}) of Woodford shale are close to the macro-scale elastic moduli (E_{M1} and E_{M3}) measured by ultrasonic pulse velocity (Tran 2009).

The predicted elastic moduli are compared with the measurements of core-scale samples of Woodford shale from Pontotoc County in Oklahoma (Tran 2009). Fig. 3.1 presents the results. The core-scale samples were loaded using an inclined direct shear-testing device and an ultrasonic pulse velocity (UPV) technique was used to obtain the elastic properties. The confining stress was equal to 13.79 MPa, and the sample's diameter and thickness were equal to 20 mm and 7.6 mm, respectively. In this measurement method, UPV signals are emitted and travel through the sample in x_1 and x_3 directions. The velocities of the signals determine the core-scale elastic moduli E_{M1} and E_{M3}, according to Eqs. 2.14 and 2.15. In Fig. 3.1, the predicted and measured moduli are representative of the dynamic loading, where the subscript "1" and "3" denote directions parallel and perpendicular to the bedding plane, respectively.

The UPV measurements give the dynamic elastic modulus, which is consistent with nanoindentations, considering the nature of the loading. In nanoindentation, the elastic modulus is derived from the unloading section of the load-displacement curve, which is representative of a dynamic elastic modulus, not a static value (Zoback 2010).

The predicted elastic moduli based on nanoindentations (E_{n1} and E_{n3}) are close to the independent core-scale moduli (E_{M1} and E_{M3}) in the literature (Tran 2009). The average E_{n1} differs less than 13.2% from the measured E_{M1}, while the average E_{n3} deviates from the relevant E_{M3} for 9.3%. Therefore, the agreement between the predicted values and lab-measured values verifies the first hypothesis (**test of hypothesis I**). Hence, the conceptual model can help us predict the macroscale elastic modulus using nanoindentations. However, the predicted elastic moduli do not always follow the anisotropy trend observed at the large scale. The large-scale elastic modulus is larger in the x_1 direction, in contrast to the predicted moduli. This inconsistency is also present in the original nanoindentation moduli reported (Bobko 2008). One possible explanation for this is that the anisotropy is scale-dependent, and nanoindentations cannot capture the anisotropy at a larger scale, even if the predicted results remain close to the actual large-scale measurements. Thus, the predicted elastic moduli cannot necessarily capture the large-scale anisotropy.

3.3. Determination of the core-scale Young's modulus based on the volume fraction of the minerals

The proposed conceptual model indicates that the effective properties of two entities are mainly determined by the softer entity in local deformation, which enables us to obtain a good estimate of the elastic modulus at the core scale (Fig. 3.1). Another competing hypothesis is that the effective properties are controlled by the elastic properties of both entities at the small scale. The latter hypothesis allows us to predict the elastic modulus at the core scale by accounting for the volume fractions of the forming entities. Here, the latter hypothesis is applied to predict the elastic modulus at the core scale, which is compared with the independent core-scale measurements for validation.

Eq. 3.2 enables us to predict the elastic modulus at the core-scale by accounting for the elastic properties of each forming mineral and its volume fraction, as follows:

$$E^m = \sum_i^m E_i^m f_i^m \, , \tag{3.2}$$

where E^m is the predicted Young's modulus at the macroscale, E_i^m is the Young's modulus of each mineral, and f_i^m is the corresponding volume fraction of the mineral. The elastic modulus of each mineral has been extensively reported in the literature (Table 3.2), and the volume fraction of each mineral was determined by X-ray diffraction (XRD). Eq. 3.2 predicts the elastic modulus of the bulk medium as the volume average of the elastic properties of the forming constituents.

The elastic properties of clay minerals are rare in the literature because they are too small to be tested in pure solid form. It is even more difficult to measure the anisotropic properties of clay minerals (Sayers and den Boer 2016). Most of the measurements are conducted on composite clays, in which the orientation of the clay minerals lies in random directions (Wang et al., 2001). The measured results are thus the average values, which represent the volume deformation of clays, as shown in Table 3.2.

Table 3.2 – Volume fractions of minerals in Woodford shale with depth (Abousleiman et al., 2007), with the Young's modulus of each mineral.

Depth (m)	Kerogen	K-Feldspar	Kaolinite	Illite	Chlorite	Plagioclase	Calcite	Quartz	Ankerite	Dolomite	Pyrite
33.7	0.18	0.02	0	0.2	0	0.01	0.01	0.53	0.02	0	0.03
47.0	0.14	0.02	0	0.29	0.03	0.03	0	0.36	0.05	0.04	0.04
47.2	0.175	0	0	0.25	0.03	0.03	0	0.31	0.04	0.03	0.13
53.4	0.12	0.02	0	0.31	0.05	0.03	0	0.34	0.07	0	0.06
56.6	0.14	0.02	0.03	0.29	0.04	0.03	0	0.27	0.08	0.06	0.03
E_i^m (GPa)	6.2[a]	39.7[a]	56.8[b]	66.6[b]	76.6[b]	69.0[a]	84.3[a]	94.5[a]	98.9[a]	116.6[a]	260.6[a]

[a] Mavko et al., 2009; [b] Wang et al., 2001.

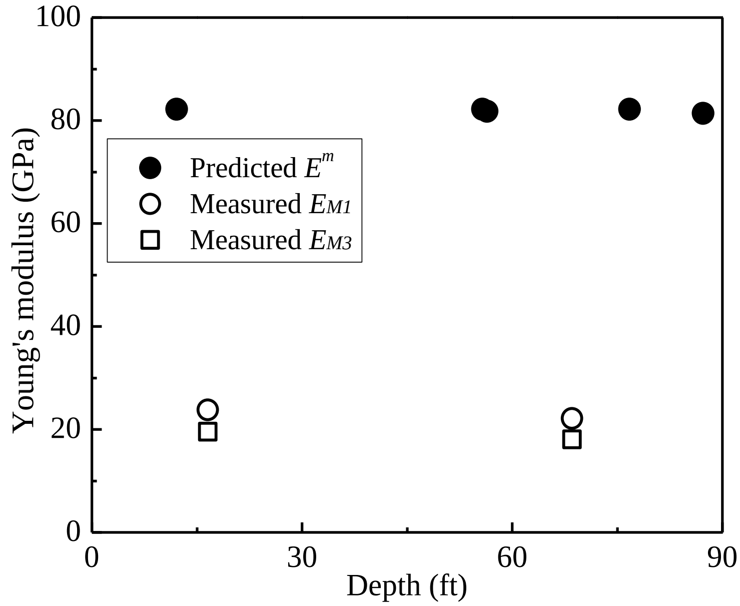

Figure 3.2 – Predicted Young's Moduli of Woodford shale based on the volume fraction. The predicted Young's moduli are significantly greater than the macroscale values obtained from independent measurements (Tran 2009).

Fig. 3.2 shows the predicted elastic moduli at core-scale for various Woodford samples, along with the lab-measured values. The predicted elastic moduli are isotropic because only the volume fraction of each mineral is considered. The predicted values are notably larger than the lab measurements because the interaction of adjacent entities is ignored in the volume averaging, which overestimates of the contribution of the harder minerals to the elastic behavior of the bulk medium. The conceptual model addresses this issue, thus achieving a better estimation of the elastic properties at the macroscale.

Isotropic elastic moduli have been used to implement the volume-averaging approach, and the predictions significantly overestimate the elastic properties of the bulk medium. The predicted results will not change significantly even if anisotropic values for the minerals (clays) are used. Thus, the main conclusion is still valid, even though isotropic properties simplify the elastic behavior of the forming minerals.

3.4. Discussion

Further discussion is need to investigate the contribution of the loading frames associated with the largest fraction (f_1^n) to the bulk property (E_n). For this reason, Fig. 3.3 presents the ratio of the contributions of these loading frames ($E_1^n f_1^n$) to the predicted Young's modulus (E_n). This ratio is smaller than 0.33, simply because the mean of the elastic moduli (E_1^n in Table 3.1) is small. These loading frames present elastic moduli close to that of kerogen, as shown in Table 3.2. However, the fractions of these loading frames, derived from nanoindentations, are significantly larger than the volume fraction of kerogen. This discrepancy is consistent with the conceptual model, in which it is postulated that the local effective stiffness is determined by the softer entities, even if they are not perturbed directly. Thus, the conceptual model explains why the nanoindentations yield a larger fraction for the softest loading frames compared to the volume of the softest mineral (kerogen) listed in Table 3.2.

The low elastic modulus associated with the largest fraction may be caused by the presence of small-scale fractures in a shale. However, the impact of the microcracks on the nanoindentation measurements may be negligible, for the following reason: In nanoindentation, the sample is confined locally, due to the indenter's compression. The typical nanoindentation load and projected area are on the order of 1 mN and 10^{-12} m^2, respectively. Thus, the mean contact stress is on the order of 1 GPa where penetration takes place. Under such high stress, the microcracks relevant to the load frame are most likely to be closed. Although microcracks far from the loading frame may remain partially open, their influence on the active nanoindentation may be negligible.

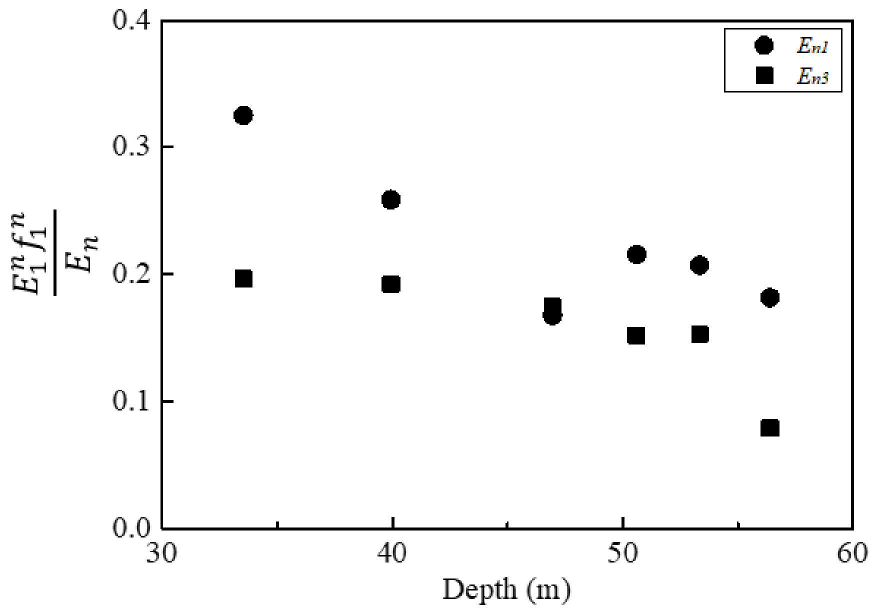

Figure 3.3 – Contribution of the loading frames with the largest fraction (f_1^n) to the Young's modulus (E_n) of the nanogranular medium is smaller than 0.33 in Woodford shale.

3.5. Conclusions

A conceptual model was proposed to predict the elastic properties of a shale formation at the core-scale based on nanoindentations. The model is based on the assumption that the elastic properties of shale at the core scale can be captured if one accounts for the effective stiffness of the small-scale constitutive minerals that have different mechanical properties. The effective stiffness of different minerals was determined from the local deformation in nanoindentations. The proposed model was applied to Woodford shale, and the predicted elastic moduli agreed with independent core-scale measurements.

The core-scale elastic properties of shales were also determined from the volumetric average of the properties of the constitutive minerals. In this case, the computed core-scale elastic properties significantly overestimated the elastic properties of the bulk volume. This proves that it is necessary to account for the effective stiffness of different minerals when estimating the core-scale properties of shales.

The proposed model is important because it provides a proper interpretation of nanoindentations of shale, which is heterogeneous. The proposed model also has practical applications in predicting the core-scale elastic properties of shales from nanoindentations that can be conducted on drill cuttings.

Chapter 4. A Hierarchical Model for Predicting the Elastic Properties of Shales at the Core Scale

The content of this chapter has been published in *SPE Reservoir Evaluation & Engineering* (Sakhaee-Pour and Li 2018). A hierarchical model is proposed to predict the core-scale elastic properties of shales from the mineralogy, porosity, pore structure, and grain-size distribution. The hierarchical model includes a small-scale model, which mimics the elastic deformation of a grain with a known mineralogy, and a large-scale model, which captures the elastic properties of shales at the core scale.

4.1. A hierarchical model of the elastic deformation of a shale

4.1.1. Small-scale (grain-scale) model

A physically representative element is developed to capture the elastic deformation of a grain with a known mineralogy. This is relevant to the small-scale (grain-scale) analysis of the hierarchical model which is shown in Fig. 1.2. The large-scale (core-scale) model is discussed subsequently.

It is assumed that the matrix of a shale is composed of solid grains, porous kerogen, and porous clay aggregates, based on the high-resolution images available in the literature (Loucks et al., 2009; Akrad et al., 2011; Jin and Sonnenbergy 2013; Milliken et al., 2013). The solid grains with no porosity, which are non-clay and non-kerogen, are relevant to quartz, feldspar, calcite, dolomite, pyrite, and apatite minerals.

The geometry of the representative element is a cube rather than a sphere, which is often used to represent the grains (Herrmann and Luding 1998; Bobko and Ulm 2008), for various reasons. A sphere is relatively similar to a solid grain, which is one of the main reasons that spheres are used to model unconsolidated sandstones (Bryant and Blunt 1992). But the similarity is unclear in shale formations because the matrix undergoes significant change and secondary processes, such as compaction and cementation, after the solid grains are deposited.

Further, shale formations have a low pore connectivity, which is more similar to the acyclic-pore model (Sakhaee-Pour and Bryant 2015; Sakhaee-Pour and Li 2016; Zapata and Sakhaee-Pour 2016). In the acyclic-pore model, there is a unique path between any two points, whereas the pore space in the sphere-packing model has a high connectivity, with many paths between two points, which is not realistic for shale formations. Although the pore connectivity may not change the geomechanical properties, a cube-packing model is more realistic because its pore connectivity can be assigned to be representative of a shale. The pore connectivity in the pack-of-cubes model is unstructured, as opposed to the cyclic pattern in the sphere-packing model (Bryant and Blunt 1992).

Simplicity is another reason for using a cube for the geometry of the representative element. A variety of finite-element models have been developed and can be used for cubic elements. In the present study, the effective properties of the representative elements are determined such that they mimic the solid grains, porous kerogen, or clay aggregates in the matrix of a shale. Thus, the geometry of the representative element does not play an important role in the numerical results, and other geometries may also be used.

The main objective in developing a representative element is to simulate the elastic compression of the grain. Thus, the elastic modulus of the representative element is determined such that its elastic deformation becomes equal to that of the grain for a given pure compression. The compressive stiffness of the representative model is set to be equal to that of the mineral as

$$\frac{E_r A_r}{L_r} = \frac{E_m A_m}{L_m}, \tag{4.1}$$

where E_r is the elastic modulus of the representative element, A_r is the cross-sectional area of the representative model, L_r is the length of the representative model, $E_m$is the elastic modulus of the mineral, A_m is the cross-sectional area of the corresponding grain, and L_m is the corresponding characteristic length of the grain. The grain sizes can be obtained from high-resolution images using X-ray diffraction (XRD) coupled with a scanning electron microscope (SEM) (Milliken et al., 2012). It can also be obtained from a quantitative electron microscope scanner (QEMSCAN), as has been demonstrated by Jin and Sonnenbergy (2013). An average grain size is used in this study and its effect on the predicted results is clarified below.

To model the elastic deformations of porous kerogen and porous clay aggregates, the void space that resides inside them and the pore structure needs to be accounted for. It is assumed that the voids reside equally in the kerogen and the clay due for reasons of practicality. High-resolution images allow us to investigate the spatial distribution of pore space in kerogen and clay, but such investigations are limited to rock samples of a small size (4−50 μm). It is difficult, although possible, to determine the spatial distribution of pore space at the core-scale (~ 2.5 cm) based on the images. The assumption allows us to determine the void space inside the kerogen and the clay as

$$\phi_{kerogen} = \phi_{clay} = \frac{\phi_{total}}{f_{clay} + f_{kerogen} + \phi_{total}}, \tag{4.2}$$

where ϕ_{total} is the total porosity determined by helium porosimeter; f_{clay} is the volume fraction of the clay minerals; $f_{kerogen}$ is the volume fraction of the kerogen; $\phi_{kerogen}$ is the local porosity of the porous kerogen, and ϕ_{clay} is the local porosity of the clay aggregates.

The pore structure also plays an important role in the effective properties at the small scale (grain scale). A crack-like pore decreases the elastic modulus of the host grain more than a spherical pore does. In the proposed model, the effect of the pore structure is implemented via aspect ratios. It is supposed that the aspect ratios of the pores inside the kerogen and the clay aggregates are equal to 1/3 and 1/20, respectively, based on the data available in the literature. Locuks et al., (2009) reported that the aspect ratio of the pores in kerogen changes from 1/1.8 to 1/4.8 in Barnett shale. The aspect ratio of the pores in clay aggregates is close to 1/20 (Hornby et al., 1994), which is much smaller, because of the sheet-like geometry of a clay particle.

The effective elastic modulus of a porous grain (the porous kerogen and clay aggregates in Fig. 1.2) is determined using a finite element method. The elastic properties of the pores are set equal to zero and those of the host solid minerals are based on the data available in the literature. The determined effective elastic modulus allows us to obtain the corresponding elastic modulus of the representative element.

The elastic modulus of the representative element is determined, while its size is assumed to be identical for different minerals. This assumption facilitates developing a large-scale model because the representative elements can match easily, and there will be no non-matching nodes, which is a famous problem in finite element analyses (Arbogast et al., 2000). The corresponding grain size of each mineral and the elastic properties of the minerals are available in the literature (Table 4.1). Thus, the elastic modulus of the representative model is the only unknown in Eq. 4.1.

The size of the representative element is assumed to be equal to 1 μm, which is different than the grain size measured from high-resolution images. Both element and grain sizes are used to derive the elastic modulus of the representative element according to Eq. 4.1. The element sizes for different minerals are specified to be 1 μm because this facilitates the development of a large-scale model. It is also assumed that the cross-sectional area of the grain is proportional to the squares of the length ($A \sim L^2$) to determine the elastic modulus of the representative element. Table 4.1 lists the elastic moduli of the representative elements for different minerals found in Barnett shale. Barnett shale is analyzed in this study as an example because its properties are available in the literature.

Because the effective compressive stiffness of the representative element is equal to that of the grain with a known mineralogy, the displacements of equal compressive forces applied to both are equal. The Poisson's ratio of the representative element remains that of the grain. The equality of the Poisson's ratios forces the lateral displacements of the two to be equal for the specified compression, because the Poisson's ratio dictates the ratio of the lateral to the vertical displacements.

The average grain size (L_m) reported for each mineral in Barnett shale is used to determine the elastic properties of the representative element (Table 4.1). Milliken et al. (2012), after performing an extensive image analysis, reported that the grain size is on the order of 5.9−19.2 μm. The elastic modulus of the representative element, which is used in the core-scale model (Fig. 1.2), is computed for each mineral such that the effective stiffness, and not necessarily the elastic modulus, remains equal to that of the mineral in the matrix. The sensitivity of the results to the grain size will be discussed in a later section.

For porous kerogen and clay aggregates in Table 4.1, effects of the local porosity and pore structure are also considered. The total porosity of the samples, which is 9.4% (Vermylen 2011), is changed to the local porosity in kerogen and in clay aggregates (Eq. 4.2). The aspect ratio of the pores in kerogen is equal to 1/3 (Locuks et al. 2009) and in clay aggregates to 1/20 (Hornby et al. 1994).

Table 4.1 – Elastic properties of the representative elements. The elastic properties are determined by accounting for the elastic properties and characteristic size of each mineral.

		Mineral					Representative elements	
		Density, g/cm^3	Young's modulus (E_m), GPa	Poisson's ratio[a]	length[c] (L_m), μm	Stiffness (k_r), N/μm	Young's modulus (E_r), GPa	Poisson's ratio
Kerogen		1.30[a]	6.2[a]	0.14	12.55	0.08	77.8	0.14
Clays	Kaolinite	2.44[b]	56.8[b]	0.285	12.55	0.71	712.8	0.285
	Illite	2.75[b]	66.6[b]	0.315	12.55	0.84	835.8	0.315
	Chlorite	2.68[b]	76.6[b]	0.266	12.55	0.96	961.3	0.266
Feldspar (orthoclase)		2.62[a]	39.7[a]	0.32	12.55	0.50	498.3	0.32
Plagioclase (albite)		2.63[a]	69.0[a]	0.35	12.55	0.87	866.0	0.35
Calcite		2.71[a]	84.3[a]	0.32	12.55	1.06	1057.9	0.32
Quartz		2.65[a]	94.5[a]	0.08	12.55	1.19	1185.9	0.08
Ankerite		3.05[a]	98.9[d]	0.32	12.55	1.24	1241.2	0.32
Dolomite		2.87[a]	116.6[a]	0.30	12.55	1.46	1463.0	0.30
Apatite		3.21[a]	146.7[a]	0.21	12.55	1.84	1841.3	0.21
Pyrite		4.81[a]	260.6[a]	0.19	12.55	3.27	3270.4	0.19
Marcasite		4.08[a]	305.8[a]	0.19	12.55	3.84	3838.5	0.19

a Mavko et al., 2009; b Wang et al., 2001; c Milliken et al., 2012; d Zhu et al., 2009.

4.1.2. Large-scale (core-scale) model

A large-scale (core-scale) model is developed based on the representative element for shales. The spatial distribution and the number of representative elements in the model are discussed first. Then, the elastic modulus of the large-scale model is derived and related to the elastic modulus of the rock. Because grains are deposited randomly, the representative elements with different elastic properties are randomly distributed in the large-scale model. Different realizations are generated to determine the sensitivity of the results to the distribution.

It is impossible to include all the minerals in the large-scale model if the number of the representative elements is small. The volume fraction of some minerals is as small as 1%. Thus, the total number of representative elements in the large-scale model is determined such that each mineral is represented. The number of representative elements for each mineral can be calculated as

$$N_i = N_t f_i,\ i = 1 \text{ to number of minerals}, \quad (4.3)$$

where N_t is the total number of representative elements in the large-scale model, N_i is the number of the representative element for each mineral, f_i is the volume fraction of each mineral, and the subscript i denotes the mineral.

The volume of the large-scale model is calculated based on the number of the representative elements as follows:

$$V_M = N_t V_r = N_t L_r^3, \quad (4.4)$$

where V_M is the total volume of the large-scale model, N_t is the total number of the representative elements, V_r is the volume of the representative element, and L_r is the size of the representative element.

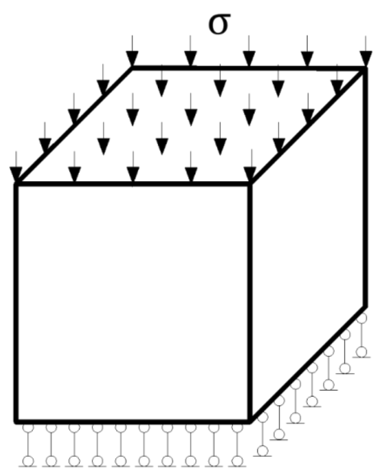

Figure 4.1 – Schematic illustration of the loading and the boundary conditions of the large-scale model for elastic compression of a shale.

Finite element analysis is performed to calculate the elastic modulus of the large-scale model. A uniform compression to one end of the large-scale model is specified and the other end is roller constrained (Fig. 4.1). The finite element model allows us to determine the stress, strain, and elastic modulus of the large-scale model as follows:

$$\sigma = \frac{P}{A_M}, \tag{4.5a}$$

$$\varepsilon = \frac{\Delta L_M}{L_M}, \text{ and} \tag{4.5b}$$

$$E_M = \frac{\sigma}{\varepsilon}, \tag{4.5c}$$

where σ is the normal stress, P is the compressive uniform force applied to the model, A_M is the cross-sectional area of the model perpendicular to the loading direction, ε is the strain parallel to the applied load, L_M is the length of the model, and ΔL_M is the change in the length of the model parallel to the applied force.

The elastic modulus of the shale is calculated based on the large-scale model. The model is based on the equivalency of the effective stiffness and not on the elastic moduli.

Hence, the computed elastic modulus has to be converted to that of the natural granular medium. The total volume of the granular medium can be determined from the total number of the representative elements and the volume fractions as

$$V_R = \sum_{i}^{m} N_i V_i, \tag{4.6}$$

where V_R is the modeled rock volume, N_i is the number of the representative elements for each mineral, V_i is the volume of each mineral, and m is the total number of minerals in the sample.

The elastic modulus of the shale is determined based on the elastic modulus of the large-scale model (E_M). The effective stiffness of the model is equal to that of the rock as

$$\frac{E_R A_R}{L_R} = \frac{E_M A_M}{L_M}, \tag{4.7}$$

where E_R is the elastic modulus of the rock, A_R is the cross-sectional area of the rock, L_R is the characteristic length of the rock, E_M is the elastic modulus of the model, A_M is the cross-sectional area of the model, and L_M is the length of the model. The right side is known from the large-scale model. The geometric parameters of the modeled rock sample (A_R and L_R) are also known because the corresponding volume is specified. Thus, the elastic modulus of the rock sample, which is the only unknown in Eq. 4.7, can be computed using the large-scale model.

4.2. Results

The elastic deformation of a Barnett shale sample (B1) was analyzed using the relevant data in Table 4.2. The mineralogy of the sample was analyzed using XRD, which determines the volume fraction of each mineral by accounting for its density (Abedi et al., 2015).

The accuracy of the large-scale model was tested based on the representative element for a single mineral. For this, a large-scale model with a single mineral was developed to simulate its elastic deformation. The difference between the computed elastic modulus and that of the mineral was less than 1% when the number of the representative elements was larger than or equal to 64 (= 4 × 4 × 4).

Fig. 4.2 shows the predicted elastic moduli of the Barnett shale sample (B1 in Table 4.2). The elastic deformation of the large-scale model is computed using different numbers of elements. For a given number of elements, 10 random realizations were generated for the spatial distribution of the minerals in the model.

To capture the formation heterogeneity at the core scale, it is assumed that the representative elements, which are relevant to various minerals, porous kerogen, and clay aggregates, are randomly distributed. This is based on the assumption that the solid grains are deposited randomly under gravity. No specific pattern is considered in this process; thus, the developed model may not capture the formation anisotropy. The trends using random spatial distribution could be used to extend the model for capturing the anisotropic behavior of shale; however, capturing such anisotropic behavior is beyond the scope of this chapter and will be discussed in chapter 6.

Next, the sensitivity of the large-scale model to the number of elements is discussed. The average of the calculated elastic moduli changes less than 1% when the number of elements is increased from 20 × 20 × 20 to 30 × 30 × 30, and from 20 × 20 × 20 to 40 × 40 × 40. Hence, the presented average elastic moduli (filled symbols in Fig.

4.3) are not sensitive to the number of the elements in the large-scale model when more than 20 × 20 × 20 elements are incorporated. Further sensitivity analysis of the proposed model for granular heterogeneous media is beyond the scope of the present study.

Fig. 4.2 also shows the variation of the measured elastic moduli, which are representative of the static deformation of intact samples at the core scale (Sone 2012), for the same formation. The measured elastic moduli parallel to the bedding plane vary from 37.4 to 46.9 GPa. The measured elastic moduli perpendicular to the bedding plane vary from 22.7 to 27.1 GPa. The average of the predicted elastic moduli is 41.81 GPa in the large-scale model with the large number of elements. Thus, the predicted elastic modulus is closer to the measured value parallel to the bedding.

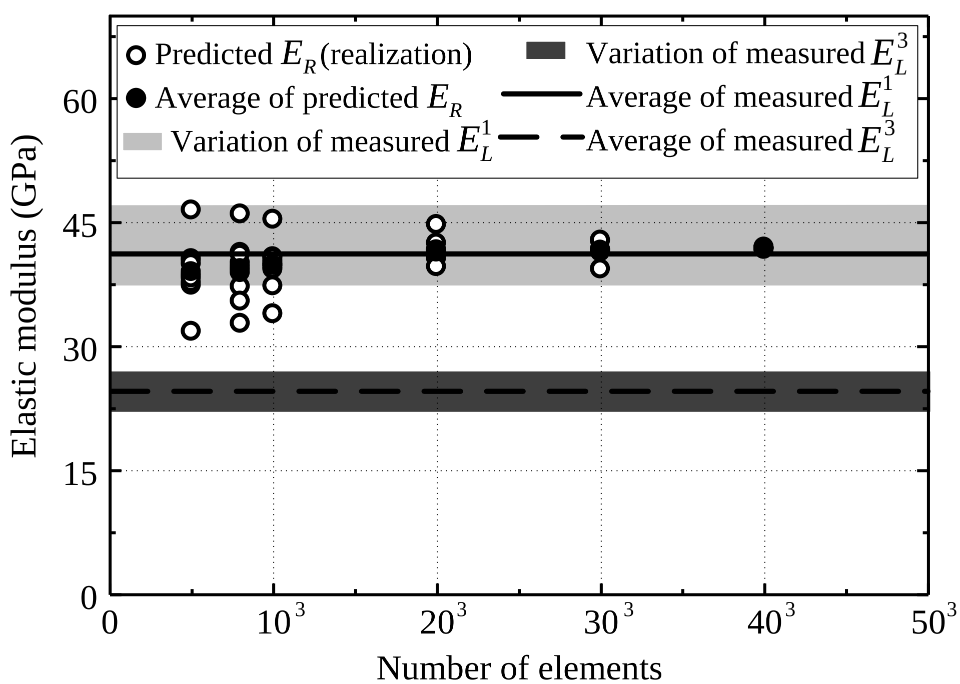

Figure 4.2 – Predicted elastic moduli (E_R) of a Barnett sample (B1) whose relevant data are listed in Table 4.2.

In Fig. 4.2, the filled symbols represent the average of the predicted moduli among different realizations. The average of the predicted moduli is not sensitive to the number of elements when it is larger than 20 × 20 × 20. Moreover, the realizations (empty symbols) are not sensitive to the number of elements when 40 × 40 × 40 elements are included in the large-scale models.

In the large-scale model, it is also observed that the difference between the maximum and minimum elastic moduli becomes smaller as the number of elements increases. For instance, the maximum and minimum moduli are equal to 46.45 and 31.76 GPa, respectively, when the model includes 5 × 5 × 5 elements (Fig. 4.2), but the predicted elastic moduli become almost equal when 40 × 40 × 40 elements are used. The larger difference between the predicted moduli arises because the large-scale model is not realistic for a random distribution when only a few elements are included, an issue which is resolved by increasing the number of elements.

The developed model is based on the random spatial distribution of the representative elements. Any statistical model becomes representative only when it includes a large population (Goovaerts 1997). The difference between the predicted results for different realizations is negligible when the model is large enough. This applies to the large-scale model as well, where the modeled population consists of the solid grains, porous kerogen, clay aggregates, and pores. Fig. 4.2 shows that the difference between the random realizations is negligible when there are 40 × 40 × 40 elements in the large-scale model. Thus, the model with 40 × 40 × 40 elements will be tested for various shale formations in the Validation section.

Table 4.2 – Mineral composition in mass percent for different shales. N1 is a New Albany shale sample (Salehi 2010), S1 – S4 are Siliceous Rocky Mountains shale samples (Daigle et al., 2017), LB1 – LB3 are Lower Bakken shale samples (Simpson et al., 2015), and B1 – B7 are Barnett shale samples (Vermylen 2011).

		N1	S1	S2	S3	S4	LB1	LB2	LB3	B1	B2	B3	B4	B5	B6	B7
Mineral composition by XRD (wt %)																
Kerogen		7.3	5.0	3.0	4.0	3.0	25.5	27.5	24.4	3.6	3.4	4.0	5.7	3.8	5.3	3.0
Clays	Kaolinite	0	1.0	1.0	1.0	0	0	0	0	0	0	0	0	0	0	0
	Illite	28.7	22.0	19.0	18.0	31.0	19.1	13.2	15.0	28.3	28.0	27.7	38.8	23.8	37.4	38.6
	Chlorite	0	1.0	1.0	1.0	2.0	7.2	12.1	0	0	0	0	0	0	0	0
Feldspar (orthoclase)		6.5	0	0	0	0	5.1	5.3	4.5	0	0	0	0	0	0	0
Plagioclase (albite)		5.6	8.0	13.0	8.0	8.0	2.1	2.1	2.1	4.2	3.7	5.3	4.3	3.8	4.0	4.8
Calcite		0	1.0	1.0	0	0	2.6	3.9	1.2	10.7	4.2	11.3	0.3	7.7	0	2.9
Quartz		36.1	52.0	52.0	60.0	50.0	29.6	26.1	44.1	48.8	49.2	43.5	48.2	56.7	51.3	42.7
Ankerite		0	0	0	0	0	0	0	0	0.8	0	0	0.1	0	0	2.3
Dolomite		11.1	2.0	3.0	4.0	2.0	3.6	3.5	4.3	1.1	10.1	2.3	0.2	1.4	0.4	2.8
Apatite		0	1.0	0	0	1.0	0	0	0	0.9	0	4.1	0.5	1.0	0	0
Pyrite		2.8	7.0	7.0	4.0	3.0	5.2	6.3	4.4	1.6	1.3	2.0	1.8	1.8	1.7	2.0
Marcasite		1.9	0	0	0	0	0	0	0	0	0	0	0	0	0	0
Total porosity (%)		5.91	9.7	8.5	8.9	7.0	9.1	6.6	8.1	9.4	9.4	9.4	9.4	8.6	10.7	9.0

The large-scale models associated with the maximum and minimum elastic moduli, which are relevant to two random realizations of the spatial distribution of the minerals, are further analyzed. The layers of the large-scale models for two numbers of elements (= $5 \times 5 \times 5$ and $20 \times 20 \times 20$) are plotted. The plotted layers that are parallel to the applied force can be considered as cross-sections of the model, where darker colors correspond to the minerals with higher elastic moduli (Figs. 4.3 and 4.4).

Fig. 4.3a shows that the representative elements with high elastic moduli form two loading frames (red dashed lines) when the predicted elastic modulus is at the maximum in the smaller model. There is no column comprising the elements with high elastic moduli when the overall value is at the minimum (Fig. 4.3b). The only difference between the two models, shown in Figs. 4.4a and 4.4b, is the spatial distribution of the representative elements because they both mimic identical volume fractions for the minerals.

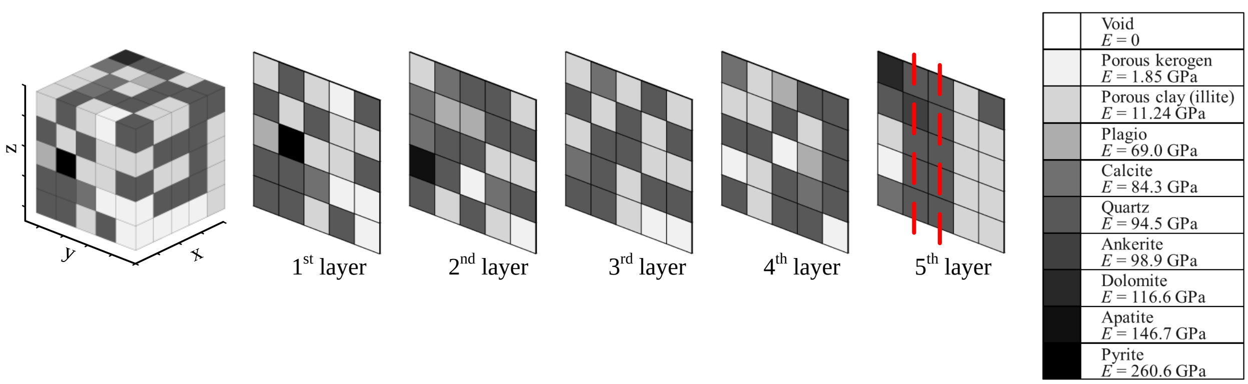

a.

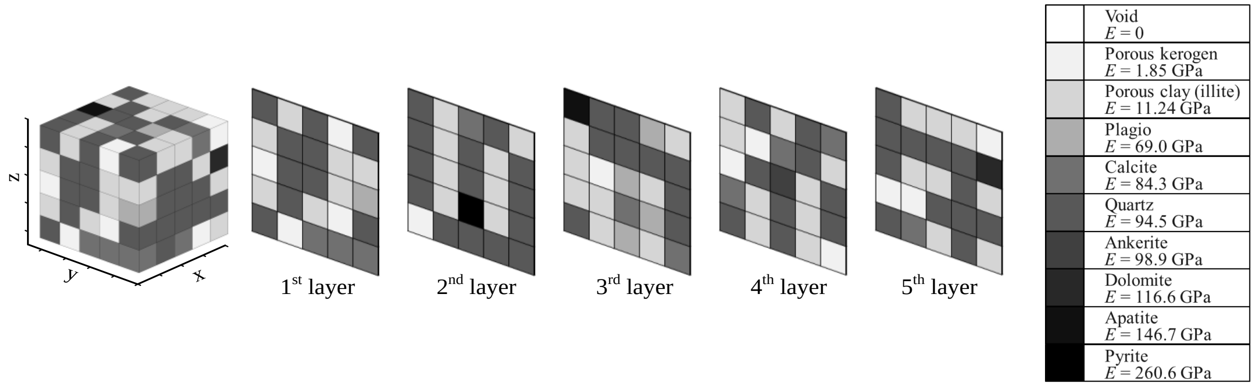

b.

Figure 4.3 – Cross-sections of the large-scale models, with 5 × 5 × 5 elements, whose elastic moduli are at the maximum (a) and at the minimum (b) in Fig. 4.2.

It is more likely for the representative elements that have high elastic moduli to form a loading frame in the smaller model when they are randomly distributed. In the larger model, the difference between the maximum and minimum elastic moduli is negligible. Figs. 4.4a and 4.4b show no significant difference between the cross-sections of the models, and no specific pattern is observed. Thus, the loading frames disappear when the spatial distribution of the minerals is random in the larger model.

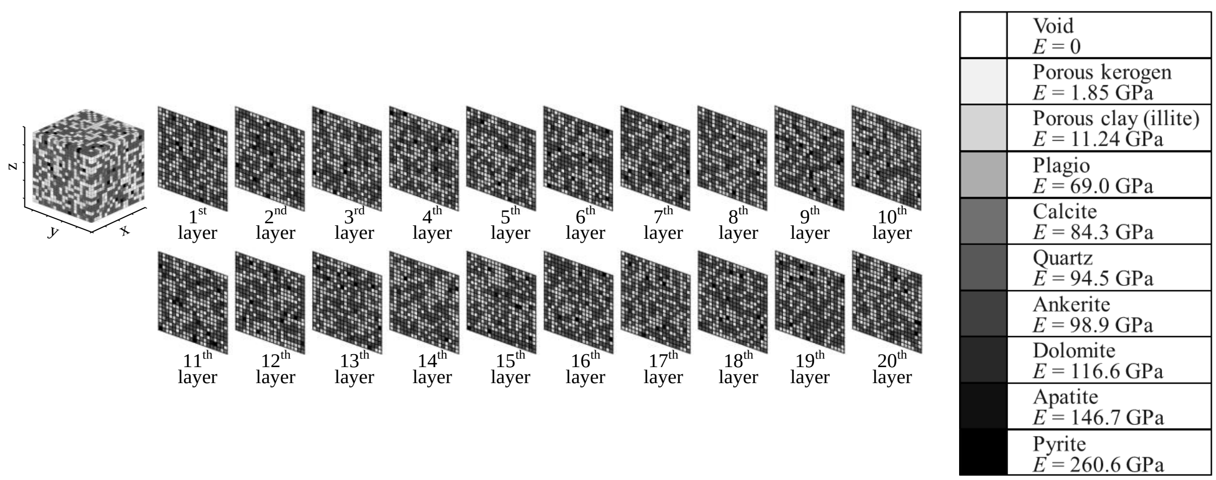

a.

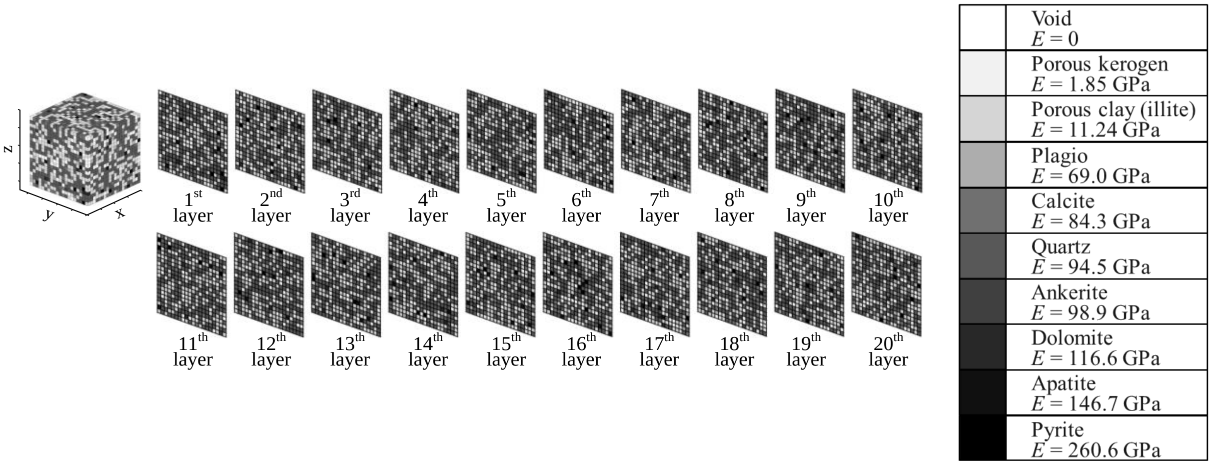

b.

Figure 4.4 – Cross-sections of the large-scale models whose elastic moduli are at the maximum (a) and at the minimum (b) in Fig. 4.2, respectively, when the total number of the elements is equal to 20 × 20 × 20.

4.3. Validation on four shale formations

The hierarchical model is tested for four shale formations whose data are available in the literature. The analyzed shales are New Albany (N), Rocky Mountain Siliceous (S), Lower Bakken (LB), and Barnett (B), whose mineral compositions are listed in Table 4.2. In the New Albany shale, the mineral composition of different samples remains almost identical with the depth where the core plug was recovered (Salehi 2010); hence, the listed mineral compositions are representative of the modeled core plug. In the Rocky Mountain Siliceous (Daigle et al., 2017) and the Lower Bakken shales (Simpson et al., 2015), the mineral compositions were reported for the investigated core plugs. One of the lab measurements from Rocky Mountain Siliceous is excluded in our analysis because its elastic modulus parallel to the bedding plane was 11 GPa. The sample was possibly damaged along the bedding plane. In the Barnett shale, the mineral composition and elastic moduli are related to the same well, and not necessarily to the same plug. Thus, the mineral compositions represent the core plugs more accurately in the first three shales (N, S, and LB) than in the Barnett shale (B).

The effective elastic properties shown in Table 4.1 are used to build the large-scale model. The number of the representative elements in the large-scale model is 40 × 40 × 40. The elastic properties of the solid grains, which are non-clay and non-kerogen, are identical to the values listed in Table 4.1. For porous kerogen and clay aggregates, the effect of the local porosity is also considered (Eq. 4.2).

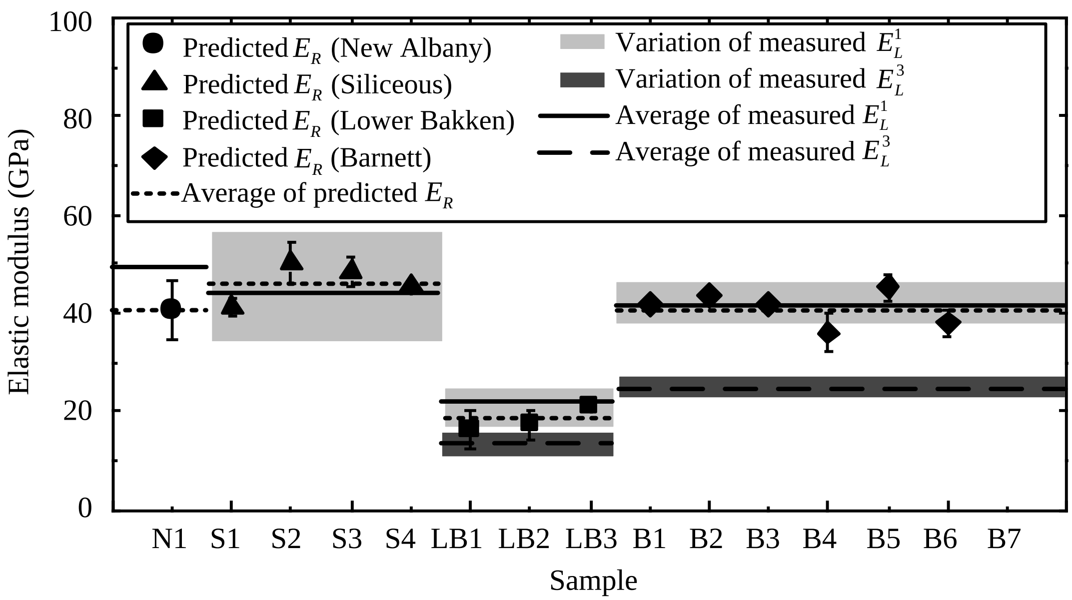

Figure 4.5 – Predicted elastic moduli of New Albany (N1), Rocky Mountain Siliceous (S1–S4), Lower Bakken (LB1–LB3), and Barnett (B1–B7) shales based on the hierarchical model.

The predicted elastic moduli are compared with independent lab measurements that were conducted on intact shale samples (Fig. 4.5). For the Rocky Mountain Siliceous (S1–S4), Lower Bakken (LB1–3), and Barnett (B1–7) samples, the predicted values cover the range reported parallel to the bedding (E_L^1). The average of the predicted values (dotted lines) are close to the average measurements (solid lines), with a difference of less than 15%. For the New Albany shale, the predicted elastic modulus is 40.43 GPa and is smaller than the only measurement available (48.96 GPa). Thus, the hierarchical model can capture the elastic properties of a shale formation parallel to the bedding more accurately, but overestimates the elastic properties of a shale perpendicular to the bedding. Table 4.2 lists the mineral compositions of the modeled shale samples.

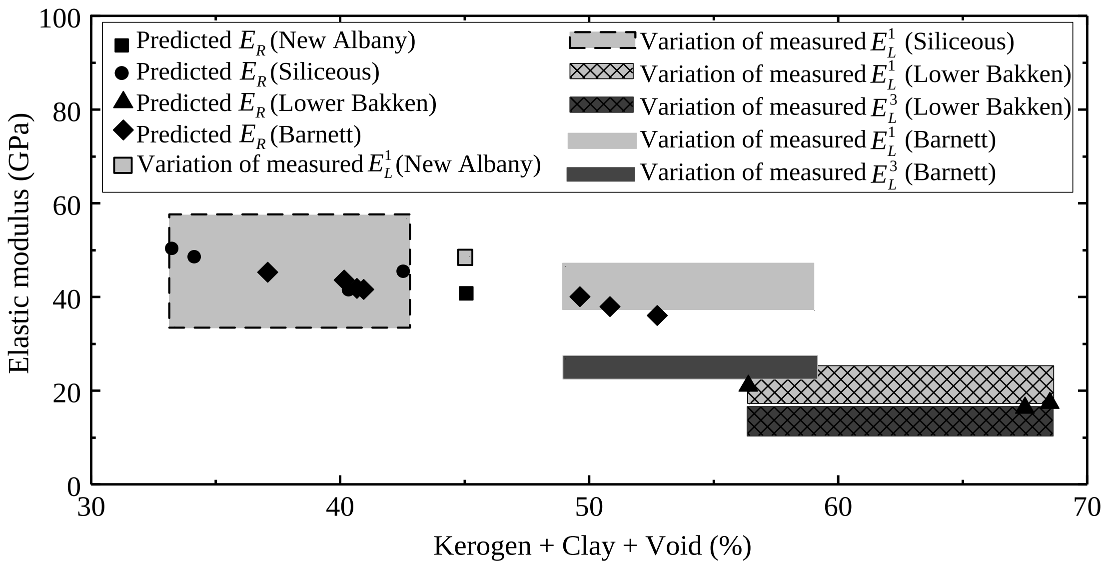

Figure 4.6 – Predicted elastic moduli based on the hierarchical model decrease with the increasing fraction of the kerogen + clay + void, consistent with the data available in the literature (Sone and Zoback 2013; Rybacki et al., 2015).

The proposed model captures the dependency of the elastic moduli on the volume fractions of kerogen + clay + void, which are the weaker components in the matrix of a shale. Fig. 4.6 shows the dependency, based on the proposed model, and compares it with lab measurements. The predicted elastic moduli decrease as the weak components increase, a phenomenon observed by different researchers for different shales (Sone and

Zoback 2013a; Rybacki et al., 2015). The predicted dependency provides further evidence that supports the hierarchical model.

4.4. Conclusions

A hierarchical model was proposed to predict the elastic properties of shales at the core scale from the mineral composition and the void system. In the small-scale model, a physically representative element was developed to mimic the elastic deformation of a grain with a known mineralogy in the matrix of a shale. The representative elements determine the effective elastic properties of the grain using its mineralogy, the local porosity, and the pore structure. In the large-scale model, the effective properties are determined by accounting for the volume fraction of each mineral. The predicted elastic moduli of shales, based on the proposed model, were tested against independent laboratory measurements for New Albany, Rocky Mountain Siliceous, Lower Bakken, and Barnett Shales. The predicted results are close to the measured elastic moduli parallel to the bedding plane.

The proposed model is important because it also allows us to characterize the geomechanical properties of shales from drill cuttings, instead of core plugs, which are difficult to recover due to the mechanical instability of shales. The model predicts the core-scale elastic properties of shales from the mineralogy, the porosity, the pore structure, and the grain-size distribution. All these factors can be determined from small-scale measurements on drill cuttings. The model also enables us to quantitatively determine the effect of heterogeneity on the core-scale properties of shales.

Chapter 5. A Hierarchical Model for Predicting the Elastic Properties of Carbonate at the Core Scale

The hierarchical model can be applied to predict the elastic properties of carbonates at the core scale from the mineralogy and the void system. Here, an example is presented of its application to the Arab-D carbonate formation in the Middle East. The content of this chapter has been published in *Rock Mechanics and Rock Engineering* (Li and Sakhaee-Pour 2018).

5.1. Introduction

Carbonate formations constitute close to half of the world's oil reserves (US EIA 2017), yet researchers have a limited understanding of their fundamental behavior because of their complex pore structures (Dunham 1962; Lucia 2007). The reservoir characterization of these formations becomes more complicated in the presence of karsts (Gritto et al., 2014). Understanding the geomechanical properties of carbonate formations, which could reduce the exploitation cost, will be of increasing importance in years to come, especially if oil prices remain low.

Mineral composition has a profound effect on the geomechanical properties of carbonate formations at the core scale because various minerals show distinct mechanical properties (Mavko et al., 2009). Calcite and dolomite usually constitute the main fraction of the minerals in carbonate formations, where anhydrite may account for a small fraction (Cantrell and Hagerty 1999 and 2003; Cantrell et al., 2004). Other minerals, such as quartz, kaolinite, smectite, barite, feldspar, fluorite, illite, and pyrite, may also be present in the carbonate matrix (Rogen et al., 2005). Calcite is a carbonate mineral ($CaCO_3$)

whereas dolomite is an anhydrous carbonate mineral with calcium magnesium carbonate ($CaMg(CO_3)_2$). Calcite and dolomite have different crystal structures and physical properties (Lucia 2007).

The geomechanical properties of carbonates at the core scale depend on the porosity and the pore structures. Carbonate rocks have a variety of pore types, such as vugs, molds, interparticles, micropores, and others (Choquette and Pray 1970; Lucia 1995; Eberli et al., 2003). These pore types, which have varied topologies, cause a large scatter of the mechanical properties of a particular carbonate at equal porosity (Eberli et al., 2003; Sayers 2008). Difficulties remain in quantitatively relating the pore system to the geomechanical properties of carbonates at the core scale (Xu and Payne 2009).

Researchers have conducted triaxial measurements on core plugs to understand the geomechanical properties of the carbonates (Ameen et al., 2009; Croize et al., 2010; Santos and Ferreira 2010; Neveux et al., 2014; Walton et al., 2015). While core-scale measurements provide useful information about a formation, these measurements cannot be made on drill cuttings and are time consuming and expensive. Thus, researchers have tried to predict the large-scale properties based on porosity, forming minerals, and nanoindentations (Xu and Payne 2009; Saenger et al., 2016).

Researchers have proposed several models for predicting the geomechanical properties of a carbonate formation based on porosity, most of which have been empirical (Farquhar et al., 1994; Edimann et al., 1998). Their results show that the geomechanical properties correlate poorly with the porosity and that the pore structure plays an important role in the geomechanical properties of the formation at the core scale. Many studies have been conducted to evaluate the effect of the pore structure on the elastic behavior of the carbonates (Eberli et al., 2003; Rogen et al., 2005; Sayers 2008; Weger et al., 2009; Xu and Payne 2009; Walton et al., 2015). The main conclusion is that, for a given total porosity, the round pores provide more grain-to-grain contact and reduce the bulk stiffness less significantly than do fractures.

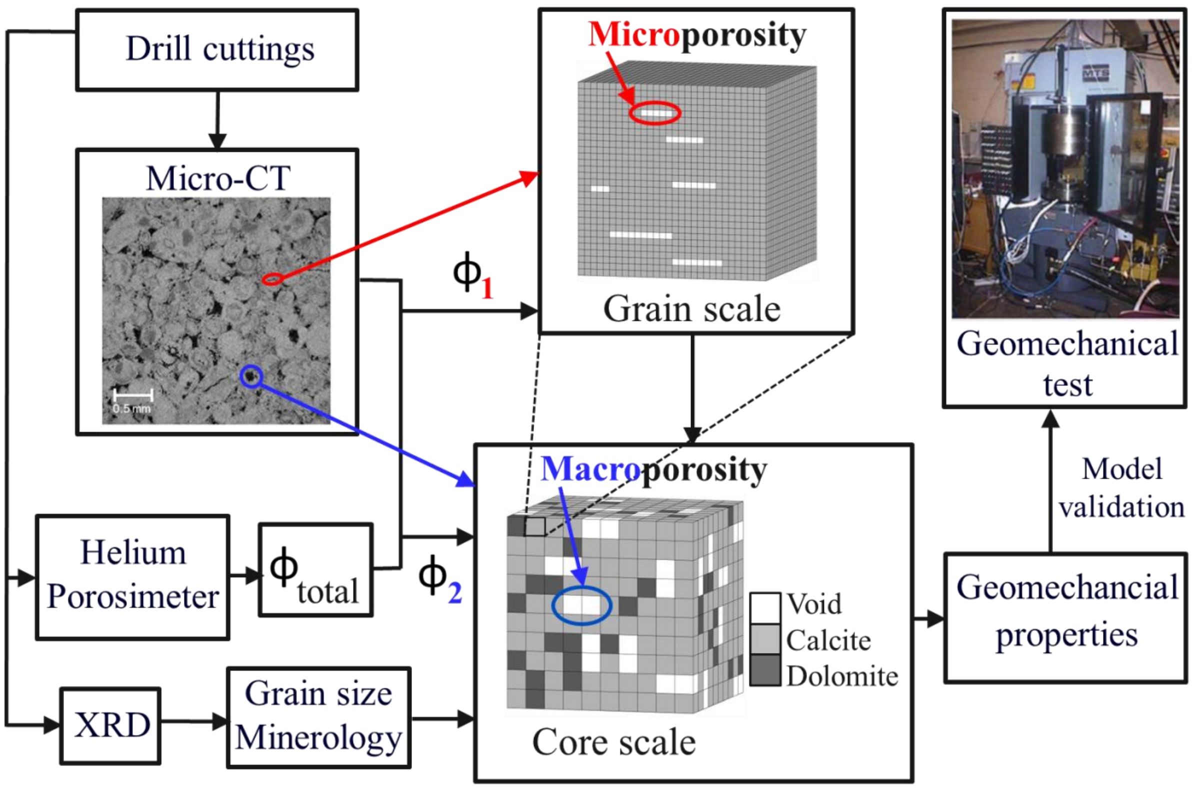

Figure 5.1 – Hierarchical model for the geomechanical characterization of a carbonate formation from drill cuttings. The proposed method follows a hierarchical approach (gain and core scales).

Here, the hierarchical model presented in Chapter 4 is applied to carbonates for geomechanical characterization at the core scale from drill cuttings (Fig. 5.1). The representative element is used to determine the effective elastic properties of a porous grain in the matrix of a carbonate formation (grain-scale model). The effective elastic properties are then used to develop a core-scale model. The developed models at the two scales are numerically solved using the finite element method and then compared with lab measurements of a carbonate formation.

5.2. Small-scale (grain-scale) model

A small-scale model is developed following Eq. 4.1, which enables us to propose a physically representative element for the elastic deformation of a grain with a known mineralogy and size. The representative element is used to build a core-scale model for carbonate, which is discussed later.

The small-scale model accounts for the mineralogy, microporosity, and pore structure of the carbonate. The elastic moduli of solid minerals are available in the literature (Mavco et al., 2009), and those of the voids are set equal to zero in the model. The microporosity can be quantified from the core analysis and the pore structure is represented by the void aspect ratio. The finite element method enables us to compute the effective elastic properties of a porous grain because these effective properties depend on the complex pore structure. The computed effective elastic properties of a porous grain are substituted in Eq. 4.1 to determine the pertinent properties of the representative element.

Because the effective compressive stiffness of the representative element is equal to that of the grain, with a known mineralogy, the displacements of equal compressive forces applied to both are equal. The Poisson's ratio of the representative element is set to be equal to that of the grain. The equality of the Poisson's ratios forces the lateral displacements of the two to be equal for the specified compression, because the Poisson's ratio dictates the ratio of the lateral to the vertical displacements.

5.3. Large-scale (core-scale) model

A large-scale (core-scale) model is developed using representative elements that have been characterized at the small scale. Because grains are deposited randomly, the representative elements with different geomechanical properties are distributed randomly in the large-scale model (the core scale in Fig. 5.1). Different realizations are considered to determine the sensitivity of the results to the spatial distribution for a given ratio of the micro- and macroporosity, and a known porosity.

The total number of the elements in the large-scale model is taken such that each mineral is represented. The number of representative elements for each mineral can be calculated in a manner similar to that shown in Eq. 4.3. The volume fraction of each mineral in the matrix of a formation is determined using XRD. Eq. 4.5 allows us to determine the elastic properties of the large-scale model, which is substituted in Eq. 4.7 to obtain the predicted elastic properties of the carbonate at the core scale. Fig. 4.1 illustrates the boundary conditions of the large-scale model.

5.4. Results

The hierarchical model is applied to the Arab-D carbonate formation simply because its mineralogy, porosity, and core-scale elastic properties are available in the literature. This formation is mainly composed of two minerals (calcite and dolomite). The elastic properties of the calcite and the dolomite minerals are listed in Table 5.1. The volume fractions of the calcite and dolomite in the matrix are equal to 90% and 10%, respectively. The porosity and the pore structure of the formation have also been reported by Ameen et al., (2009).

The hierarchical model is designed to predict the elastic properties of a carbonate at the core scale. Both the small- and the large-scale model are simulated using the finite element method. The numerical results of the large-scale model are used to determine the core-scale elastic moduli of the carbonate based on Eq. 4.7. The sensitivity of the model to the number of elements was tested: The difference between the computed elastic modulus and that of the mineral is less than 1% when the total number of elements is equal to 64 (= 4×4×4). Thus, the total number of elements is taken to be larger than 64 in the performed analyses.

Table 5.1 – Bulk and shear moduli of calcite and dolomite (Mavko et al., 2009). The elastic moduli and the Poisson's ratios are based on the measured values under isotropic conditions.

Mineral	Bulk modulus (GPa)	Shear modulus (GPa)	Elastic modulus (GPa)	Poisson's ratio
Calcite	76.8	32	84.3	0.32
Dolomite	94.9	45	116.6	0.30

In the finite element method, the entire volume is divided into small volumes, which are referred to as elements. The size of each element (grain size) is set equal to 300 μm at the large scale (core scale). This size corresponds to the average grain size reported in the literature for this formation, which is on the order of 100−500 μm (Lucia et al., 2001).

The total porosity is divided into macro- and microporosity. The total porosity is equal to the macro- or microporosity in limiting cases. The microporosity fraction can be measured from high-resolution images for small samples, but quantifying its value for large samples is difficult. Thus, various scenarios are considered for the microporosity fraction that satisfies the following relations:

$$\phi_1 + \phi_2 = \phi_{\text{total}} \text{ and} \tag{5.1a}$$

$$\text{microporosity fraction (\%)} = 100 \times \frac{\phi_1}{\phi_1+\phi_2}, \tag{5.1b}$$

where ϕ_1 is the microporosity, ϕ_2 is the macroporosity, and ϕ_{total} is the total porosity.

The effect of the pore structure on the elastic properties of the carbonate is investigated by considering the void aspect ratios at the grain and the core scales. The aspect ratios of the voids vary from 0.1 to 1 at the small scale (grain scale) and are equal to 0.5 at the large scale (core scale). Considering voids with different aspect ratios is consistent with the data available in the literature (Cantrell and Hagerty 1999). Elements with zero elastic moduli, which mimic the voids, are selected to form a row (or column) to implement the aspect ratio in the model. Fig. 5.1 shows examples of voids whose aspect ratios are equal to 0.2, where five white elements are in a row in the grain-scale model. In the core-scale model, two elements with elastic moduli of zero are next to each other to create the aspect ratio of 0.5.

The small-scale model is analyzed to give a geomechanical characterization of the formation at the grain scale. The elements are divided into the void and the mineral to simulate the porous grain. The number of elements, which are representative of voids, is determined to replicate the microporosity based on Eq. 5.1a. Other elements simulate the minerals with known properties. The void elements form a row, or column, to create the required aspect ratio of 0.05−1 (or 0.1−1). The row or column is randomly distributed in the finite element model, which means the void spaces do not follow any specific spatial distribution function. For a given microporosity, ten different realizations are generated for the random spatial distribution. The realizations yield slightly different elastic moduli, which are averaged to determine the effective modulus. The number of elements in the small-scale model is 27×10^3 (= $30 \times 30 \times 30$) because the simulation results are not sensitive to the number of elements when the number of elements is larger than or equal to 8×10^3 (= $20 \times 20 \times 20$).

The small-scale model is solved by the finite element method to determine the effective elastic properties of the porous grains. The effective elastic properties of the porous grains are different from those of the minerals due to the void presence. A uniaxial and uniform compression is applied to the model, whose boundary conditions are shown in Fig. 4.1. The numerical simulation of the model allows us to determine the force and the displacement, parallel to the compression, and compute the stress by averaging the force over the cross-sectional area perpendicular to the compression. The effective properties are obtained for calcite and dolomite, which are the main minerals in the analyzed carbonate samples.

The effective properties obtained from the small-scale (grain-scale) model are used to determine the geomechanical properties at the large scale (core scale). The elements are divided into the void and the grain in the large-scale model, and the number of elements relevant to the voids is assigned to replicate the macroporosity (Eq. 5.1b). Two void elements are set in a row or column to create the aspect ratio of 0.5 for each void space. The void spaces follow the random spatial distribution in the large-scale model. Other elements simulate the calcite or the dolomite. The number of elements for each mineral is calculated based on its volume fraction in the matrix. The spatial distribution of each mineral element is also random, similar to the void distribution. The large-scale model has 64×10^3 (= $40 \times 40 \times 40$) elements because the results are not sensitive to the number of elements when at least 8×10^3 (= $20\times20\times20$) elements are included. The sensitivity analysis is discussed subsequently.

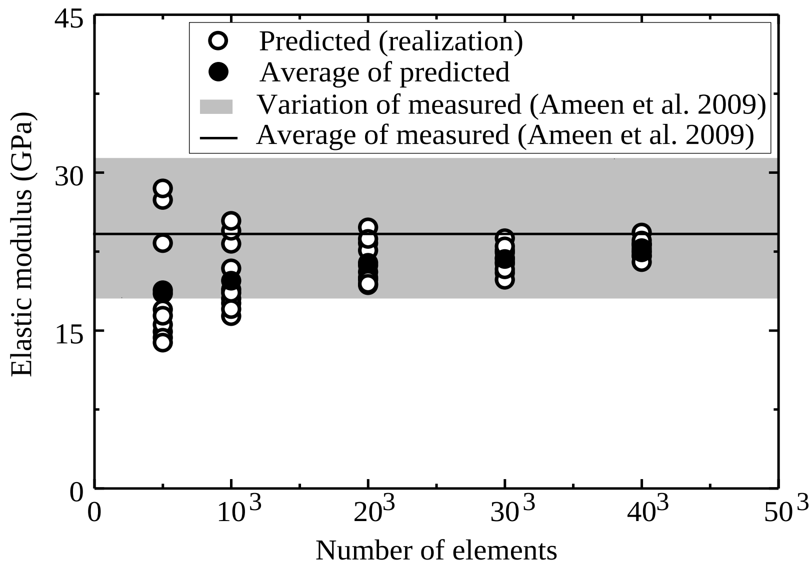

Figure 5.2 – Sensitivity of the proposed model to the number of elements. The average of the predicted moduli is not sensitive to the number of elements when 20^3 (= $20 \times 20 \times 20$) or more elements are incorporated.

The sensitivity analysis indicates that the predicted results are not sensitive to the number of elements when there are 20^3 (= $20 \times 20 \times 20$) or more elements in the large-scale model. For clarification, a specific scenario is considered, where the total porosity is 25% and the microporosity fraction is 50%. Ten random realizations are included for the spatial distribution of the grains and the voids for a given number of elements. Fig. 5.2 shows that the average of the elastic moduli changes less than 4% when the number of elements increases from 20^3 (= $20 \times 20 \times 20$) to 30^3 (= $30 \times 30 \times 30$) and from 20^3 (= $20 \times 20 \times 20$) to 40^3 (= $40 \times 40 \times 40$). These numbers of elements are considered because these numbers allow us to check the change in the predicted results over a wide range. The grey box in Fig. 5.2 shows the lab measurements conducted by Ameen et al., (2009).

The elements with different elastic properties are randomly distributed, which leads to an isotropic model when the model is large. This issue has been tested for all the models, whose results are represented here. As an example, Fig. 5.3 shows the cross-sections of the large-scale model whose total number of elements is 20^3, whose total porosity is 25%, and whose microporosity fraction is 50%. The uniaxial and uniform compressions in the *x*, *y*, and *z* directions have been solved, and the computed elastic moduli turned out to be 21.4 GPa, 21.6 GPa, and 21.1 GPa, respectively. The difference between the maximum and the minimum elastic moduli is less than 2.5%.

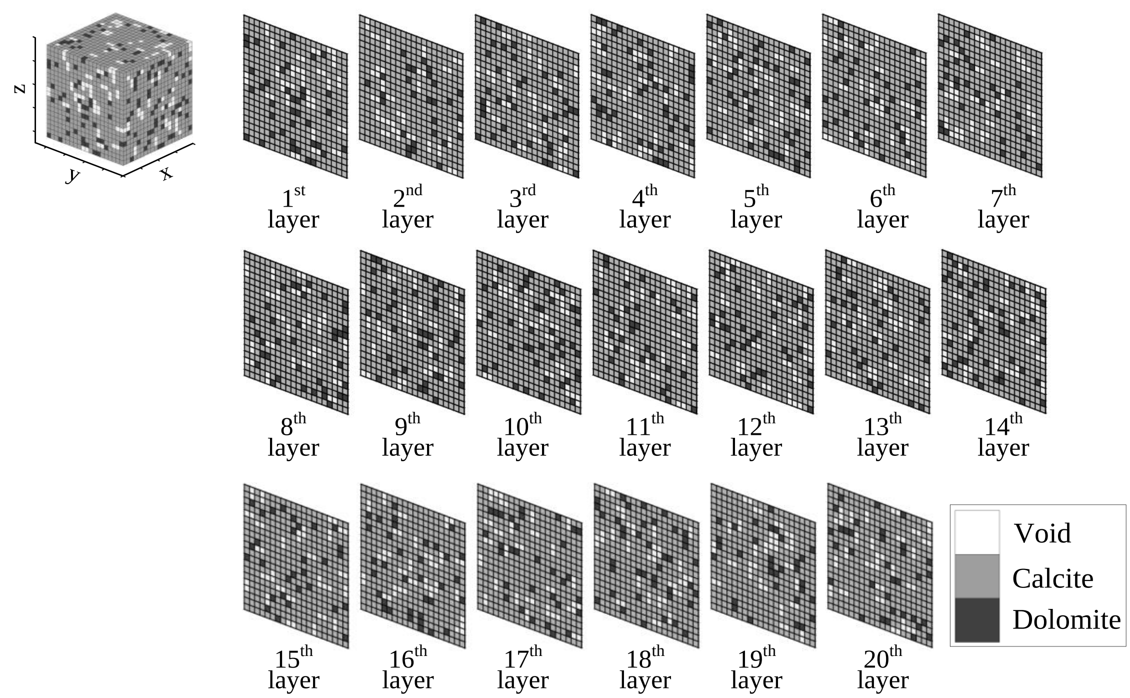

Figure 5.3 – Cross-sectional area of the large-scale model with 20^3 ($20 \times 20 \times 20$) elements. The elements with different elastic properties are randomly distributed, which leads to an isotropic model when the model is large.

The predicted elastic moduli are compared with independent lab measurements conducted on core plugs for two reasons. First, the size of the large-scale model, which is 1.2 cm (= 40 × 300 μm), is close to that of the core plug, which is close to 1 in (= 2.54 cm). Second, the large-scale model excludes fractures, which is a realistic assumption for the intact core plugs, as the analyzed core plugs were free of visible fractures and defects. The large-scale model is a cube, while the core plug is a cylinder. The elastic modulus of a defect-free medium is relatively fixed at low loading rates. Other issues relevant to the scale are addressed in detail in the Discussion section below.

The importance of the pore structure for the elastic modulus of a carbonate needs further discussion. The importance of the pore structure is assessed by analyzing the effect of the microporosity fraction on the predicted results. The microporosity fraction ($\frac{\phi_1}{\phi_1+\phi_2}$) is different from the microporosity (ϕ_1) and the total porosity (ϕ_1+ϕ_2). Fig. 5.4 shows the average of the simulation results based on the hierarchical model. The grey box shows the upper and lower limits of the measurements of 400 core plugs (Ameen et al., 2009). The hierarchical model indicates that, for a given porosity, the elastic modulus decreases with an increase in the microporosity fraction of the pore space. The observed trend is consistent with other measurements relevant to the impact of the microporosity fraction (Eberli et al., 2003; Sayers 2008; Weger et al., 2009; Xu and Payne 2009). The hierarchical model provides a systematic approach to quantifying the pore structure's effect and can be applied to drill cutting. The predicted results agree with measured values for the formation analyzed.

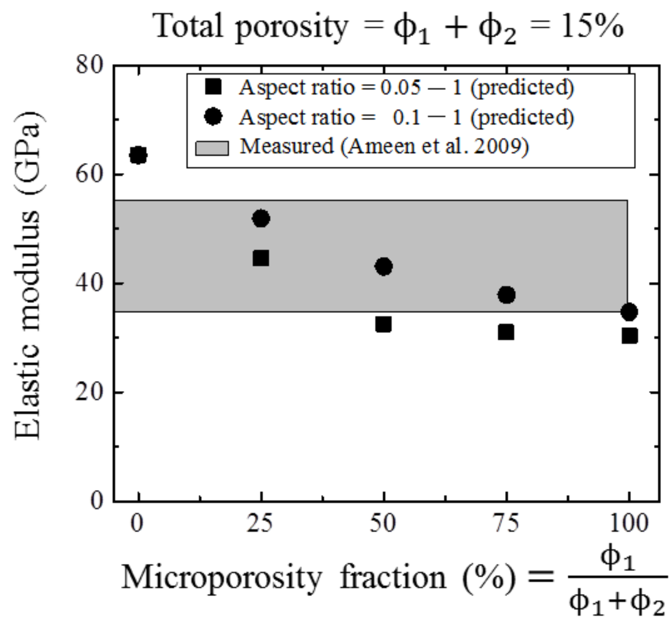

a. Total porosity = 15 %

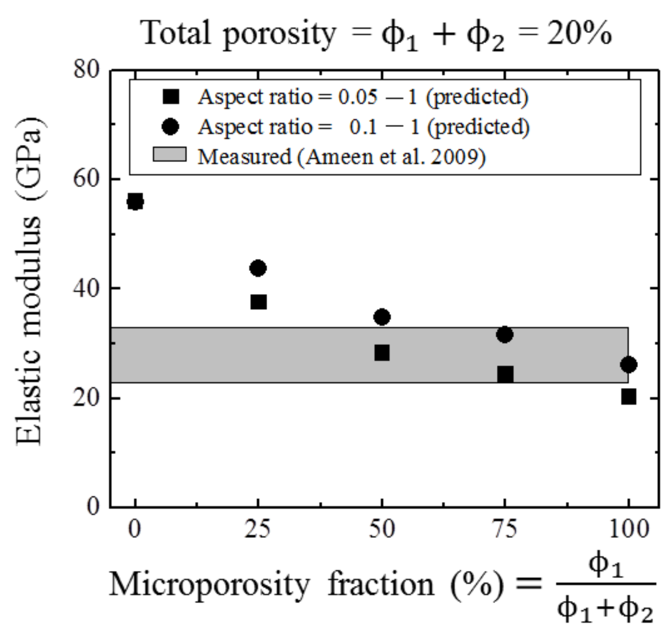

b. Total porosity = 20 %

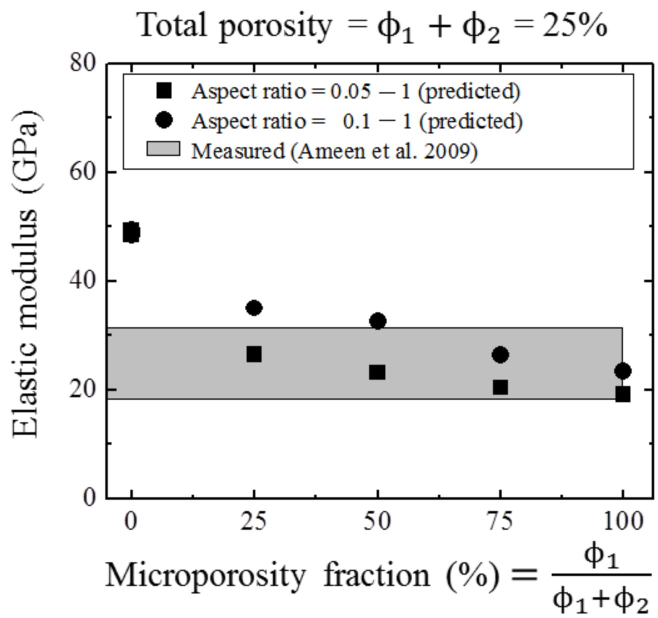

c. Total porosity = 25 %

Figure 5.4 – Predicted elastic moduli, based on the hierarchical model, decrease with an increase in the microporosity fraction of the pore space, which is consistent with lab observations. Ameen et al., (2009) conducted the measurements.

Next, the effect of the total porosity on the elastic modulus is investigated. Fig. 5.5 shows that the elastic modulus decreases with increasing porosity only when the microporosity fraction does not change significantly. In other words, both the total porosity and the microporosity must be considered to be governing parameters. The elastic modulus need not correlate with the total porosity or the microporosity alone. The lack of correlation is consistent with the data available in the literature (Ameen et al., 2009) and further highlights the importance of the pore structure for understanding the geomechanical behavior of the formation. The effect of the pore structure is expressed using different pore models for the microporosity and macroporosity in the hierarchical model.

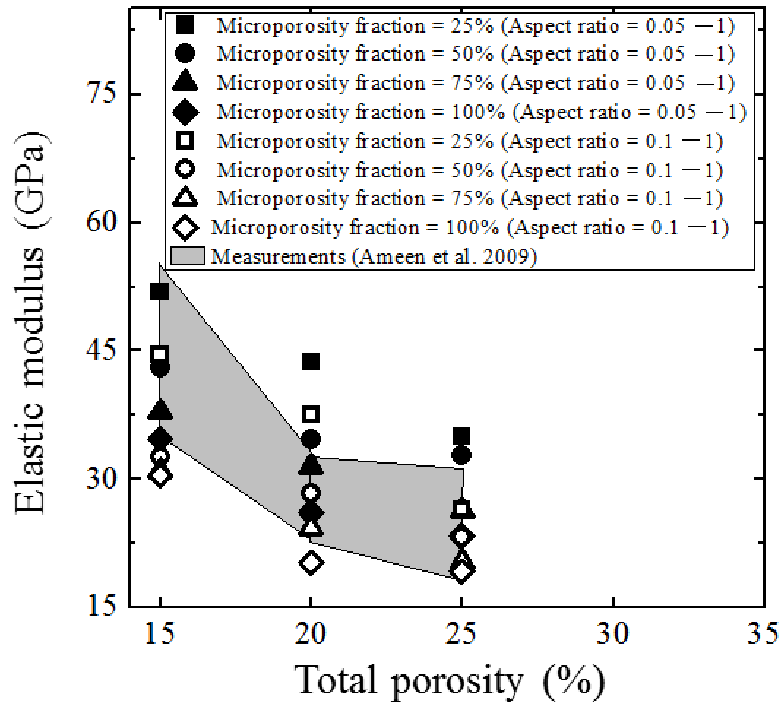

Figure 5.5 – The elastic moduli of a carbonate decreases with an increase in the total porosity only when the microporosity fraction is fixed.

At this point, the applicability of the proposed model needs to be discussed. The error associated with the predicted elastic moduli of a carbonate is determined to evaluate the accuracy of the developed hierarchical model. The error associated with the predicted elastic modulus is computed as follows:

$$Error\ (\%) = \left|\frac{E_{Model}^{Ave} - E_{Lab}^{Max}}{E_{Lab}^{Max}}\right| \times 100 \quad \text{If } E_{Lab}^{Max} < E_{Model}^{Ave}, \tag{5.2a}$$

$$Error\ (\%) = 0 \quad \text{If } E_{Lab}^{Min} \leq E_{Model}^{Ave} \leq E_{Lab}^{Max}, \text{ and} \tag{5.2b}$$

$$Error\ (\%) = \left|\frac{E_{Model}^{Ave} - E_{Lab}^{Min}}{E_{Lab}^{Min}}\right| \times 100 \quad \text{If } E_{Model}^{Ave} < E_{Lab}^{Min}. \tag{5.2c}$$

where $Error$ is relevant to the accuracy of the developed model, E_{Model}^{Ave} is the average of the predicted elastic moduli using drill cuttings, E_{Lab}^{Max} is the maximum of the measured elastic moduli of a core plug, and E_{Lab}^{Min} is the minimum of the measured elastic moduli of a core plug.

Fig. 5.6 quantifies the accuracy of the developed hierarchical model for characterizing the geomechanical properties of a carbonate formation based on drill cuttings. The results are provided for a given total porosity by averaging different microporosity fractions, which are listed in Table 5.2. The error remains smaller than 5% for the carbonate formation analyzed, which is a good approximation. The accuracy of the developed model becomes more apparent if the predicted elastic moduli are compared with those of pure calcite (76.8 GPa) and dolomite (94.9 GPa), which are much larger than the lab measurements shown in Fig. 5.6. More importantly, the developed hierarchical model can be used for drill cuttings. This is a significant advantage compared to core-scale measurements, which are time consuming and expensive.

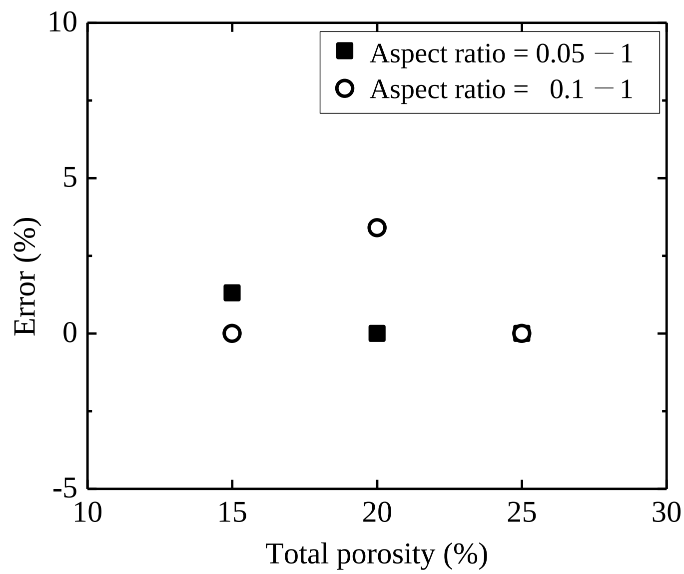

Figure 5.6 – Error associated with the predicted elastic modulus of a carbonate formation based on the proposed model from drill cuttings. The results are averaged for different fractions of the microporosity, which are listed in Table 5.2.

Now, the hierarchical model is applied to predict the variation of the elastic modulus of a carbonate formation with depth. The predicted results, which are presented in a pseudo-log format, are compared against lab measurements available in the literature (Ameen et al., 2009). The hierarchical model predicts the static modulus, as opposed to the dynamic modulus that is often estimated from acoustic velocity logs. The model input parameters are the total porosity, the pore structure, and the mineralogy. The standard core analysis often quantifies the total porosity but excludes the other two. Thus, the minimum and maximum moduli for a given total porosity are predicted by changing the microporosity fraction and the mineralogy. The void aspect ratio varies between 0.05 and 1 in microporosity and is 0.5 in macroporosity.

Table 5.2 – Error associated with the predicted elastic moduli based on the proposed hierarchical model. The average of the results for a given total porosity is shown in Fig. 5.6.

Aspect ratio	Microporosity fraction (%)	Total porosity (%)		
		15	20	25
0.05 — 1	100	13.2	12.5	0
	75	11.8	0	0
	50	7.3	0	0
	25	0	14.0	0
0.1 — 1	100	1.1	0	0
	75	0	0	0
	50	0	5.5	4.4
	25	0	33.0	11.9

Fig. 5.7 shows the pseudo-log of the elastic modulus. The minimum and maximum moduli are predicted by changing the pore structure and the mineralogy for a given total porosity. There were 28 lab measurements, of which 23 remained within the predicted bounds. The agreement between the lab measurements and the model corroborates the proposed model. Fig. 5.7 also indicates that the model can provide a

convenient tool for predicting the range of the elastic modulus. The importance of the predicted range is greater when core plugs are unavailable because the model can be applied to small pieces of rock samples (drill cuttings).

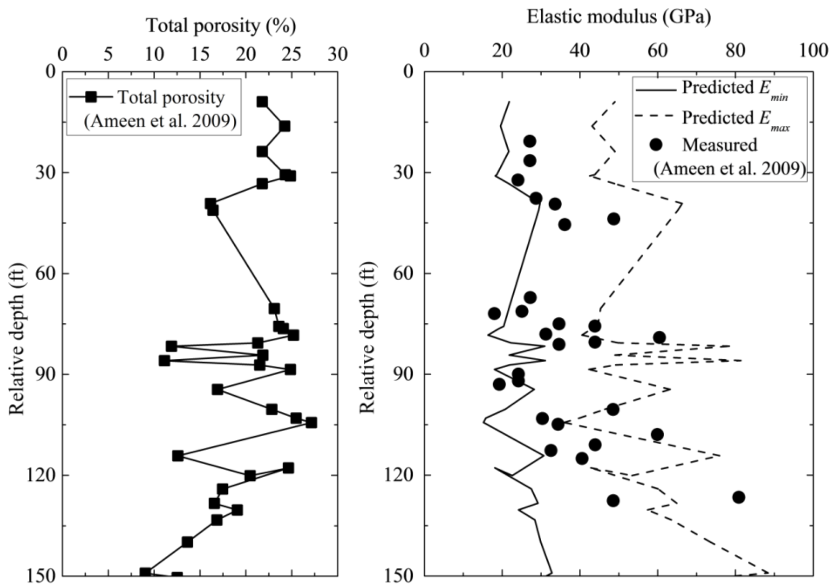

Figure 5.7 – Predicted pseudo-log of the static elastic modulus based on the hierarchical model and independent lab measurements (Ameen et al. 2009).

5.5. Discussion

In this section, the effects of different parameters on the predicted results are discussed. Ameen et al., (2009) indicated that, for a given total porosity, the measured elastic modulus varies significantly because the mineralogy, the rock texture, and the rock pore structure change, which is consistent with the proposed model.

5.5.1. Rock mineralogy

The lab measurements, conducted by Ameen et al., (2009), indicate that the elastic modulus of a dolostone is higher than that of a limestone at a given porosity. The dolostone is mainly composed of dolomite, while the limestone is composed of calcite. The proposed model shows the same trend, as the elastic modulus is higher when the forming mineral is 100% dolomite (E_{max} in Fig. 5.7) than when the forming mineral is 100% calcite (E_{min} in Fig. 5.7). The effect of the mineralogy alone on the elastic properties is difficult to quantify because the calcite and the dolomite usually have different pore structures in a carbonate sample.

To help us build a realistic model at the core scale, the drill cuttings must include the representative mineralogy of a core plug. The grain size in carbonate formations can be as large as 0.5 mm (Lucia et al., 2001). Thus, cuttings that are smaller than 1 mm (Lenormand and Fonta 2007) should not be used to determine the mineralogy.

5.5.2. Rock texture

The rock texture refers to the size, shape, and sorting of grains in the matrix (Lucia 2007). Ameen et al., (2009) studied the effect of the grain size on the elastic properties of a carbonate sample in the Arab-D formation, based on the Dunham classification (Dunham 1962). Ameen et al., (2009) observed that the crystalline rocks showed the highest static elastic moduli among the various rock textures for a given total porosity. Ameen et al., (2009) also reported that the impact of the rock texture on the elastic modulus was less significant than those of the total porosity and the pore structure.

The Dunham classification is not adopted in the proposed model. The hierarchical model implements the grain size and the shape, and the results are promising when the grain size does not change significantly. The accuracy of the proposed model deteriorates when the sample is poorly sorted and the grain size varies over several orders of magnitude. This issue may be resolved by combining clustered small grains, but such analyses are beyond the scope of the present study.

5.5.3. Rock pore type (pore structure)

For different fractions of the macroporosity, Fig. 5.4 shows that the elastic modulus varies from 19.2 GPa to 63.5 GPa and from 23.3GPa to 63.5 GPa when the total porosity is equal to 15% and 25%, respectively. The predicted results reveal the importance of the pore structure for the geomechanical characterization of the carbonate formation, which is consistent with the data available in the literature (Ameen et al., 2009).

To help us build a representative model at the core scale, the drill cuttings must include the representative pore type (pore structure) of a core plug. Micro- and macro-voids exist in drill cuttings because these voids are smaller than the cutting size. Cuttings with fractures should not be used because the main purpose of the proposed model is to capture the elastic properties of an intact core plug without visible fractures. Cuttings should also be free of vugs (Sakhaee-Pour and Tran 2017), whose effects are not included in the proposed model.

5.5.4. Porosity

Ameen et al., (2009) measured the effect of the total porosity on the elastic modulus of the carbonate sample from the Arab-D formation. Their measurements showed that the elastic modulus varied from 55.2 GPa to 18.1 GPa when the total porosity increased from 15% to 25%. The proposed model predicts that the elastic modulus will decrease from 63.5 GPa to 19.2 GPa for the same change in the total porosity (Fig. 5.4). For a given total porosity, thus, the predicted results are slightly higher than the measured values.

To help us build a representative model at the core scale, the drill cuttings must include the representative porosity. Moreover, the standard helium expansion measures the porosity accurately only when the sample size is larger than or equal to 2.5 mm (Lenormand and Fonta 2007). Thus, very small drill cuttings are not appropriate for porosity determination in the proposed model.

Finally, for completeness, the limitations of the proposed model are discussed. First, the proposed model does not account for the presence of fluid or pore pressure. Thus, the predicted results are more realistic for drained conditions (Wang 2017). Second, the proposed model does not incorporate fractures; hence, the predicted results are more representative of intact cores without visible fractures. Third, the proposed model cannot predict the rock strength, because plasticity, or local failure, is not included.

5.6. Conclusions

The main objective of this chapter was to develop a hierarchical model for characterizing the quasi-static elastic modulus of a carbonate formation at the core scale from drill cuttings. In the hierarchical model, the effective elastic properties of the formation at the small scale (grain scale) are determined based on the grain size and the elastic properties of the forming minerals. The effective elastic properties of the grains are then implemented in a large-scale model for predicting the elastic properties at the core scale. The hierarchical model was implemented for the Arab-D carbonate formation in the Middle East.

The hierarchical model shows that the pore structure plays an important role in the elastic moduli of the Arab-D carbonate formation, especially when the porosity increases. The pore structure effect was implemented by accounting for the aspect ratio of the void at the two scales. The simulation results also show that the geomechanical properties need not correlate with the total porosity, which requires a hierarchical model to be captured. Independent lab measurements corroborate the results. For the carbonate formation analyzed, the hierarchical model predicts the elastic moduli with a less than 5% error.

Chapter 6. A Hierarchical Model for Predicting the Anisotropic Elastic Properties of Shales at the Core Scale

This chapter presents a revised hierarchical model to capture the anisotropic elastic properties of shales at the core scale. For this objective, the governing parameters of the anisotropic elasticity of shales are elaborated, and then incorporated into the revised hierarchical model. The model is implemented for Lower Bakken, Barnett, and Haynesville shales for validation. Finally, a sensitivity analysis is conducted, based on one Lower Bakken sample, to systematically determine the importance of each governing parameter on the anisotropic elastic properties of shales.

6.1. Governing parameters of the elastic anisotropy of shales at the core scale

The mechanical properties of a shale at the core scale become anisotropic due to the microfabric characteristics of the solid phase in the matrix (Sayers 2013) and the void structure (Hornby et al., 1994). Table 6.1 summarizes the parameters whose effects on the elastic properties of shales are discussed below.

6.1.1. Solid phase

The intrinsic anisotropic elastic properties of clay platelets have been determined using a theoretical method (Sayers and den Boer 2016), acoustic velocity analysis (Katahara 1996), and nanoindentation measurement (Ortega et al., 2007). Table 6.2 shows that a large variation exists in the reported values. The large variation is due to the presence of different clay mineral types and the adopted analysis method. The anisotropic elastic moduli of clays, reported in Sayers (2005), are used in the present study because these values are representative of in-situ solid clays (Ortega et al., 2007).

Clay platelet orientation affects the anisotropic elastic properties of shales at the core scale (Hornby et al., 1994). Clay platelets are generally aligned parallel to the bedding, but they are locally disordered due to the presence of the silt grains (Sayers and den Boer 2016). It is difficult to quantify the orientation due to the small particle size (~ nm). Hornby et al., (1994) reported that the platelet orientation in a shale ranges from 0^o to 90^o with respect to the bedding. Their measurement suggests that the mode and the average of the platelet orientation are 6^o and 20^o degrees, respectively. The average orientation is adopted to model the Lower Bakken, Barnett, and Haynesville shales in the present study.

The microfabric structures of the kerogen and clay aggregates contribute to the elastic anisotropy of shales. Kerogen and clay aggregates form patch, lenticular, and layer structures (Loucks et al., 2009; Chalmers et al., 2012). It is difficult to characterize the structures because their geometric sizes are non-uniform in the matrix. The lenticular structure with various geometries is used in this study to make a realistic estimate of the microfabric structures of the kerogen and clay aggregates.

Shales are strongly heterogeneous and their mineral composition can vary significantly. The mineral composition, which can be determined by X-ray diffraction (XRD) (Sone and Zoback 2013), has an impact on their elastic properties. In the present study, the model is implemented based on the mineral composition shown in Table 6.3 for three shales (Simpson et al., 2015; Sone 2012; Sone 2018).

Table 6.1 – Governing parameters of the elastic anisotropy of shales

Void or matrix	Physical factors	Mathematically parameters	Values/Ranges	Methods	References	Model inputs	Grain- or core-scale model
Matrix	Elastic anisotropy of clays	Anisotropic elastic moduli (E^{clay})	Known (Table 6.2)	Measurements or inversion analysis	Table 6.2	Anisotropic E^{clay} (Table 6.2)	Grain- and core-scale
	Clay platelet orientation	Orientation angle to the bedding	0 – 90°	Imaging or modeling	Hornby et al., (1994); Chalmers et al., (2012)	20°	Grain-scale
	Structure of kerogen	Lenticular with geometric size	Unknown	Imaging but difficult to characterize	Vernik and Nur (1992); Sone and Zoback (2013)	$1 - m$ [d]	Core-scale
	Structure of clay aggregates	Lenticular with geometric size	Unknown	Imaging but difficult to characterize	Vernik and Nur (1992); Sone and Zoback (2013)	$1 - m$ [d]	Core-scale
	Mineral composition	Mineral volume fractions	Known	XRD measurements	Simpson et al., (2015) Sone (2012)	Table 6.3	Core-scale
Void	Macroporosity	ϕ_{macro} fraction[a]	0 – 100%	Difficult to measure	–	0	Core-scale
	Topology of macropores	Aspect ratio (AR_m)[c]	0.50 – 1.00	Imaging	Vasin et al., (2013)	–	Core-scale
	Microporosity	ϕ_{micro} fraction[a]	0 – 100%	Difficult to measure	–	100%	Grain-scale
	Kerogen porosity	$\phi_{kerogen}$ fraction[b]	0 – 100%	Difficult to measure	–	50%	Grain-scale
	Clay aggregate porosity	ϕ_{clay} fraction[b]	0 – 100%	Difficult to measure	–	50%	Grain-scale
	Topology of pores in kerogen	Aspect ratio (AR_k)[c]	0.21 – 0.77	Imaging or modeling	Loucks et al., (2009); Klaver et al., (2012)	0.49	Grain-scale
	Topology of pores in clay aggregates	Aspect ratio (AR_c)[c]	0.05 – 1.00	Imaging or modeling	Hornby et al., (1994); Keller (2016)	0.05	Grain-scale

a. ϕ_{macro} fraction $= \frac{\phi_{macro}}{\phi_{total}}$, ϕ_{micro} fraction $= \frac{\phi_{micro}}{\phi_{total}}$, where $\phi_{total} = \phi_{macro} + \phi_{micro}$;

b. $\phi_{kerogen}$ fraction $= \frac{\phi_{kerogen}}{\phi_{micro}}$, ϕ_{clay} fraction $= \frac{\phi_{clay}}{\phi_{micro}}$, where $\phi_{micro} = \phi_{kerogen} + \phi_{clay}$;

c. Aspect ratio is defined as the ratio of the short axis to the long axis for a spheroidal void space;

d. 'm' is the element number in one edge of the core-scale model.

Table 6.2 – Anisotropic elastic properties of clay minerals

Clays	c_{11} (GPa)	c_{33} (GPa)	c_{44} (GPa)	c_{13} (GPa)	c_{12} (GPa)	References	E_1 (GPa)[a]	E_3 (GPa)[a]	Selected E_1 (GPa)	Selected E_3 (GPa)
Illite	179.90	55.00	11.72	14.50	39.84	Katahara 1996	168.71	53.09	32.89	13.79
	127.40	54.70	14.40	28.40	48.00	Bayuk et al., 2007	102.84	45.50		
	81.40	53.10	22.70	18.40	21.40	Vasin et al., 2013	72.02	46.51		
	40.00	16.80	2.70	9.00	13.80	Sayers 2005	32.89	13.79		
	44.90	24.20	3.70	18.10	21.70	Ortega et al., 2007	29.24	14.36		
Chlorite	181.76	106.77	11.42	20.34	56.77	Katahara 1996	162.16	103.30	32.89	13.79
	40.00	16.80	2.70	9.00	13.80	Sayers 2005	32.89	13.79		
	44.90	24.20	3.70	18.10	21.70	Ortega et al., 2007	29.24	14.36		
Kaolinite	171.52	52.63	14.76	27.11	38.88	Katahara 1996	153.61	45.64	32.89	13.79
	122.20	87.30	28.70	34.30	43.40	Vasin et al., 2013	100.49	73.09		
	40.00	16.80	2.70	9.00	13.80	Sayers 2005	32.89	13.79		
	44.90	24.20	3.70	18.10	21.70	Ortega et al., 2007	29.24	14.36		

a. $E_1 = (c_{11}^2 c_{33} + 2c_{13}^2 c_{12} - 2c_{11}c_{13}^2 - c_{33}c_{12}^2)/(c_{11}c_{33} - c_{13}^2)$, $E_3 = (c_{11}^2 c_{33} + 2c_{13}^2 c_{12} - 2c_{11}c_{13}^2 - c_{33}c_{12}^2)/(c_{11}^2 - c_{12}^2)$ (Bower 2009).

Table 6.3 – Elastic properties of the solid minerals in shales. Mineral composition and measured core-scale elastic properties are also given for Lower Bakken (LB1−LB3), Barnett (B1−B4), and Haynesville (H1−H6) shales.

		Mineral properties			Mineral composition (wt%)												
		Density ρ_i (g/cm^3)	Young's modulus *Em* (GPa) [a]	Poisson's ratio [a]	LB1[c]	LB2[c]	LB3[c]	B1[d]	B2[d]	B3[d]	B4[d]	H1[d]	H2[d]	H3[d]	H4[d]	H5[d]	H6[d]
Kerogen		1.30 [a]	6.2	0.14	25.5	27.5	24.4	11.4	11.4	9.1	8.5	7.6	7.7	7.5	7.9	7.9	7.9
Clays	Kaolinite	2.44 [b]	Table 6.2		0	0	0	0	0	0	1.0	0.8	0	0	0.4	0.4	0.4
	Illite	2.75 [b]			19.1	13.2	15.0	36.5	36.1	38.8	33.3	31.0	34.6	32.1	31.0	31.0	31.0
	Chlorite	2.68 [b]			7.2	12.1	0	0	0	0	2.4	4.8	4.4	4.3	4.2	4.2	4.2
Feldspar (orthoclase)		2.62 [a]	39.7	0.32	5.1	5.3	4.5	0	0	0	4.0	5.1	1.2	6.1	2.4	2.4	2.4
Plagioclase (albite)		2.63 [a]	69.0	0.35	2.1	2.1	2.1	4.4	4.1	4.5	7.8	6.2	5.9	5.2	6.2	6.2	6.2
Calcite		2.71 [a]	84.3	0.32	2.6	3.9	1.2	0	0	0	1.0	19.2	19.0	18.7	21.3	21.3	21.3
Quartz		2.65 [a]	94.5	0.08	29.6	26.1	44.1	44.4	47.4	46.7	35.7	22.5	22.8	22.5	23.4	23.4	23.4
Ankerite		3.05 [a]	98.9	0.32	0	0	0	0	0	0	0	0.2	1.3	0	0	0	0
Dolomite		2.87 [a]	116.6	0.30	3.6	3.5	4.3	0.4	0	0	1.8	0.9	0	1.3	0.7	0.7	0.7
Apatite		3.21 [a]	146.7	0.21	0	0	0	2.0	0	0	1.6	0	0.8	1.0	0	0	0
Pyrite		4.81 [a]	260.6	0.19	5.2	6.3	4.4	1.0	0.9	0.9	3.1	1.3	1.1	1.3	1.3	1.3	1.3
Total porosity ϕ_{total} (%)		–	–	–	9.1	6.6	8.1	4.2	6.2	5.9	9.1	5.8	6.1	5.7	5.6	5.6	5.6
Measured E_1 (GPa)		–	–	–	17.6	22.7	24.1	–	–	42.9	46.9	–	–	–	–	43.0	45.9
Measured E_3 (GPa)		–	–	–	12.3	13.4	17.3	24.9	24.6	–	–	18.2	17.7	16.9	15.1	–	–

a. Mavko et al., (2009); b. Wang et al., (2001); c. Simpson et al., (2015); d. Sone (2012) and Sone (2018).

6.1.2. Void system

The void system is crucial for developing a realistic model of a shale. The voids are divided into macro- and micro-pores, which have different characteristic sizes and topologies (Hornby et al., 1994; Loucks et al., 2009). It is difficult to determine the volume fraction of each category at the core scale. High-resolution images allow us to determine the corresponding fraction for a small volume, but it is not possible to scale such determinations to a core scale (Sakhaee-Pour and Li 2016). Eqs. 6.1 to 6.3 enable us to consider a full range of the micro- and macroporosity without any restrictions. For instance, the microporosity fraction can vary from 0 to 100%. The micro- and macroporosity fractions are tuned in the hierarchical model to characterize the representative void system for a particular shale formation.

$$\phi_{macro\_fraction} = \frac{\phi_{macro}}{\phi_{total}}, \tag{6.1}$$

$$\phi_{micro\_fraction} = \frac{\phi_{micro}}{\phi_{total}}, \text{ and} \tag{6.2}$$

$$\phi_{total} = \phi_{macro} + \phi_{micro}, \tag{6.3}$$

where ϕ_{total} is the total porosity, ϕ_{macro} is the macroporosity, ϕ_{micro} is the microporosity, $\phi_{macro\_fractoin}$ is the macroporosity fraction, and $\phi_{micro\_fractoin}$ is the microporosity fraction.

The microporosity resides inside the kerogen and clay aggregates, but the pores in each are different in topology (Sayers 2013). The pores in the kerogen are mostly ellipsoidal with greater aspect ratios (Loucks et al., 2009; Klaver et al., 2012). The pores in the clay aggregates are elongated because they are confined by the sheet-like geometry of the clay platelet. It is also difficult to determine the porosity fraction associated with each for a bulk volume, based on the high-resolution images; thus, they are calculated using Eqs 6.4 to 6.6. A full range of the local porosities in kerogen and clays is considered when the hierarchical model is tuned for a shale formation.

$$\phi_{kerogen\text{-}fraction} = \frac{\phi_{kerogen}}{\phi_{micro}}, \tag{6.4}$$

$$\phi_{clay\text{-}fraction} = \frac{\phi_{clay}}{\phi_{micro}}, \text{ and} \tag{6.5}$$

$$\phi_{micro} = \phi_{kerogen} + \phi_{clay}, \tag{6.6}$$

where $\phi_{kerogen}$ is the microporosity inside the kerogen, $\phi_{kerogen\_fractoin}$ is the fraction of the microporosity in kerogen, ϕ_{micro} is the microporosity, ϕ_{clay} is the microporosity associated with the clay aggregates, and $\phi_{clay\_fractoin}$ is the fraction of the microporosity in clays.

6.1.3. Uncertainties in the governing parameters

There are uncertainties in the governing parameters and it is not possible to determine all of them from lab measurements. Thus, a range is considered for each parameter that does not have a unique value. The uncertainty of each parameter has an effect on the anisotropic elastic moduli that are measured for a specific core sample. Considering a physically realistic range also helps us determine the effect of each parameter on the predicted results from the sensitivity analysis.

6.2. A revised hierarchical model for the anisotropic elasticity of shales

The main objective of this chapter is to predict the static anisotropic elastic properties of a shale at the core scale from its constituents and structures based on a revised hierarchical model. Fig. 6.1 shows the workflow of the revised model. The small-scale measurements, such as those using X-ray diffraction (XRD), a helium porosimeter, and a scanning electron microscope (SEM), can be conducted on small samples to characterize the governing parameters (Table 6.1). The input parameters are implemented in the model, the results of which are tested with lab measurements at the core scale.

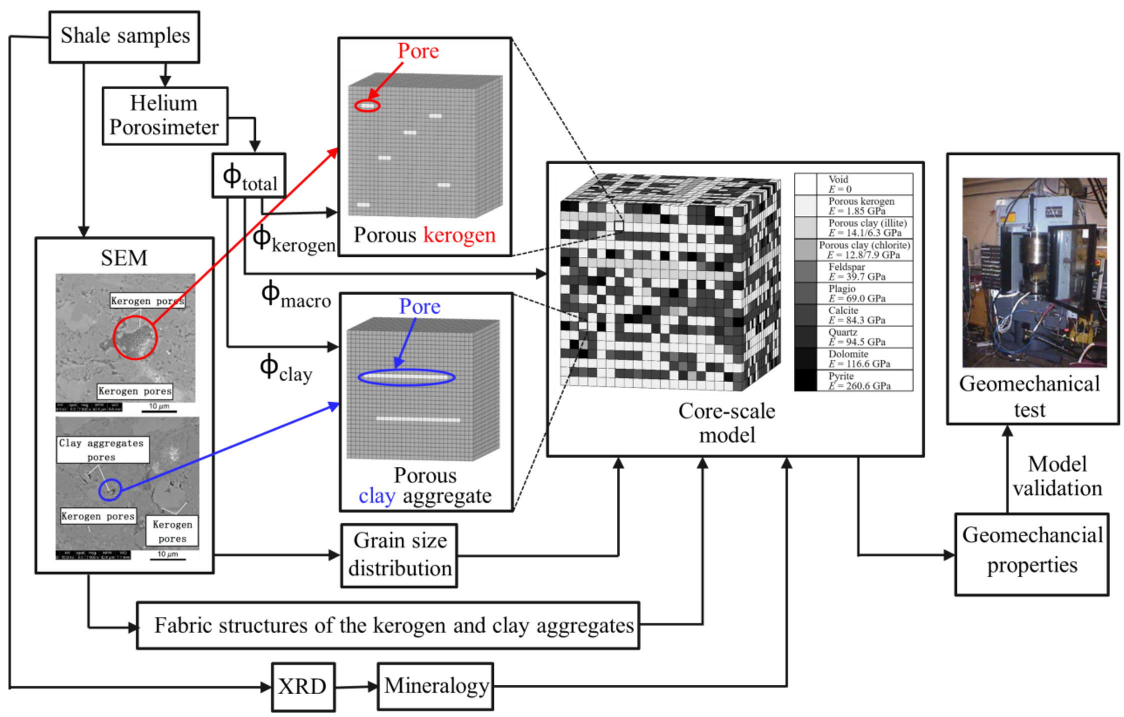

Figure 6.1 – The hierarchical model for predicting the anisotropic elasticity of a shale at the core scale from its constituents and structures. It is revised from Fig. 1.2 by considering the microfabrics of the solid phase and the void structure.

6.2.1. Small-scale (grain-scale) model

Chapter 4 presented the procedures to develop the physically representative element for the elastic deformation of a grain of known mineralogy. The same procedures are applicable here to derive the pertinent representative elements for the porous kerogen and the other solid minerals in shales. However, the small-scale model for the porous clay aggregates must be updated because the anisotropic elastic properties of clays and the clay platelet orientation need be accounted for in the revised model.

The following procedures are used to develop the small-scale model for the porous clay aggregates. First, the local porosity in clay aggregates is obtained according to Eqs. 6.5 and 6.6. This local porosity determines the amount of pore space in the small-scale model, given the geometry and topology of the pores in clays (see section 4.1.1). Then, the void space is considered to align in two distinct directions: perpendicular to and parallel to the axis of symmetry. This consideration of the void space allows us to mathematically mimic the average orientation of the sheet-like voids (or clay platelets). For instance, the average clay platelet orientation is 18^{o} from the horizontal direction if one vertical and four horizontal sheet-like voids are introduced in the model. Finally, the elements relevant to the clay platelets have the anisotropic elastic properties listed in Table 6.2, whereas for the remainder, the elastic moduli are zero.

The finite element method is used to determine the effective anisotropic elastic properties of porous clay aggregates. One end of the model is roller constrained and the other end is subject to uniform compression (Fig. 4.1). Because clays show anisotropic elasticity, uniform compressions are applied in two orthogonal directions to compute the effective anisotropic moduli at the grain scale. Finally, Eq. 4.1 is used to determine the elastic properties of the representative elements for clay aggregates.

6.2.2. Large-scale (core-scale) model

The core-scale model is developed using the representative elements. Eqs. 4.3 and 4.4 are used to determine the number of elements for each mineral based on the pertinent volume fraction. Eq. 4.5c helps us to compute the elastic modulus of the core-scale model whose boundary conditions can be found in Fig. 4.1. Similarly, the elastic modulus of the core-scale model is converted to that of the rock using Eqs. 4.6 and 4.7.

In reality, kerogen and clay aggregates form complex structures with various characteristic sizes parallel to the bedding (Sone and Zoback 2013; Milliken et al., 2012). These microfabric structures are considered in the core-scale model due to their significant effect on the anisotropic elasticity of shales. For this reason, the core-scale model includes a number of lenticulars of random sizes that are smaller than the model size. The lenticular structures are randomly distributed in the planes perpendicular to the axis of symmetry of the shale. Other minerals do not form any spatial structure and are also randomly distributed in the core-scale model. Different realizations are generated to account for the effect of the random spatial distribution on the results. Fig. 6.2 shows one example of a core-scale model that incorporates the microfabric structures of the shale matrix. The random distribution of the lenticulars enables us to generate microstructures with non-uniform geometries and sizes for the kerogen and clays. This is in agreement with the SEM observations of various shale formations (Sone and Zoback 2013). Other shapes may also be applied to form the microfabric structures of the shale matrix (Vasin et al., 2013), but this is beyond the scope of the present study.

Finite element analysis allows us to calculate the anisotropic elastic moduli of the core-scale model. The loading and boundary conditions are similar to that shown in Fig. 4.1. The core-scale model is solved in an unconfined compressive test, and the predicted results are compared with the independent lab measurements of core plugs under the triaxial compression condition. The different boundary conditions between the simulations and the lab measurements have negligible effects on the model validation analysis for the following reason: the analyzed shales are relevant to consolidated formations whose elastic properties show negligible dependency on the confining pressures (Sone and Zoback 2013).

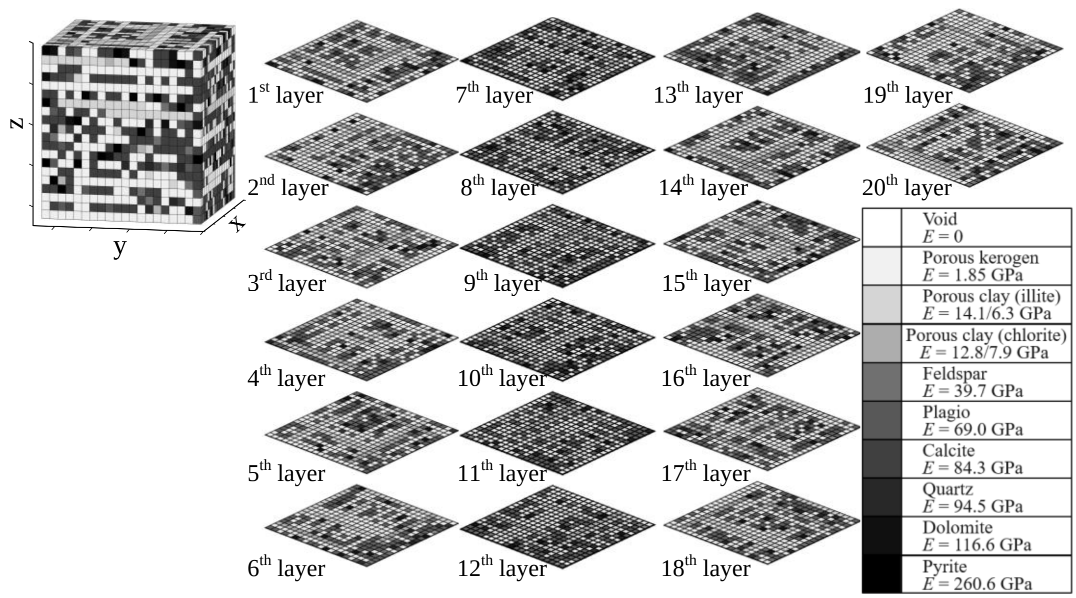

Figure 6.2 – Cross sections of a core-scale model that includes the microfabric structure of the kerogen and clays for the LB1 sample. The elastic properties of the porous kerogen and clays are characterized using the grain-scale model.

The core-scale model is solved by applying a fixed displacement on one end and keeping the other end roller constrained (Fig. 4.1). The fixed displacement, instead of a stress value, is applied in the core scale model because the lab triaxial compression is often conducted under a displacement-control mode (Cheng et al., 2015). The predicted elastic modulus, which is obtained using Eqs. 4.5 – 4.7, represents the relevant properties of dry shale samples because fluid is not considered in the void space of the proposed model.

6.3. Validation

Samples from Lower Bakken, Barnett, and Haynesville shales are analyzed to clarify the proposed model. Simpson et al., (2015) reported the relevant measurements for the Lower Bakken and Sone (2012) the measurements for the Barnett and the Haynesville formations. They measured the mineral composition from XRD analysis and determined the total porosity from mercury injection capillary pressure (MICP). They also reported the static anisotropic elastic modulus for each sample at the core scale (Table 6.3).

The input parameters of the revised model are listed in the seventh column in Table 6.1. The average grain size of the mineral is 12.55 μm (Milliken et al., 2012). The elastic moduli of the clay platelets are shown in Table 6.2. The clay platelet orientation in the model is 20 degrees with respect to the bedding planes, based on the study conducted by Hornby et al., (1994). It is assumed that the microporosity accounts for the total porosity, based on high-resolution images, and resides in the kerogen and the clay (Loucks et al., 2009). It is assumed that kerogen accounts for 50% of the microporosity because it is impossible to determine the corresponding values at the core scale. The aspect ratios of the pores in the kerogen and the clay aggregates are 0.33 and 0.05, respectively. The aspect ratios of the voids are reported for different shales in the literature (Hornby et al., 1994; Klaver et al., 2012).

For model implementation, the first step is to derive the elastic properties of the porous kerogen and the porous clay aggregates using the grain-scale model (Fig. 6.1). The elastic properties of the core scale model are determined by generating ten random realizations of the microfabric structure in the matrix. Fig. 6.2 shows one realization of the core-scale model which includes the complex microfabric structure. Fig. 6.3 presents the simulated anisotropic stress-strain curves for the core-scale model illustrated in Fig. 6.2. The predicted anisotropic elastic moduli at the core scale are determined according to Eq. 6.3. The predicted elastic moduli of the ten random realizations are averaged and plotted in Fig. 6.4 for each sample. The elastic modulus parallel to the axis of symmetry is denoted by E_3, whereas the modulus in the other direction is shown by E_1. The predicted E_1 is greater than the E_3 for each sample, which is consistent with the triaxial measurements. It is observed that 12 out of 16 predicted elastic moduli at the core scale differ less than 17% from the measured values (Fig. 6.4). The agreement between the predicted results and the measured values supports the proposed model.

For completeness, the average error of the predicted anisotropic elastic moduli to the lab measurements is analyzed for each shale formation. Eq. 6.7 is used to compute the error, which is plotted in Fig. 6.5. The average errors of the predicted elastic moduli are 10.5%, 9.5%, and 24.1% for the Lower Bakken, Barnett, and Haynesville shales, respectively. Therefore, the proposed model yields a good prediction of the anisotropic elastic properties of the three shale formations at the core scale.

$$Error\ (\%) = \frac{1}{N}\sum_{i=1}^{N}\left|\frac{E_i^{Predicted} - E_i^{Measured}}{E_i^{Measured}}\right| \times 100, \tag{6.7}$$

where *Error* is the average error of the predicted anisotropic elastic moduli with respect to the lab measurements of a shale formation, *N* is the number of measurements of the elastic moduli for the shale formation, $E_i^{Predicted}$ is the predicted elastic modulus parallel to or perpendicular to the axis of symmetry, and $E_i^{Measured}$ is the measured elastic modulus parallel to or perpendicular to the axis of symmetry.

The anisotropic elastic moduli are predicted based on the core-scale model that incorporates 20^3 (=20×20×20) cubic elements. The number of elements in the core-scale model is determined based on the sensitivity analysis: the predicted anisotropic elastic moduli show less variations among different realizations when the number of elements is equal to or larger than 20^3 (Fig. 6.6).

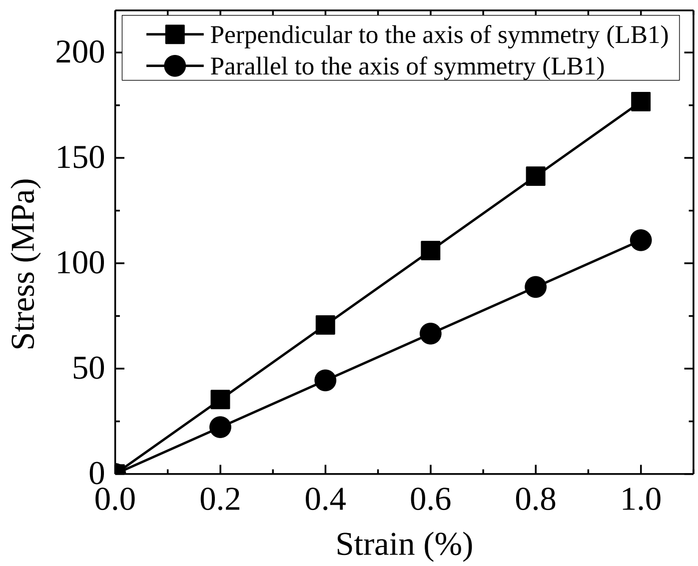

Figure 6.3 – Simulated anisotropic stress-strain curves for the core-scale model of the LB1 sample shown in Fig. 6.2. The predicted anisotropic elastic moduli were computed according to Eq. 6.3.

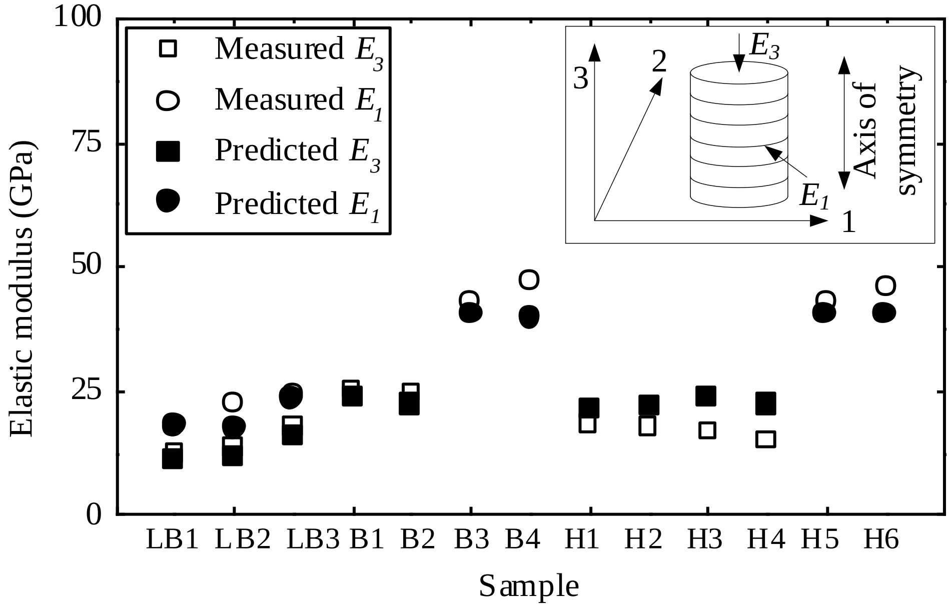

Figure 6.4 – Predicted anisotropic elastic moduli for the samples of Lower Bakken, Barnett, and Haynesville shales based on the revised hierarchical model.

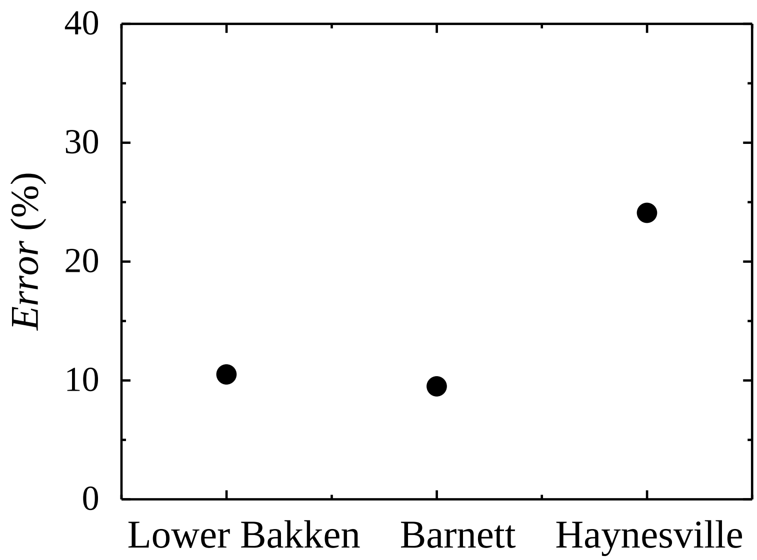

Figure 6.5 – Error of the predicted elastic modulus for the three shale formations.

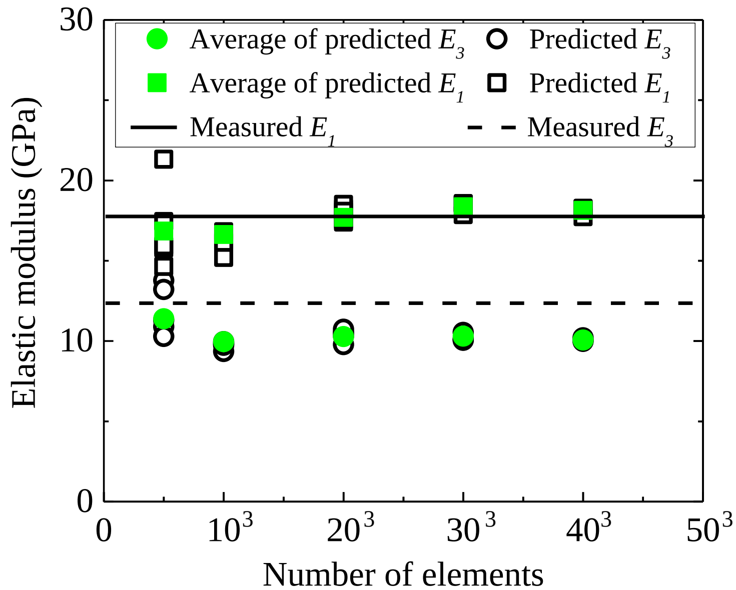

Figure 6.6 – Sensitivity of the predicted anisotropic elastic moduli to the number of elements in the core-scale model. The model is relevant to the LB1 sample.

6.4. Sensitivity analysis

The sensitivity analysis is presented in this section to systemically discuss the importance of each parameter for the anisotropic elasticity of a shale at the core scale. The sensitivity analysis also enables us to quantitatively evaluate the uncertainties of the predicted anisotropic moduli when a single value is used for a parameter in the proposed model. The LB1 sample is used to conduct the sensitivity analysis.

The maximum and the minimum of the anisotropic elastic moduli at the core scale (E_3^{min}, E_3^{max}, E_1^{min}, and E_1^{max}) can be determined by considering the full range of variation for each input parameter. Table 6.4 lists the corresponding input parameters for each scenario. Subsequently, every input parameter is changed individually to determine its effect on the elastic properties at the core scale.

First, the clay properties have significant effects on the anisotropic elastic moduli of shales at the core scale (Fig. 6.7). The entire range of the elastic moduli of the clays is considered (Table 6.2), while other parameters are fixed and equal to the values listed in Table 6.4. For reference conditions associated with (0, 0) in Fig. 6.7, the predicted E_3^{min}, E_3^{max}, E_1^{min}, and E_1^{max} are equal to 10.52, 15.14, 15.18, and 23.87 GPa, respectively, where the clay has the smallest anisotropic moduli E_1^{clay}= 29.24 GPa and E_3^{clay}= 14.26 GPa..4. The predicted anisotropic moduli of the LB1 increase up to 100% when the clay moduli are increased by 300%–500%. Sedimentary diagenesis causes the transformation of the clay minerals (Segonzac 1970), the effect of which can be predicted quantitatively using the proposed model.

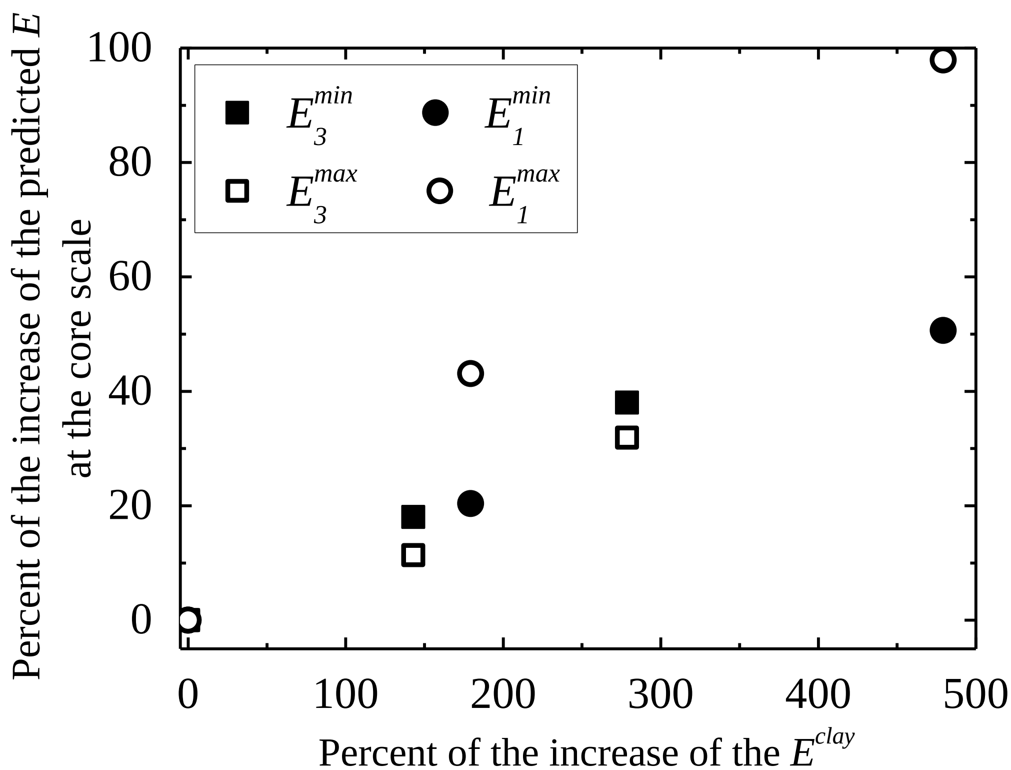

Figure 6.7 – Effect of clay moduli on the elastic moduli of the LB1 sample at the core scale.

Table 6.4 – Governing parameters that yield the maximum and minimum anisotropic elastic moduli (E_3^{min}, E_3^{max}, E_1^{min}, and E_1^{max}).

Void or matrix	Physical factors	Mathematical parameters	Variation	E_3^{min}	E_3^{max}	E_1^{min}	E_1^{max}
Matrix	Elastic anisotropy of clays	Anisotropic elastic moduli (E^{clay})	Table 6.2	Smallest E^{clay} (Table 6.2)	Greatest E^{clay} (Table 6.2)	Smallest E^{clay} (Table 6.2)	Greatest E^{clay} (Table 6.2)
	Clay platelet orientation	Orientation angle to the bedding	0 – 90°	0	90°	90°	0
	Structure of kerogen	Lenticular with geometric size	Unknown	$1-m$	$1-m$	$1-m$	$1-m$
	Structure of clay aggregates	Lenticular with geometric size	Unknown	$1-m$	$1-m$	$1-m$	$1-m$
	Mineral composition	Mineral volume fractions	–	LB1 in Table 6.3	LB1 in Table 6.3	LB1 in Table 6.3	LB1 in Table 6.3
Void	Macroporosity	ϕ_{macro} fraction	0 – 100%	0	0	0	0
	Topology of macropores	Aspect ratio (AR_m)	0.50 – 1.00	–	–	–	–
	Microporosity	ϕ_{micro} fraction	0 – 100%	100%	100%	100%	100%
	Kerogen porosity	$\phi_{kerogen}$ fraction	0 – 100%	0	0	0	0
	Clay aggregate porosity	ϕ_{clay} fraction	0 – 100%	100	100	100	100
	Topology of pores in kerogen	Aspect ratio (AR_k)	0.21 – 0.77	–	–	–	–
	Topology of pores in clay aggregates	Aspect ratio (AR_c)	0.05 – 1.00	0.05	0.05	0.05	0.05

* The detailed explanation of each parameter in this table can be found in Table 6.1.

Next, the clay platelet orientation is crucial for the anisotropic elastic properties of shales at the core scale (Fig. 6.8). The clay platelet orientation varies from 0 to 90 degrees with respect to the bedding plane, and Table 6.4 lists other input parameters. For reference conditions associated with (0, 0) in Fig. 6.8, the predicted E_3^{min}, E_3^{max}, E_1^{min}, and E_1^{max} are equal to 10.52, 23.87, 15.91, and 47.31 GPa, respectively, where the clay platelet is horizontal for 0 degree. The E_3^{min} and E_3^{max} increase by 31%–53% and the E_1^{min}, and E_1^{max} decrease by 37%−54% when the clay platelet orientation increases from 0 to 90 degrees. Thus, there is a stronger elastic anisotropy when the clay platelets show a more profound horizontal orientation. The proposed model helps us to numerically predict the anisotropy. The sedimentary compaction is likely to produce a greater horizontal orientation of the clay platelets (Hornby 1998). The net force between the clay platelets, whose surfaces are negatively charged, is also important because a net repulsion disperses the clay platelets (Lagaly and Ziesmer 2003) and affects the orientation.

Third, the microporosity fraction of clays significantly affects the anisotropic elastic moduli of shale at the core scale. Fig 6.9 shows that E_1 changes more significantly than E_3 when the void space in the clay accounts for a larger fraction. The observed trend is expected because pores in clay aggregates usually have smaller aspect ratios.

The effect of the pore aspect ratio in clay on the predicted anisotropic moduli is shown in Fig. 6.10. The predicted E_3^{min}, E_3^{max}, E_1^{min}, and E_1^{max} are 10.52, 24.61, 15.20, and 47.31 GPa, respectively, when the pore aspect ratio is equal to 0.05. Increasing the aspect ratio to one increases E_3^{min} and E_1^{min} by 30%–45% and decreases E_3^{max} and E_1^{max} by 15%–20%. In other words, a clay pore with a larger aspect ratio decreases the variation of the elastic moduli, which may reduce the anisotropic elasticity at the core scale. The observed trend indicates that the determination of the representative clay pore aspect ratios is also crucial for a quantitative understanding of the anisotropic elastic properties of a shale at the core scale.

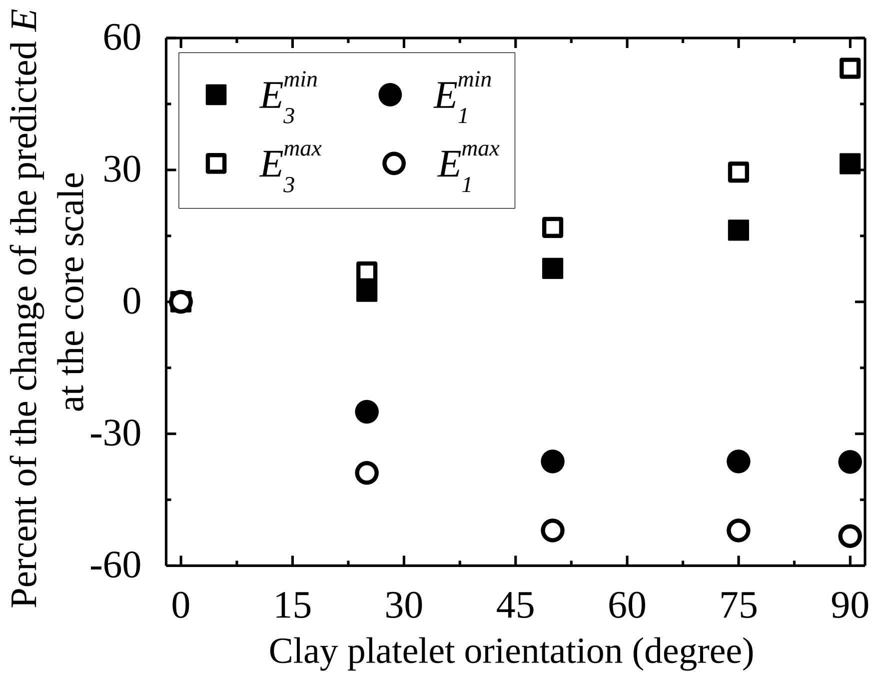

Figure 6.8 – Effect of clay platelet orientation on the elastic anisotropy of the LB1 sample at the core scale.

Finally, it is necessary to analyze the effects of the microfabric structures of kerogen and of clays on the predicted anisotropic moduli (Fig. 6.11). The proposed model indicates that E_3^{min}, E_3^{max}, E_1^{min}, and E_1^{max} are equal to 11.52, 24.61, 15.20, and 47.31 GPa, respectively, when the lenticular sizes are allowed to be equal to the core-scale model size. The lenticular size influences E_3^{min} and E_3^{max} more significantly than E_1^{min} and E_1^{max}. The observed trend occurs because the lenticular structures are parallel to the bedding. Researchers have studied the effect of the microfabric structure on the anisotropic elastic properties of shales (Vernik and Nur 1992), but the proposed model suggests that it needs to characterize the representative sizes to quantify the effect. The observed effect has not been discussed quantitatively in previous studies.

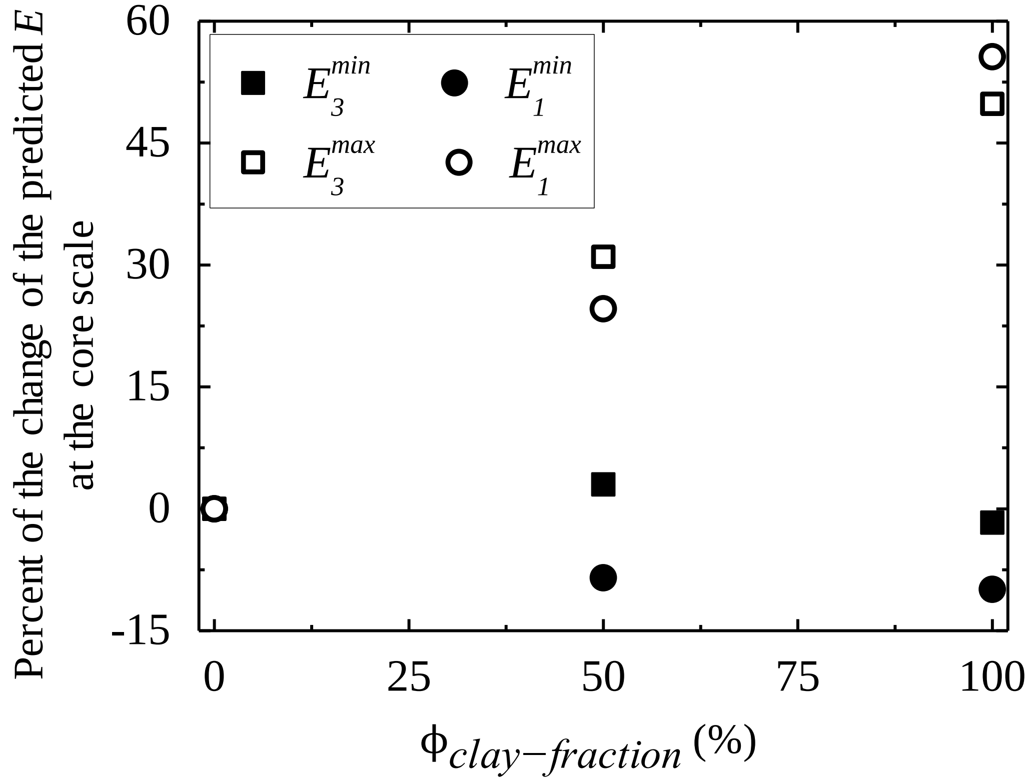

Figure 6.9 – The predicted elastic moduli of the LB1 sample vs. the microporosity in clays ($\phi_{clay\text{-}fraction}$). For reference conditions at (0, 0), the predicted E_3^{min}, E_3^{max}, E_1^{min}, and E_1^{max} are 10.89, 21.94, 13.99, and 31.66 GPa, respectively.

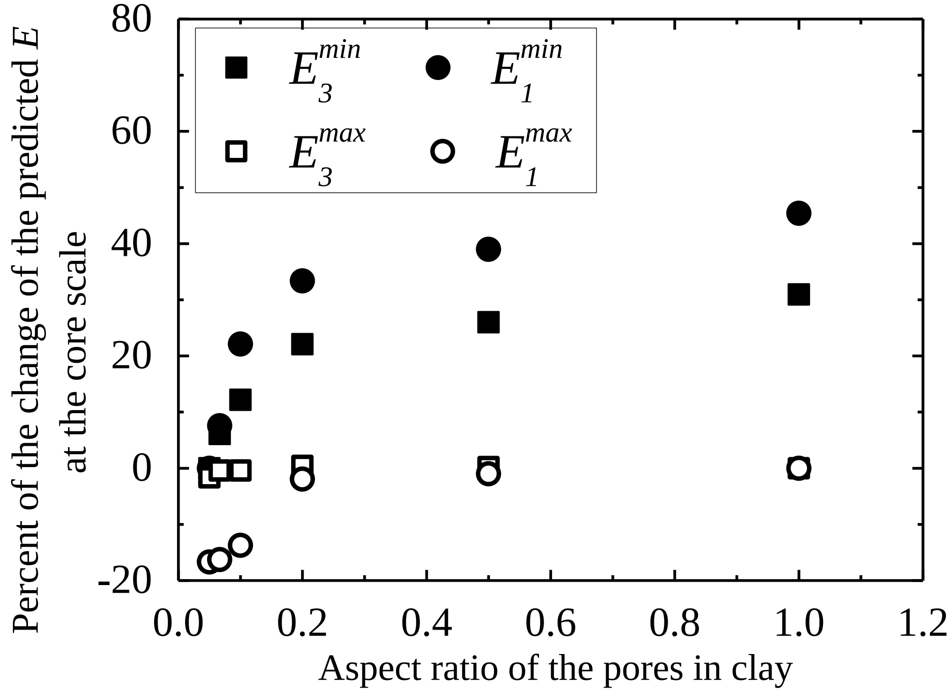

Figure 6.10 –The predicted anisotropic moduli of the LB1 sample at the core scale vs the clay pore aspect ratio. The predicted E_3^{min}, E_3^{max}, E_1^{min}, and E_1^{max} are 10.52, 24.61, 15.20, and 47.31 GPa, respectively, when the pore aspect ratio is 0.05.

The sensitivity analysis indicates that the clay elastic moduli and the clay platelet orientation have the most significant effects on the anisotropic elastic moduli of shales at the core scale. Other parameters—for instance, the microfabric structures of the kerogen and clays—also contribute slightly to the elastic anisotropy at the core scale. These conclusions are drawn from the sensitivity analysis of the Lower Bakken sample analyzed in this study. The applicability of these conclusions to other formations needs further investigation. In addition, the sensitivity analysis demonstrates that the predicted anisotropic elastic moduli of shales at the core scale may vary significantly, depending on the uncertainties of each governing parameter. Therefore, it is crucial to conduct a comprehensive investigation of all the governing parameters to make appropriate predictions of the elastic anisotropy at the core scale.

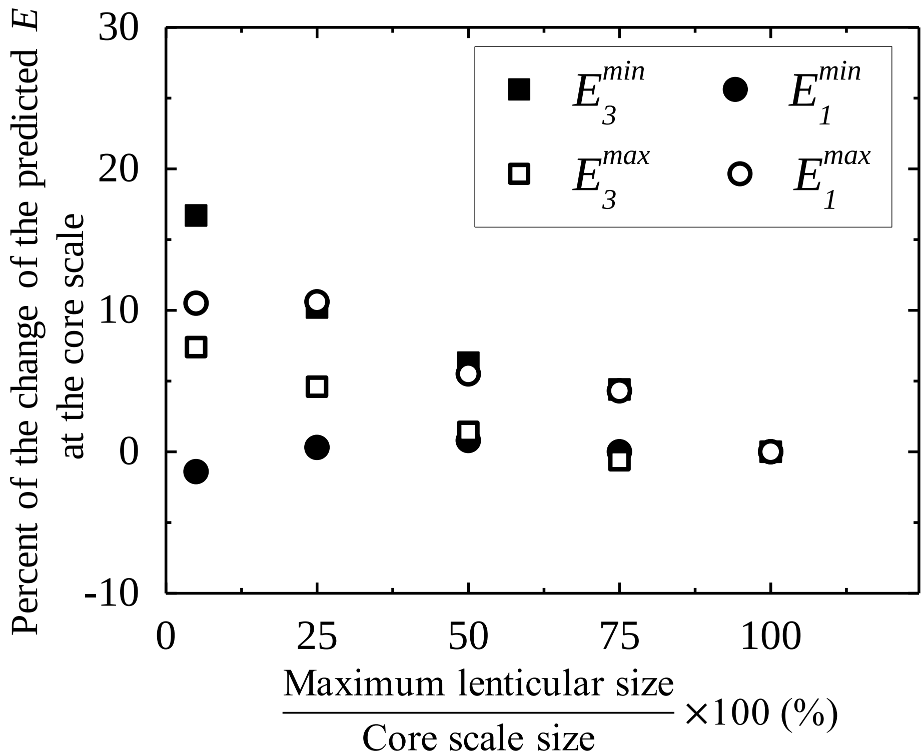

Figure 6.11 –The lenticular structures of kerogen and clays vs the elasticity of the LB1 at the core scale. For reference conditions at (100, 0), the predicted E_3^{min}, E_3^{max}, E_1^{min}, and E_1^{max} are 11.52, 24.61, 15.20, and 47.31 GPa, respectively.

6.5. Conclusions

The main objective of this chapter was to predict the anisotropic elastic properties of shales at the core scale based on the revised hierarchical model. The revised model accounts for the void system, the mineralogy, the grain-size distribution, and the microfabric structure of the rock matrix. The proposed model characterizes the effective properties of the formation at the small scale (grain scale), and predicts the anisotropic elastic moduli of shales at the large scale (core scale). It has been tested for the Lower Bakken, Barnett, and Haynesville shales. Most of the predicted anisotropic elastic moduli differ less than 17 percent from the independent measurements, which supports the proposed model. The sensitivity of the anisotropic moduli of shales to the governing parameters was also discussed based on one Lower Bakken sample. This is important because it allows us to systematically and quantitatively determine the importance of each parameter for the geomechanical characterization of shales at the core scale.

The proposed model has major implications for the characterization of the anisotropic geomechanical properties of shales at the core scale, which are important for in-situ stress analysis and the analysis of wellbore stability. It allows us to predict the quasi-static anisotropic elastic properties from drill cuttings, instead of cores or core-plugs, the recovery of which is difficult and expensive. The proposed model also enables us to gain a deep understanding of the anisotropic geomechanics of shales.

Chapter 7. Assumptions and Limitations of the Proposed Models

In this chapter, assumptions relevant to the applications of the proposed models are discussed. The limitations of the proposed models' applications are also elaborated for completeness. Other assumptions pertinent to the model development have been provided in the prior chapters.

7.1. A conceptual model of nanoindentation

For a conceptual model of nanoindentation, the assumption is that the predicted elastic properties are representative of the dynamic properties of shales at the core scale. This is because the elastic properties are interpreted from the unloading stages of nanoindentation, which are more relevant to the dynamic properties, as discussed by Zoback (2010). The predicted results capture the dynamic elastic properties of a given shale, as shown in Fig. 3.1.

The first limitation of the application of the conceptual model is that the load of the nanoindentation should be on the order of a few micro-Newtons in order to extract the loading frames with distinct mechanical properties. Bennett et al., (2015) conducted nanoindentations with various loads on the Woodford shale. They reported that a small load (~ 4 mN) allowed them to distinguish the loading frames with distinct mechanical properties, whereas a large load (200 ~ 400 mN) failed to do so because the grain-scale heterogeneity was suppressed under the large load. The proposed model predicts the core-scale elastic properties of shales based on the pertinent properties of the loading frames. Thus, nanoindentations of shales must be conducted using a small load for the application of the proposed model.

The second limitation for the application of the conceptual model is that the size of the shale sample should be large enough (~ mm) to exclude the boundary effect on the nanoindentation measurements. Eq. 7.1 allows us to approximate the size of the plastic zone in a nanoindentation (Johnson 1970). Substituting $E = 20\,GPa, \upsilon = 0.3$, and $\sigma_{yield}(\text{UCS}) = 35.8$ MPa of the Woodford shale in Eq. 3.3 (Abousleiman et al., 2007) results in *c/a* = 3.6. Thus, the size of the plastic zone, *c*, is about 2 μm for a Berkovich indentation on shale with a penetration depth of 200 nm (load ~ 4 mN). Therefore, the shale sample size has to be much greater than 2 μm (c) in order to minimize the boundary effect on the nanoindentation measurements. Ulm and Abousleiman (2006) suggested that the shale samples should be 5–10 mm thick for nanoindentation measurements.

$$\frac{c}{a} = \left[\frac{1}{6(1-\upsilon)}\left[\frac{E}{\sigma_{yield}} tan\beta + 4(1-2\upsilon)\right]\right]^{1/3}, \qquad (7.1)$$

where c is the radius of the hemispherical plastic zone, a ($= h\ tan\alpha$) is the radius of the projected elastic contact, h is the penetration depth, α is the half angle of the indenter, υ is the Poisson's ratio of the medium, E is the Young's modulus of the medium, σ_{yield} is the yield strength of the medium, and β ($= \frac{1}{2}\pi - \alpha$) is the slope of the indenter edge with respect to the horizontal direction.

7.2. The hierarchical model

For the hierarchical model, the assumption is that the predicted elastic moduli are relevant to the properties of the intact core plugs. The proposed model does not account for the presence of fractures. Thus, the predicted results are not representative of fractured shales or carbonates.

The first limitation of the proposed hierarchical model is that it does not account for the effects of the fluid-rock interaction on the geomechanical properties. The injected fluid, once it contacts the rock, may alter the properties because of swelling (Sayers and den Boer 2016) or cooling. The geomechanical properties of the sample may also be altered after recovery because of the escape of the saturation fluid. These fluid-rock interactions are not considered in the proposed model.

The second limitation is that the proposed model also does not account for the effects of temperature on the geomechanical properties of shales at the core scale. The implemented elastic properties of solid minerals in Table 4.1 are representative of standard conditions (room temperature). Hence, the model has been tested against laboratory measurements at identical conditions. The elastic properties of solid minerals at subsurface conditions (elevated temperature) have to be modified to mimic shale formations at in-situ conditions. Analyzing the temperature effects is beyond the scope of the present study.

Finally, the proposed model needs to be tested for other shale formations. It has been validated for several shale formations, such as the New Albany, Rock Mountain Siliceous, Lower Bakken, Barnett, and Haynesville. However, the applicability of the proposed model to other formations needs further study due to the heterogeneity of shales.

Chapter 8: Concluding Remarks and Future Work Recommendations

8.1. Concluding remarks

8.1.1. Nanoindentations of shales

The first objective of this study was to predict the elastic properties of a shale at the core scale from nanoindentation measurements that could be conducted on drill cuttings. This is important because it allows us to use drill cuttings instead of large samples (cores or blocks) for the geomechanical characterization of shales. It is difficult to recover large shale samples because they usually break along the bedding planes due to their mechanical instability.

For the objective, a conceptual model was proposed for interpreting the nanoindentations on shales, which are strongly heterogeneous. It is assumed that nanoindentation measures the effective stiffness of different minerals in a combined volume where the softer entities dominate the elastic behavior. The conceptual model relates the effective stiffness at the small scale to the pertinent properties of a shale at the core scale. The proposed model was applied on the Woodford shale, with a good agreement between the predicted elastic moduli and independent core-scale measurements.

Further evidence was given to highlight the importance of the effective stiffness of different minerals in the mechanical behavior of a shale at the core scale. The core-scale elastic properties of shales were computed from the volumetric average of the elastic properties of the forming minerals. The computed moduli were significantly greater than the elastic properties of the bulk volume. Therefore, the effective stiffness of different minerals must be considered when predicting the geomechanical properties of a shale at the core scale from small-scale measurements.

8.1.2. The hierarchical model

A hierarchical model was proposed to predict the elastic properties of a shale at the core scale from the mineralogy, porosity, pore structure, grain-size distribution, and microfabric structures. All these parameters can be determined from drill cuttings. This was the second objective of the present study.

The proposed method incorporates a small-scale model, which mimics the elastic deformation of a grain with a known mineralogy, and a large-scale model, which captures the elastic properties of shales at the core scale. In the small-scale model, a physically representative element was proposed to capture the elasticity of a grain by accounting for the mineralogy, micropore structure, and grain size. The representative elements were randomly distributed in the core-scale model by considering the volume fraction of each mineral. The finite element method was adopted to solve the hierarchical model and derive the elastic moduli of shales. The computed results were compared with independent lab measurements of the New Albany, Rocky Mountain Siliceous, Lower Bakken, and Barnett shales. The predicted results captured the measured moduli parallel to the bedding because the minerals were randomly distributed in the model.

The hierarchical model was applied to a carbonate (Arab-D) formation to predict its static elastic properties at the core scale from the mineralogy and the void system. Compared to shales, carbonates are mainly composed of calcite and dolomite and have more complex pore structures. The hierarchical model accounts for the complex pore structures in predicting the elastic properties of the Arab-D carbonate at the core scale.

The predicted elastic properties agree with independent lab measurements reported in the literature. The results also show that the pore structure plays an important role in the elastic moduli of the Arab-D carbonate formation. Therefore, the geomechanical properties of carbonates need not correlate with the total porosity alone. The hierarchical model enables us to quantitatively analyze the effect of pore structure on the elastic properties of carbonates at the core scale.

The hierarchical model was revised to predict the anisotropic elastic properties of shales at the core scale. For this, the clay anisotropy, clay platelet orientation, and microfabric structures of the kerogens and clays were included in the revised model. All these factors could contribute to the anisotropic elasticity of shales at the core scale. The revised hierarchical model was tested on Lower Bakken, Barnett, and Haynesville shale samples. The agreement between the predicted and measured anisotropic elastic moduli supports the revised model. A sensitivity analysis was conducted to systematically and quantitatively determine the importance of each parameter to the anisotropic elasticity of a Lower Bakken sample at the core scale. The analysis suggests that it is crucial to characterize the clay type, the clay platelet orientation, and the geometrical sizes of the kerogen and clay structures in order to gain a comprehensive understanding of the anisotropic elastic properties of shales at the core scale. Understanding the anisotropic behavior of shales is important for many field applications, such as in-situ stress interpretation and wellbore stability analysis.

8.2. Future work recommendations

8.2.1. Nanoindentation of shales

The proposed conceptual model based on nanoindentations does not necessarily capture the anisotropic elastic properties of a shale at the core scale. This is probably because the anisotropic elasticity of a shale may be affected by factors at length scales beyond nanoindentation measurements. For instance, a nanoindentation test probes a small volume of the sample, which may not necessarily include the bedding plane effect on the anisotropic elasticity of shales. Future work needs to be conducted to capture the anisotropic elastic properties of shales at the core scale from nanoindentations.

The conceptual model needs to be tested on other shale formations. It works well for the Woodford shale, as shown in Chapter 3. However, its applicability to other shale formations needs to be verified because shales are different due to their heterogeneity.

The conceptual model may be extended to predict the elastic properties of shales with different water saturations. This is because water can be trapped in the shale pores whose characteristic sizes are on the order nanometers (Sakhaee-Pour and Bryant 2015) whereas the penetration depth of a nanoindentation can be greater than 200 nm. Thus, nanoindentation can be used to quantify the alternation of local properties due to the water presence. The conceptual model may then be applied to relate the local changes to the core-scale properties.

8.2.2. The hierarchical model

The hierarchical model works well for the shale formations analyzed in the present study. Future work includes testing the model's applicability to other shales because different formations vary significantly in their mineralogy, matrix structure, and void systems.

The hierarchical model predicted elastic moduli that are relevant to the ambient conditions of shales because the mineral properties used in the model are relevant to the ambient conditions (room temperature). The elastic properties of solid minerals at subsurface conditions (elevated temperature) must be modified to mimic shale formations at in-situ conditions. The hierarchical model may be used to study the temperature effect on the core-scale elastic properties of shales by considering the temperature-dependency of the properties of the minerals.

The hierarchical model may be extended to predict the water effect on the elastic properties of shales at the core scale. To this end, the compressibility of water should be accounted for in the hierarchical model. The hierarchical model may also be extended to study the fluid-rock interaction at the core scale by taking into account the changes of the decrease of the clay minerals' properties.

The hierarchical model may be applicable to predict the creep and strength properties of shales at the core scale. Creep deformation significantly affects the permeability of shales (Sinha et al., 2013), while strength properties are crucial for wellbore stability analysis and the study of hydraulic fracturing (Papanastasiou 1997; Zeynali 2012). Unlike the elastic properties, the creep and strength properties are routinely obtained from destructive triaxial tests on core plugs, which significantly increases the cost of core analysis. Therefore, it would be of great importance to predict the creep and strength properties of shales at the core scale based on a hierarchical model that utilizes small-scale measurements on drill cuttings. Future work may be conducted to incorporate the creep and strength properties of minerals to accomplish this objective.

References

Abedi S., Slim M., Hofmann R., Bryndzia T., and Ulm F.J. 2015 "Nanochemo-Mechanical Signature of Organic-Rich Shales: A Coupled Indentation–EDX Analysis." *Acta Geotechnica*, 11(3), 1−14.

Abedi S., Slim M., and Ulm F.J. 2016 "Nanomechanics of Organic-Rich Shales: The Role of Thermal Maturity and Organic Matter Content on Texture." *Acta Geotechnica*, 11 (4), 775−787.

Abousleiman Y.N., Tran M.H., Hoang S., Bobko C.P., Ortega A. and Ulm F.J., 2007. "Geomechanics Field and Laboratory Characterization of the Woodford Shale: The Next Gas Play." In SPE Annual Technical Conference and Exhibition. Society of Petroleum Engineers.

Amadei B., 1996. "Importance of Anisotropy When Estimating and Measuring In Situ Stresses in Rock." *International Journal of Rock Mechanics and Mining Sciences & Geomechanics Abstracts*, 33(3):293−325.

Ameen MS, Smart BG, Somerville JM, Hammilton S, Naji NA 2009. "Predicting Rock Mechanical Properties of Carbonates From Wireline Logs (A Case Study: Arab-D Reservoir, Ghawar Field, Saudi Arabia)." *Marine and Petroleum Geology*, 26(4), 430−444.

Arbogast T., Cowsar L.C., Wheeler M.F., and Yotov I. 2000. "Mixed Finite Element Methods on Nonmatching Multiblock Grids." *SIAM Journal on Numerical Analysis*, 37 (4), 1295—1315.

Bachrach R., 2011. "Elastic and Resistivity Anisotropy of Shale During Compaction and Diagenesis: Joint Effective Medium Modeling and Field Observations."

Geophysics, 76(6), E175−E186.

Barkved O.I. and Kristiansen T., 2005. “Seismic Time-Lapse Effects and Stress Changes: Examples From A Compacting Reservoir.” *The Leading Edge*, 24(12), 1244−1248.

Barla G., 1974. “Rock Anisotropy: Theory and Laboratory Testing.” *Rock Mechanics*, 131−169.

Bec S., Tonck A. And Fontaine J., 2006. “Nanoindentation and Nanofriction on DLC Films.” *Philosophical Magazine*, 86(33-35), 5465−5476.

Bennett K.C., Berla L.A., Nix W.D., and Borja R.I. 2015. “Instrumented Nanoindentation and 3D Mechanistic Modeling of a Shale at Multiple Scales.” *Acta Geotechnica*, 10 (1), 1−14.

Bobko C.P., 2008. “Assessing the Mechanical Microstructure of Shale By Nanoindentation: The Link Between Mineral Composition and Mechanical Properties.” Doctoral Dissertation, Massachusetts Institute Of Technology.

Bobko C. And Ulm F.J. 2008 “The Nano-Mechanical Morphology of Shale.” *Mechanics of Materials*, 40 (4), 318−337.

Bourgoyne A.T., Millheim K.K., Chenevert M.E., and Young F.S. 1991. Applied Drilling Engineering. SPE, Rechardson, TX.

BP Statistical Review Of World Energy 2017. Available at Https://Www.Bp.Com/Content/Dam/Bp/En/Corporate/Pdf/Energy-Economics/Statistical-Review-2017/Bp-Statistical-Review-Of-World-Energy-2017-Full-Report.Pdf

Briscoe B.J., Fiori L. and Pelillo E., 1998. “Nano-Indentation Of Polymeric Surfaces.”

Journal Of Physics D: Applied Physics, 31(19), 2395.

Bryant, S. and Blunt, M., 1992. "Prediction Of Relative Permeability In Simple Porous Media." *Physical Review A*, 46(4), 2004.

Burchette TP 2012. "Carbonate Rocks And Petroleum Reservoirs: A Geological Perspective From The Industry." *Geological Society, London, Special Publications*, 370(1), 17−37.

Cantrell D.L. and Hagerty R.M., 1999. "Microporosity In Arab Formation Carbonates, Saudi Arabia." *Geoarabia*, 4(2), 129−154.

Cantrell DL, and Hagerty RM 2003. "Reservoir Rock Classification, Arab-D Reservoir, Ghawar Field, Saudi Arabia." *Geoarabia*, 8, 435−462.

Cantrell D, Swart P, and Hagerty R 2004. "Genesis And Characterization Of Dolomite, Arab-D Reservoir, Ghawar Field, Saudi Arabia." *Geoarabia*, 9(2), 11−36.

Chang C., Zoback M.D. and Khaksar A., 2006. "Empirical Relations Between Rock Strength And Physical Properties In Sedimentary Rocks." *Journal of Petroleum Science and Engineering*, 51(3-4), 223−237.

Chen X, Eichhubl P, and Olson JE. 2017. "Effect Of Water On Critical And Subcritical Fracture Properties Of Woodford Shale." *Journal of Geophysical Research: Solid Earth*.122(4):2736−50.

Chen Q., Nezhad M.M., Fisher Q., and Zhu H. 2016. "Multi-Scale Approach For Modeling The Transversely Isotropic Elastic Properties Of Shale Considering Multi-Inclusions And Interfacial Transition Zone." *International Journal of Rock Mechanics and Mining Sciences*, 84, 95−104.

Cheng Y.T. and Cheng C.M., 2004. "Scaling, Dimensional Analysis, and Indentation

Measurements." *Materials Science and Engineering: R: Reports*, 44(4), 91−149.

Cheng J., Wan Z., Zhang Y., Li W., Peng S.S. and Zhang P., 2015. "Experimental Study on Anisotropic Strength And Deformation Behavior of A Coal Measure Shale Under Room Dried and Water Saturated Conditions." *Shock and Vibration*, 2015.

Cho J.W., Kim H., Jeon S. and Min K.B., 2012. "Deformation and Strength Anisotropy Of Asan Gneiss, Boryeong Shale, and Yeoncheon Schist." *International Journal of Rock Mechanics and Mining Sciences*, 50, 158−169.

Chollacoop N., Dao M. and Suresh S., 2003. "Depth-Sensing Instrumented Indentation With Dual Sharp Indenters." *Acta Materialia*, 51(13), 3713−3729.

Choquette P.W. and Pray L.C., 1970. "Geologic Nomenclature and Classification of Porosity in Sedimentary Carbonates." *AAPG Bulletin*, 54(2), 207−250.

Constantinides G., Ulm F.J. and Van Vliet K., 2003. "On the Use of Nanoindentation for Cementitious Materials." *Materials And Structures*, 36(3), 191−196.

Croize D, Ehrenberg SN, Bjorlykke K, Renard F, and Jahren J 2010. "Petrophysical Properties of Bioclastic Platform Carbonates: Implications for Porosity Controls During Burial." *Marine and Petroleum Geology*, 27(8), 1765−1774.

Dahi-Taleghani A. and Olson J.E., 2011. "Numerical Modeling of Multistranded-Hydraulic-Fracture Propagation: Accounting for the Interaction Between Induced and Natural Fractures." *SPE Journal*, 16(03), 575−581.

Daniels J.L., Waters G.A., Le Calvez J.H., Bentley D. and Lassek J.T. 2007. "Contacting More of The Barnett Shale Through an Integration of Real-Time Microseismic Monitoring, Petrophysics, and Hydraulic Fracture Design." In SPE Annual Technical Conference And Exhibition. Society of Petroleum Engineers.

Daigle H, Hayman NW, Kelly ED, Milliken KL, and Jiang H. 2017. "Fracture Capture of Organic Pores In Shales." *Geophysical Research Letters*, 44(5), 2167–2176.

Donath F.A., 1961. "Experimental Study of Shear Failure in Anisotropic Rocks." *Geological Society of America Bulletin*, 72(6), 985–989.

Dugdale D.S., 1954. "Cone Indentation Experiments." *Journal of The Mechanics and Physics Of Solids*, 2(4), 265−277.

Dunham RJ. 1962. "Classification of Carbonate Rocks According to Depositional Texture." In: Ham, W.E. (Ed.), Classification Of Carbonate Rocks. *American Association of Petroleum Geologists Memoir*, Vol. 1, 108−121.

Eberli GP, Baechle GT, Anselmetti FS, and Incze ML 2003. "Factors Controlling Elastic Properties in Carbonate Sediments and Rocks." *The Leading Edge* 22(7):654−660.

Edgell HS 1997. "Significance of Reef Limestones as Oil and Gas Reservoirs in the Middle East and North Africa." In Preprint of the Report in the Meeting at the Sydney University.

Edimann K, Somerville JM, Smart BGD, Hamilton SA, and Crawford BR 1998. "Predicting Rock Mechanical Properties From Wireline Porosities." In SPE/ISRM Rock Mechanics in Petroleum Engineering. Society of Petroleum Engineers.

Emmanuel O.O., 2014. "Geologic Characterization and The Recognition Of Cyclicity in the Middle Devonian Marcellus Shale, Appalachian Basin, NE USA." Phd Dissertation, Colorado School Of Mines.

Farquhar RA, Somerville JM, and Smart BGD 1994. "Porosity as a Geomechanical Indicator: an Application of Core and Log Data and Rock Mechanics." In

European Petroleum Conference. Society of Petroleum Engineers.

Fischer-Cripps A.C. 2004 Nanoindentation, Springer. New York.

Ganneau F.P., Constantinides G. and Ulm F.J., 2006. “Dual-Indentation Technique for the Assessment of Strength Properties of Cohesive-Frictional Materials.” *International Journal of Solids and Structures*, 43(6), 1727−1745.

Gercek H., 2007. “Poisson's Ratio Values for Rocks.” *International Journal of Rock Mechanics and Mining Sciences*, 44(1), 1−13.

Gomez S.L. and He W., 2012. “Fighting Wellbore Instability: Customizing Drilling Fluids Based on Laboratory Studies of Shale-Fluid Interactions.” In IADC/SPE Asia Pacific Drilling Technology Conference and Exhibition. Society of Petroleum Engineers.

Goovaerts P. 1997. Geostatistics for Natural Resources Evaluation. Oxford University Press on Demand.

Gritto R, Korneev V, Elobaid E, Mohamed F, and Sadooni F 2014. “Seismic Detection Of Subsurface Karst-Like Structures.” In Qatar Foundation Annual Research Conference (No. 1, P. EEPP0551).

Herrmann H.J. and Luding S. 1998 “Modeling Granular Media on the Computer.” *Continuum Mechanics and Thermodynamics,* 10 (4), 189−231.

Hill R., Lee E.H. and Tupper S.J., 1947. “The Theory of Wedge Indentation of Ductile Materials.” *Proceedings of the Royal Society of London A: Mathematical, Physical and Engineering Sciences* 188(1013) 273−289.

Hornby B.E., Schwartz L.M. and Hudson J.A., 1994. “Anisotropic Effective-Medium Modeling of the Elastic Properties of Shales.” *Geophysics*, 59(10), 1570−1583.

Jaeger J.C., Cook N.G. and Zimmerman R., 2009. Fundamentals of Rock Mechanics. John Wiley & Sons.

Jarvie D. M., 2012 "Shale Resource Systems for Oil and Gas: Part 2−Shale-Oil Resource Systems." In J. A. Breyer, Ed., Shale Reservoirs−Giant Resources for the 21st Century: *AAPG Memoir* 97, 89−119.

Jin H. and Sonnenbergy S.A. 2013. "Characterization for Source Rock Potential of the Bakken Shales in the Williston Basin, North Dakota and Montana." Unconventional Resources Technology Conference, Denver, 12-14 August, URTEC1581243-MS.

Johnson K.L., 1970. "The Correlation of Indentation Experiments." *Journal of the Mechanics and Physics Of Solids*, 18(2), 115-126.

Johnson K.L. 1987. Contact Mechanics. Cambridge University Press.

Johnson K.L., Kendall K. and Roberts A.D., 1971. "Surface Energy and the Contact of Elastic Solids." *Proc. R. Soc. Lond. A*, 324(1558), 301−313.

Josh M., Esteban L., Delle Piane C., Sarout J., Dewhurst D.N. and Clennell M.B., 2012. "Laboratory Characterisation of Shale Properties." *Journal of Petroleum Science and Engineering*, 88, 107−124.

Kamali-Asl A., Ghazanfari E., Newell P. and Stevens M., 2018. "Elastic, Viscoelastic, and Strength Properties of Marcellus Shale Specimens." *Journal of Petroleum Science and Engineering*.

Klein C.A. and Cardinale G.F., 1993. "Young's Modulus and Poisson's Ratio of CVD Diamond." *Diamond and Related Materials*, 2(5-7), 918−923.

Landau LD, and Lifschitz. 1999. Theory of Elasticity. (Theoretical Physics, Vol. 7), 3rd

Edition, Butterworth-Heinemann, Oxford

Lawn B. and Wilshaw T.R., 1993. Fracture of Brittle Solids. Cambridge University Press.

Lenormand R, and Fonta O 2007. “Advances in Measuring Porosity and Permeability From Drill Cuttings.” In SPE/EAGE Reservoir Characterization and Simulation Conference. Society of Petroleum Engineers.

Levin V. and Markov M. 2005. “Elastic Properties of Inhomogeneous Transversely Isotropic Rocks.” *International Journal of Solids and Structures*, 42 (2), 393−408.

Levin V., Kanaun S. and Markov M., 2012. “Generalized Maxwell’s Scheme for Homogenization of Poroelastic Composites.” *International Journal of Engineering Science*, 61, 75−86.

Li X. and Bhushan B., 1998. “Measurement of Fracture Toughness of Ultra-Thin Amorphous Carbon Films.” *Thin Solid Films*, 315(1-2), 214−221.

Li C. and Chou T.W., 2003. “A Structural Mechanics Approach for the Analysis of Carbon Nanotubes.” *International Journal of Solids and Structures*, 40(10), 2487−2499.

Li W. and Sakhaee-Pour A., 2016. “Macroscale Young’s Moduli of Shale Based on Nanoindentations.” *Petrophysics*, 57(06), 597−603.

Li W. and Sakhaee-Pour A., 2018. “Two-Scale Geomechanicsl of Carbonates.” *Rock Mechanics and Rock Engineering*, https://doi.org/10.1007/s00603-018-1536-8.

Liu K., Ostadhassan M. and Bubach B., 2016. “Applications of Nano-Indentation Methods to Estimate Nanoscale Mechanical Properties of Shale Reservoir Rocks.” *Journal of Natural Gas Science and Engineering*, 35,1310−1319.

Liu K., Ostadhassan M. and Bubach B., 2018. “Application of Nanoindentation to

Characterize Creep Behavior of Oil Shales." *Journal of Petroleum Science and Engineering*, 167, 729−736.

Loucks R.G., Reed R.M., Ruppel S.C. and Jarvie D.M., 2009. "Morphology, Genesis, and Distribution of Nanometer-Scale Pores in Siliceous Mudstones of the Mississippian Barnett Shale." *Journal of Sedimentary Research*, 79(12), 848−861.

Loucks R.G. and Ruppel S.C., 2007. "Mississippian Barnett Shale: Lithofacies and Depositional Setting of a Deep-Water Shale-Gas Succession in the Fort Worth Basin, Texas." *AAPG Bulletin*, 91(4), 579−601.

Lucia, F.J., 1995. "Rock-Fabric/Petrophysical Classification of Carbonate Pore Space for Reservoir Characterization." *AAPG Bulletin*, 79(9), 1275−1300.

Lucia FJ 2007. Carbonate Reservoir Characterization: An Integrated Approach. Springer Science & Business Media.

Lucia FJ, Jennings JW, Rahnis M, and Meyer FO 2001. "Permeability and Rock Fabric From Wireline Logs, Arab-D Reservoir, Ghawar Field, Saudi Arabia." *Geoarabia*, 6, 619−646.

Mavko G, Mukerji T, and Dvorkin J. 2009 The Rock Physics Handbook: Tools for Seismic Analysis Of Porous Media. Cambridge University Press.

Maxwell S. 2011 "Microseismic Hydraulic Fracture Imaging: The Path Toward Optimizing Shale Gas Production." *The Leading Edge*.30(3):340−6.

Milliken KL, Esch WL, Reed RM, and Zhang T. 2012 "Grain Assemblages and Strong Diagenetic Overprinting in Siliceous Mudrocks, Barnett Shale (Mississippian), Fort Worth Basin, Texas." *AAPG Bulletin*. 96(8), 1553−78.

Milliken KL, Rudnicki M, Awwiller DN, and Zhang T. 2013 "Organic Matter–Hosted

Pore System, Marcellus Formation (Devonian), Pennsylvania." *AAPG Bulletin*. 97(2), 177−200.

Monfared S. and Ulm FJ. 2016 "A Molecular Informed Poroelastic Model for Organic-Rich, Naturally Occurring Porous Geocomposites." *Journal of the Mechanics and Physics of Solids*. 88, 186−203.

Montgomery C.T. and Smith M.B. 2010 "Hydraulic Fracturing: History of an Enduring Technology." *Journal of Petroleum Technology*, 62(12), 26−40.

Mukerji T., Berryman J., Mavko G. and Berge P., 1995. "Differential Effective Medium Modeling of Rock Elastic Moduli with Critical Porosity Constraints." *Geophysical Research Letters*, 22(5), 555−558.

Neveux L, Grgic D, Carpentier C, Pironon J, Truche L, and Girard JP 2014. "Experimental Simulation of Chemomechanical Processes During Deep Burial Diagenesis of Carbonate Rocks." *Journal of Geophysical Research: Solid Earth*, 119(2), 984−1007.

Oliver W.C. and Pharr G.M. 1992 "An Improved Technique for Determining Hardness and Elastic Modulus Using Load and Displacement Sensing Indentation Experiments." *Journal of Materials Research*, 7(06), 1564−1583.

Ortega J.A., Ulm F.J., and Abousleiman Y. 2007 "The Effect of the Nanogranular Nature of Shale on Their Poroelastic Behavior." *Acta Geotechnica*, 2(3), 155−182.

Page, T.F., Oliver, W.C. and Mchargue, C.J., 1992. "The Deformation Behavior of Ceramic Crystals Subjected to Very Low Load (Nano) Indentations." *Journal of Materials Research*, 7(2), 450−473.

Papanastasiou, P., 1997. "The Influence of Plasticity in Hydraulic Fracturing."

International Journal of Fracture, 84(1), 61−79.

Pommer M, and Milliken K. 2015. “Pore Types and Pore-Size Distributions Across Thermal Maturity, Eagle Ford Formation, Southern Texas.” *AAPG Bulletin* 99(9):1713−44.

Popov V.L., 2010. Contact Mechanics and Friction. Berlin: Springer Berlin Heidelberg.

Ramamurty U. and Kumaran M.C., 2004. “Mechanical Property Extraction Through Conical Indentation of a Closed-Cell Aluminum Foam.” *Acta Materialia*, 52(1), 181−189.

Rogen B, Fabricius IL, Japsen P, Hoier C, Mavko G, and Pedersen JM 2005. “Ultrasonic Velocities of North Sea Chalk Samples: Influence of Porosity, Fluid Content and Texture.” *Geophysical Prospecting*, 53(4), 481−496.

Rybacki E., Meier T. and Dresen G., 2016. “What Controls the Mechanical Properties of Shale Rocks?–Part II: Brittleness.” *Journal of Petroleum Science and Engineering*, 144, 39−58.

Saenger E. H., Vialle S., Lebedev M., Uribe D., Osorno M., Duda M., and Steeb H., 2016. “Digital Carbonate Rock Physics.” *Solid Earth*, 7, 1185-1197, Doi:10.5194/Se-7-1185-2016.

Sakhaee-Pour A. 2009 “Elastic Properties of Single-Layered Graphene Sheet.” *Solid State Communications*, 149(1), 91−95.

Sakhaee-Pour A, and Bryant S. 2012 “Gas Permeability of Shale.” *SPE Reservoir Evaluation & Engineering*. 15(04):401−9.

Sakhaee-Pour A. and Bryant S.L. 2015. “Pore Structure of Shale.” *Fuel*, 143, 467–475.

Sakhaee-Pour A. and Li W. 2018 “Two-Scale Geomechanics of Shale.” *SPE Reservoir*

Evauation & Engineering. In Press.

Sakhaee-Pour A, and Tran H. 2017. "The Permeability of a Representative Carbonate Volume with a Large Vug." *Transport in Porous Media*, 120(3), 515−534.

Salehi I. 2010. New Albany Shale Gas Project Final Report 07112-16. The Research Partnership to Secure Energy for America, Http://www.rpsea.org/projects/07122-16/.

Samuels L.E. and Mulhearn T.O., 1957. "An Experimental Investigation of the Deformed Zone Associated with Indentation Hardness Impressions." *Journal of the Mechanics and Physics of Solids*, 5(2), 125−134.

Santos ES, and Ferreira FH 2010. "Mechanical Behavior of a Brazilian Off-Shore Carbonate Reservoir." In 44th US Rock Mechanics Symposium and 5th US-Canada Rock Mechanics Symposium. American Rock Mechanics Association.

Sayers CM. 2005. "Seismic Anisotropy of Shales." *Geophysical Prospecting*. 53(5):667−76.

Sayers CM 2008. "The Elastic Properties of Carbonates." *The Leading Edge*, 27(8), 1020−1024.

Sayers C.M. and Den Boer L.D., 2016. "The Elastic Anisotropy of Clay Minerals." *Geophysics*, 81(5), C193−C203.

Sayers C.M. and Schutjens P.M., 2007. "An Introduction to Reservoir Geomechanics." *The Leading Edge*, 26(5), 597−601.

Sesetty V. and Ghassemi A. 2015 "A Numerical Study of Sequential and Simultaneous Hydraulic Fracturing in Single and Multi-Lateral Horizontal Wells." *Journal of Petroleum Science and Engineering*, 132, 65−76.

Shi Y. and Falk M.L., 2007. "Stress-Induced Structural Transformation and Shear Banding During Simulated Nanoindentation of a Metallic Glass." *Acta Materialia*, 55(13), 4317−4324.

Shukla P., Kumar V., Curtis M., Sondergeld C.H. and Rai C.S., 2013. "Nanoindentation Studies on Shales." In 47th US Rock Mechanics/Geomechanics Symposium. American Rock Mechanics Association.

Simpson G., Hohman J., and Pirie I. 2015. "Using Advanced Logging Measurements to Develop a Robust Petrophysical Model for The Bakken Petroleum System." In SPWLA 56th Annual Logging Symposium. Society of Petrophysicists and Well-Log Analysts.

Sinha S., Braun E.M., Determan M.D., Passey Q.R., Leonardi S.A., Boros J.A., Wood Iii A.C., Zirkle T. and Kudva R.A., 2013. "Steady-State Permeability Measurements on Intact Shale Samples at Reservoir Conditions-Effect of Stress, Temperature, Pressure, and Type Of Gas." In SPE Middle East Oil and Gas Show and Conference. Society of Petroleum Engineers.

Soliman M.Y., Hunt J.L. and El Rabaa A.M., 1990. "Fracturing Aspects of Horizontal Wells." *Journal of Petroleum Technology*, 42(08), 966−973.

Soliman M.Y., East L. and Adams D., 2004. "Geomechanics Aspects of Multiple Fracturing of Horizontal and Vertical Wells." In SPE International Thermal Operations and Heavy Oil Symposium and Western Regional Meeting. Society of Petroleum Engineers.

Sone H. 2012 "Mechanical Properties of Shale Gas Reservoir Rocks, and its Relation to the In-Situ Stress Variation Observed in Shale Gas Reservoirs." Doctoral

Dissertation, Stanford University.

Sone H. 2018. Personal Communications.

Sone H and Zoback MD. 2013a. "Mechanical Properties of Shale-Gas Reservoir Rocks−Part 1: Static and Dynamic Elastic Properties and Anisotropy." *Geophysics*.78(5), 381−92.

Sone H. and Zoback M.D. 2013b. "Mechanical Properties of Shale-Gas Reservoir Rocks−Part 2: Ductile Creep, Brittle Strength, and Their Relation to the Elastic Modulus." *Geophysics*, 78(5), D393−D402.

Srodon J., Drits V.A., McCarty D.K., Hsieh J.C. and Eberl D.D. 2001. Quantitative X-Ray Diffraction Analysis of Clay-Bearing Rocks From Random Preparations. *Clays and Clay Minerals*, 49(6): 514−528.

Suryanarayana C. and Norton M.G. 2013. X-Ray Diffraction: A Practical Approach. Springer Science & Business Media.

Tabor D. 1956. "The Physical Meaning of Indentation and Scratch Hardness." *British Journal of Applied Physics*, 7(5), 159.

Tabor D. 1985. "Indentation Hardness and its Measurement: Some Cautionary Comments. in Microindentation Techniques in Materials Science and Engineering." *ASTM International*.

Tabor D. 1996. "Indentation Hardness: Fifty Years on A Personal View." *Philosophical Magazine* A, 74(5), 1207−1212.

Tran M.H. 2009 "Geomechanics Field and Laboratory Characterization of Woodford Shale." M.S. Thesis, University Of Oklahoma.

Ulm F.J. and Abousleiman Y. 2006 "The Nanogranular Nature of Shale." *Acta*

Geotechnica, 1(2), 77−88.

Ulm F.J., Vandamme M., Bobko C., Alberto Ortega J., Tai K. and Ortiz C., 2007. “Statistical Indentation Techniques for Hydrated Nanocomposites: Concrete, Bone, and Shale.” *Journal of the American Ceramic Society*, 90(9), 2677−2692.

US EIA 2017 Annual Energy Outlook 2017 With Projections To 2050. Washington DC: Energy Information Administration, United States Department Of Energy.

Vachaparampil A, and Ghassemi A. 2017. “Failure Characteristics of Three Shales Under True-Triaxial Compression”. *International Journal of Rock Mechanics and Mining Sciences*. 31;100:151−9.

Vermylen J. 2011 “Geomechanical Studies of the Barnett Shale, Texas, USA.” Phd Dissertation, Stanford University.

Veytskin YB, Tammina VK, Bobko CP, Hartley PG, Clennell MB, Dewhurst DN, and Dagastine RR. 2017 “Micromechanical Characterization of Shales Through Nanoindentation and Energy Dispersive X-Ray Spectrometry.” *Geomechanics for Energy and the Environment*.9, 21−35.

Vernik L. and Liu X., 1997. “Velocity Anisotropy in Shales: A Petrophysical Study.” *Geophysics*, 62(2), 521−532.

Walton G, Arzua J, Alejano LR, and Diederichs MS 2015. “A Laboratory-Testing-Based Study on the Strength, Deformability, and Dilatancy of Carbonate Rocks at Low Confinement.” *Rock Mechanics and Rock Engineering*, 48(3), 941−958.

Wang Z. 2002. “Seismic Anisotropy in Sedimentary Rocks, Part 2: Laboratory Data.” *Geophysics*, 67(5), 1423−1440.

Wang HF 2017. Theory of Linear Poroelasticity with Applications to Geomechanics and

Hydrogeology. Princeton University Press.

Wang Z., Wang H. and Cates M.E., 2001. “Effective Elastic Properties of Solid Clays.” *Geophysics*, 66(2), 428−440.

Ward C.R., Taylor J.C., and Cohen D.R. 1999. Quantitative Mineralogy of Sandstones by X-Ray Diffractometry and Normative Analysis. *Journal of Sedimentary Research*, 69(5): 1050−1062.

Warpinski NR, Mayerhofer M, Agarwal K, and Du J. 2013 “Hydraulic-Fracture Geomechanics and Microseismic-Source Mechanisms.” *SPE Journal*.18(04):766−80.

Weger RJ, Eberli GP, Baechle GT, Massaferro JL, and Sun YF 2009. “Quantification of Pore Structure and its Effect on Sonic Velocity and Permeability in Carbonates.” *AAPG Bulletin*, 93(10), 1297−1317.

Wong RC, Schmitt DR, Collis D, and Gautam R. 2008 “Inherent Transversely Isotropic Elastic Parameters of Over-Consolidated Shale Measured by Ultrasonic Waves and Their Comparison with Static and Acoustic In Situ Log Measurements.” *Journal of Geophysics and Engineering*. 5(1):103.

Wong G.K., Dudley J.W., Golovin E., Zhang H. and Chudnovsky A., 2017. “Injector Completion Performance Under Hydraulic Fracturing and Matrix Flooding Conditions into A Sand Pack.” In 51st US Rock Mechanics/Geomechanics Symposium. American Rock Mechanics Association.

Wright W.J., Saha R. and Nix W.D., 2001. “Deformation Mechanisms of the Zr40Ti14Ni10Cu12Be24 Bulk Metallic Glass.” *Materials Transactions*, 42(4), 642−649.

Xu J. and Sonnenberg S., 2016. "Brittleness and Rock Strength of the Bakken Formation, Williston Basin, North Dakota." Unconventional Resources Technology Conference (URTEC).

Zapata Y. and Sakhaee-Pour A. 2016. "Modeling Adsorption–Desorption Hysteresis in Shales: Acyclic Pore Model." *Fuel*, 181, 557–565.

Zeynali M.E., 2012. "Mechanical and Physico-Chemical Aspects of Wellbore Stability During Drilling Operations." *Journal of Petroleum Science and Engineering*, 82, 120–124.

Zhu W., Hughes J.J., Bicanic N. nd Pearce C.J., 2007. "Nanoindentation Mapping of Mechanical Properties of Cement Paste and Natural Rocks" *Materials Characterization*, 58(11-12), 1189−1198.

Zhu W., Fonteyn M.T.J., Hughes J. and Pearce C. 2009 "Nanoindentation Study of Resin Impregnated Sandstone and Early-Age Cement Paste Specimens." In Nanotechnology In Construction 3, 403−408, Springer, Berlin Heidelberg.

Zimmerman R. 2000 "Coupling on Poroelasticity and Thermoelasticity." *International Journal of Rock Mechanics and Mining Sciences*, 37(1), 79−87.

Zoback M.D. 2010 Reservoir Geomechanics. Cambridge University Press.

Appendix

This appendix shows the title pages of the journal publications relevant to the dissertation.

PETROPHYSICS, VOL. 57, NO. 6 (DECEMBER 2016); PAGE 597–603; 5 FIGURES; 2 TABLES

Macroscale Young's Moduli of Shale Based on Nanoindentations

Wenfeng Li[1] and A. Sakhaee-Pour[1]

ABSTRACT

It remains difficult to relate shale nanoscale measurements to core- and block-scale properties because of the heterogeneous structure of shale. One of the main reasons for this difficulty is the heterogeneity of natural nanogranular media, which is scale dependent. In this study, we propose a new conceptual model for the elastic deformation of a shale formation. The conceptual model accounts for the effective stiffness of small-scale constitutive entities at a large scale. We use the proposed model to determine macroscale Young's moduli by analyzing nanoindentations. Independent macroscale measurements corroborate our model.

INTRODUCTION

The petrophysical characterization of a shale formation, which can be considered to be a natural nanogranular composite, remains a challenging problem because of its heterogeneous structure. The heterogeneity exists at different scales, which makes it even more difficult for us to understand the pore space and the solid phases forming the matrix (Gupta et al., 2013; Sakhaee-Pour and Bryant, 2015).

The elastic properties of shale play critical roles in formation stimulation, well-log interpretation, drilling design, and production estimation. Determining these properties by conventional methods is time consuming and may even become impractical for shales. A large shale sample usually breaks into pieces during recovery due to the lack of mechanical stability. Hence, the notion of finding large-scale (core-scale, block-scale, or log-scale) properties from relevant properties of forming entities, such as organic and clay minerals, has gained attention among researchers (Bobko and Ulm, 2008; Kumar et al., 2012; Bennett et al., 2015). The key assumption is that knowing the elastic properties of the forming entities can enable us to predict the elastic properties of shale at a larger scale.

Researchers have analyzed the fundamental properties of shale that control its deformation. They have conducted measurements using nanoindenters (Bobko, 2008) and scanning electron microscopes (Bennett et al., 2015) and have been able to relate the nanoindentation to smaller-scale measurements (Abedi et al., 2016). Researchers have also worked on upscaling the results and have reported some correlations (Shukla et al., 2013), but it is not yet clear if there is a close relationship between the measurements made so far and the relevant properties at the large scale.

In the present study, we propose a new model to account for the heterogeneity of shale at the nano- and microscales. Our model allows us to predict the elastic deformation by accounting for the relative stiffness of the constitutive entities at the small scale. We test our model with independent macroscale measurements.

NANOSCALE MEASUREMENTS

We briefly review nanoindentation here because the relevant measurements are used in this study. We usually conduct nanoindentation to determine the Young's modulus and mechanical hardness of a solid medium. A hard tip with known geometry and mechanical properties is placed on the surface of the solid medium. We then increase the force continuously and record the penetration depth. The force-displacement measurements (Fig. 1) allow us to calculate the indentation modulus and the hardness as follows (Fischer-Cripps, 2011; Bennett et al., 2015):

$$M = \frac{\sqrt{\pi}}{2\alpha}\frac{S}{\sqrt{A_c}} \quad (1)$$

$$H = \frac{P}{A_c}, \quad (2)$$

where M is the indentation modulus, α is a correction factor related to the geometry of the indenter ($\alpha = 1.034$ for a Berkovich tip), S is the slope of the force-displacement curve at the beginning of the unloading (Fig. 1), A_c is the projected contact area (Oliver and Pharr, 1992), H is the

Manuscript received by the Editor February 10, 2016; revised manuscript received June 30, 2016; manuscript accepted August 4, 2016.
[1]Petroleum and Geological Engineering Department, The University of Oklahoma, 100 E. Boyd Street, Sarkeys Energy Center, SEC 1210, Norman, Oklahoma 73019, USA; wenfeng.li@ou.edu; sakhaee@ou.edu

Two-Scale Geomechanics of Shale

A. Sakhaee-Pour and **Wenfeng Li,** University of Houston

Summary

The geomechanical properties of reservoirs, which are important for formation stimulation, are often determined from triaxial tests on large-scale samples such as core plugs or blocks. It is difficult to recover large samples from shale formations because they are mechanically unstable and usually break down into pieces. The present study develops a two-scale model that uses drill cuttings to estimate the static elastic properties of shales at the core scale. We first propose a physically representative element to capture the elastic deformation of a solid grain with a known minerology by accounting for the grain size and its elastic properties using the structural-mechanics approach (a small-scale model). We then develop a core-scale model dependent on the volume fractions of the minerals, which are obtained from X-ray diffraction (XRD), for different realizations of the spatial distribution of the solid grains (large-scale model). The sensitivity of the large-scale model to the number of the elements is tested. The proposed model shows promising results for four shale formations (New Albany, Rocky Mountain Siliceous, Lower Bakken, and Barnett) and has major applications for the geomechanical characterization of a formation from drill cuttings.

Introduction

Hydrocarbon production from shale formations, which has become economically feasible because of hydraulic fracturing, has launched a new era in petroleum engineering. The implications are relevant to a wide range of issues, including natural-fracture characterization (Laubach et al. 2000; Ortega et al. 2006; Pommer et al. 2013), fluid-driven fracture propagation (Sheibani and Olson 2013; Gale et al. 2014), and transport-properties evolution. For the first time, researchers analyzed the fundamental behavior of a granular composite (shale) subject to the changes in effective stress and pore pressure to better predict energy transport in the source rock (Gutierrez et al. 2001; Xie et al. 2015; Wheaton 2017).

The matrix of a shale can be considered a natural nanocomposite for various reasons. First, it is heterogeneous because it is composed of different minerals, such as quartz, calcite, and dolomite. The grain size in the matrix is usually on the order of micrometers or submicrometers (Loucks et al. 2009; Milliken et al. 2013). Second, the transport properties of the matrix of a shale are controlled by the nanosized pore throats (Sakhaee-Pour and Bryant 2012, 2014). Third, the geomechanical properties of a shale are heterogeneous and depend on the length scale (Ulm and Abousleiman 2006; Bennett et al. 2015). Thus, the poroelastic response of a shale depends on the combined response of the small-size pores and grains (Cheng et al. 1993; Ortega et al. 2007).

Despite researchers' interest in understanding shale formations, basic knowledge about their fundamental behavior is fairly limited. This is in contrast to synthetic nanostructures, such as graphene sheets and carbon nanotubes, the responses of which to different loadings, such as tension (Sakhaee-Pour 2009a), compression (Sakhaee-Pour 2009b), and vibration (Sakhaee-Pour et al. 2008), have been successfully modeled.

Heterogeneity is the main difference between a natural nanocomposite (shale) and a synthetic nanocomposite, such as a graphene sheet, built under controlled conditions. For synthetic nanocomposites, researchers can use a single representative element (unit cell) to mimic the large-scale behavior (Li and Chou 2003). But in shale formations, the large-scale model (at the core or block scale) encompasses grains for which sizes and mineralogy vary spatially (Anders et al. 2014). It also remains difficult to implement a realistic spatial distribution for the minerals at the core scale. Thus, most studies, including the present work, are dependent on the assumption that the minerals are randomly distributed in the large-scale model (Mavko et al. 2009).

Another issue is the mechanical stability of shales. Shale samples often break down into pieces during extraction, unlike samples taken from conventional formations such as sandstones. The difficulty of recovering a large-scale sample complicates the assessment of core- and block-scale properties. Thus, researchers have sought alternative methods for determining the geomechanical properties using drill cuttings. For instance, they have made nanoindentations on a small sample (a subcore scale) and analyzed the relation between the measured values and those of the core scale and the block scale (Ulm and Abousleiman 2006). Abedi et al. (2016a, 2016b) conducted nanoindentation and energy-dispersive X-ray (EDX) spectroscopy to identify the microscale elastic properties of the forming constituents in shales. The microscale properties are not necessarily equal to the elastic properties of the core plug. Saxena and Mavko (2015) and Saxena et al. (2015) also proposed analytical models to estimate the effective elastic properties of sandstones and carbonates with good accuracy, but the applicability of their models to shale formations has not been tested.

Researchers used nanoindentation to predict the large-scale properties. Bennett et al. (2015) nanoindented shale samples with different penetration depths to determine the macroscale properties. Li and Sakhaee-Pour (2016) developed a conceptual model to account for the effective stiffness of the solid grain, dependent on the nanoindentation, and scaled up the results to the core scale. The proposed models predict the elastic properties at the large scale but require nanoindentations. Further, they do not determine the effects of forming minerals on the large-scale properties.

Different groups of researchers proposed analytical models to predict the elastic properties of the shale formation dependent on forming minerals. Mavko et al. (2009) reviewed some of those studies. For instance, Levin and Markov (2005) and Levin et al. (2012) used an effective-medium theory to predict the elastic properties. The homogenization theory was also adopted to predict the large-scale properties by accounting for the mineral contents and porosity (Ortega et al. 2007; Chen et al. 2016; Monfared and Ulm 2016). The error associated with the analytical method was on the order of 40 to 50% for different shales (Ortega et al. 2007; Monfared and Ulm 2016). The analytical models determine the effects of forming minerals, but they are complex and difficult to implement. Most importantly, they are limited to simplified geometries for the void and the grain.

The present study proposes a two-scale finite-element model, which is a numerical method, to predict the elastic modulus of the shale at the core scale. The finite-element method can include more-complicated geometries for the void and the solid grain, as opposed

Original SPE manuscript received for review 5 December 2016. Revised manuscript received for review 22 September 2017. Paper (SPE 189965) peer approved 16 October 2017.

Rock Mechanics and Rock Engineering
https://doi.org/10.1007/s00603-018-1536-8

ORIGINAL PAPER

Two-Scale Geomechanics of Carbonates

Wenfeng Li[1] · A. Sakhaee-Pour[1]

Received: 11 March 2017 / Accepted: 20 June 2018

Abstract

The geomechanical characterization of a carbonate reservoir is required for formation stimulation and hydrocarbon recovery. The pertinent core- or block-scale (large-scale) characterizations are time consuming and expensive, and more importantly, cannot be used for drill cuttings. The present study proposes a two-scale model based on microscale (small-scale) measurements to predict the geomechanical properties of a carbonate formation at the core scale. At the small scale, we develop a physically representative element by accounting for the effective stiffness of a constitutive mineral and of voids. At the large scale, we account for the volume fraction of each mineral, the porosity, and the pore structure of the void space. The elastic deformation of a large-scale model is simulated using a finite element method (FEM), whose results are tested against independent lab measurements. The proposed two-scale model has applications for geomechanical characterization of a formation at the core scale from drill cuttings.

Keywords Two-scale model · Representative element · Pore structure · Finite element method (FEM) · Drill cutting

List of Symbols

A_m	Cross-sectional area of the grain with a known mineralogy
A_M	Cross-sectional area of the core-scale model
A_r	Cross-sectional area of the representative element
E_m	Elastic modulus of the mineral
E_M	Elastic modulus of the core-scale model
E^{Ave}_{Model}	Average of the predicted elastic moduli
E^{Max}_{Lab}	Maximum of the measured elastic moduli
E^{Min}_{Lab}	Minimum of the measured elastic moduli
E_r	Elastic modulus of the representative element
Error	Error of the predicted Young's moduli at the core scale
f_i	Volume fraction of each mineral
G_m	Shear modulus
I_m	Moment of inertia
J_m	Polar moment of inertia
k_r	Stretching stiffness
k_θ	Bending stiffness
k_ϕ	Torsional stiffness
L_m	Average size of a solid grain with a known mineralogy
L_M	Length of the core-scale model
L_r	Length of the representative model
M	Bending load
N	Axial load
N_i	Number of the representative elements relevant to the *i*th mineral in the core-scale model
N_t	Total number of the representative elements in the core-scale model
P	Compressive load
T	Torsion of a solid medium
U_A	Stretching or compression potential energy
U_M	Bending potential energy
U_r	Stretching energy of a solid medium
U_T	Torsional energy
U_{total}	Total potential energy of the solid medium
U_θ	Angle bending energy of the solid medium
U_ϕ	Torsional energy of the solid medium
α	Rotational angle of the solid medium ends
ε	Normal strain of the model
ΔL_m	Change in the length of the solid medium
Δr	Stretching elastic deformation
$\Delta\beta$	Torsion angle of the solid medium
$\Delta\theta$	Angle bending elastic deformation
$\Delta\phi$	Torsional elastic deformation
σ	Normal stress of the model
ϕ_1	Microporosity

✉ A. Sakhaee-Pour
asakhaee@central.uh.edu

[1] Department of Petroleum Engineering, University of Houston, Houston, TX 77204, USA

Published online: 12 August 2018